WASHINGTON UNIVERSITY IN ST. LOUIS

School of Engineering & Applied Science

Department of Mechanical Engineering and Materials Science

Dissertation Examination Committee:
Philip Bayly, Chair
Susan Dutcher
Ruth Okamoto
David Peters
Jin-Yu Shao
Jessica Wagenseil

Probing Mechanical Forces in Flagella by Manipulation of Media Viscosity and Axonemal Structure

by
Kate Wilson

A dissertation presented to the
Graduate School of Arts & Sciences
of Washington University in
partial fulfillment of the
requirements for the degree
of Doctor of Philosophy

May 2015
St. Louis, Missouri

Table of Contents

List of Figures ... v

List of Tables ... vii

Acknowledgments ... viii

Abstract ... x

Chapter 1 ... 1

Introduction: An Overview of Flagella Structure and Function ... 1

- 1.1 Cilia and Flagella are Important Biological Motors ... 1
  - 1.1.1 Normal Function ... 1
  - 1.1.2 Dysfunction ... 2
- 1.2 *Chlamydomonas reinhardtii* as a Model Organism ... 4
- 1.3 Details of Shape and Structure ... 6
  - 1.3.1 Structure of the Flagellar Axoneme ... 7
  - 1.3.2 Active Elements of the Flagellar Axoneme ... 9
- 1.4 Function: How do Flagella Generate Motion? ... 10
- 1.5 Mathematical Modeling of Flagellar Beating ... 11
- 1.6 Dissertation Organization ... 13

Chapter 2 ... 16

Experimental Methods for Characterization of the Flagellar Waveform ... 16

- 2.1 Introduction and Motivation ... 16
- 2.2 Cell Culture and Genetics ... 16
- 2.3 Optical Microscopy Recordings ... 18
- 2.4 Viscosity ... 18
- 2.5 Image Processing ... 18
- 2.6 Waveform Analysis ... 21
- 2.6 Post-Processing ... 25

Chapter 3 ... 28

The Effects of Viscosity on Flagellar Waveform in Normal and Mutant Flagella ... 28

- 3.1 Introduction and Motivation ... 28
- 3.2 Cell Body Parameters ... 29

3.3 Waveform Parameters 35
3.4 Discussion 45
Chapter 4 49
Methods for Mathematical Modeling of Flagella Motion 49
4.1 Introduction and Motivation 49
4.2 Background 49
4.3 General Equations of Flagella Motion 50
4.2.1 Kinematics 51
4.2.2 Equilibrium Conditions 52
4.2.3 Constitutive Relations 53
4.2.4 Derivation Steps 54
4.3 Discussion 56
Chapter 5 58
Unstable Modes in a Model of Sliding-Controlled Dynein Activity 58
5.1 Introduction and Motivation 58
5.2 Linearized Equation of Motion and Shear Force 59
5.3 Eigenvalue Problem 61
5.4 Solution to the Eigenvalue Problem 65
5.5 Results and Stability 67
5.5.1 Case 1: Finite Sliding Compliance at the Base 67
5.5.2 Case 2: No sliding at the base 73
5.6 Discussion 77
Chapter 6 79
Mathematical Formulation of the Geometric Clutch Hypothesis 79
6.1 Introduction and Motivation 79
6.2 Model: Two Doublet Pairs 80
6.3 Doublet Pair Interactions 82
6.3.1 Equilibrium Equations 82
6.3.2 Inter-Doublet Separation and Transverse Force 83
6.3.3 Cross-Bridge Attachment and Dynein Activity 86
6.4 Opposing Doublet Pairs 89
6.4.1 Inter-Doublet Equations: Two Doublet Model 91

6.4.2 Load Dynamics of Inter-Doublet Separation 92
6.5 Stability Analysis 96
6.5.2 Eigenvalue Problem for the GC Model 97
6.5.3 Numerical Eigenanalysis and Simulation 99
6.5.4 Unstable Modes of the GC Model 100
6.6 Large Amplitude, Nonlinear Flagella Oscillations 102
6.7 Discussion 104
Chapter 7 107
Discussion and Future Work 107
7.1 Summary 107
7.1.1 Key Findings and Results 108
7.1.2 Significance 109
7.2 Limitations 110
7.2.1 Cell Experiments 110
7.2.2 Modeling Assumptions 111
7.3 Future Work 112
7.3.1 Non-Periodic Oscillations 112
7.3.2 Model Validation 112
7.3.3 Clinical Diagnostics 112
7.3.4 Microfluidics 113
7.3.4 Outlook 113
References 114
Vita 125

List of Figures

Figure 1.1 – Cilia and flagella in the body ... 2
Figure 1.2– Ciliary components and associated disease ... 3
Figure 1.3 – Ciliary ultrastructure ... 4
Figure 1.4 – Diagram of flagellum origin and cross-section ... 7
Figure 1.5 – Axonemal Elements from Cryo-EM ... 9
Figure 1.6 – Diagram of sliding filaments ... 12
Figure 1.7 – Diagram of transverse force and curvature ... 12
Figure 2.1 – Cell body registration ... 19
Figure 2.2 – Fourier analysis of uniflagellate cell rotation ... 20
Figure 2.3 – Waveform tracing steps. ... 22
Figure 2.4 – Demonstration of Isomap sorting ... 23
Figure 2.5 – Polynomial fit figures ... 24
Figure 2.6 – General beat characteristics ... 25
Figure 2.7 – Typical normalized curvature map ... 26
Figure 3.1 – Beat frequency vs viscosity ... 30
Figure 3.2 – Cell body rotations per second ... 31
Figure 3.3 – Beats per revolution ... 32
Figure 3.4 – Force balance between cell body and flagellum ... 32
Figure 3.5 – Work generated by the flagellum vs viscosity ... 34
Figure 3.6 – Propulsive force and power vs viscosity ... 35
Figure 3.7 – Characteristic waveforms for selected experimental conditions. ... 37
Figure 3.8 – Normalized flagellar stroke width ... 38
Figure 3.9 – Maximum and minimum normalized curvature values $\bar{\kappa}$ ... 40
Figure 3.10 – Average normalized absolute curvature ... 41
Figure 3.11 – Normalized bend propagation speeds ... 42
Figure 3.12 – Normalized delay times ... 43
Figure 3.13 – Power and recovery stroke completion with viscosity ... 44
Figure 4.1 – Flagellum schematics ... 50
Figure 4.2 – Free body diagram of a differential element of a beam in viscous fluid ... 52
Figure 5.1 – Schematic of sliding displacement ... 60
Figure 5.2 – Eigenvalues from direct solution of the sliding-controlled flagella model ... 69
Figure 5.3 – Unstable and neutrally-stable modes of the sliding-controlled model with sliding at the base (Case 1). ... 70
Figure 5.4 – Frequency of least stable mode and bend propagation direction, sliding-controlled model (Case 1) ... 71
Figure 5.5 – Nonlinear simulation of sliding-controlled model with sliding at base (Case 1) ... 72
Figure 5.6 – Comparison of frequency of periodic solutions from direct analysis and weighted residual predictions, no base sliding (Case 2). ... 74

Figure 5.7 – Eigenvalues of the sliding-controlled model with no base sliding (Case 2) from the weighted residuals method 75
Figure 5.8 – Mode shapes of the sliding-controlled model with no sliding at base (Case 2). 75
Figure 5.9 – Nonlinear simulation of sliding-controlled model with no sliding at base (Case 2) 76
Figure 6.1 – Schematic of two doublet-pair model........ 81
Figure 6.2 – Free body diagram of a single doublet pair 82
Figure 6.3 – Schematic diagrams of inter-doublet separation. 84
Figure 6.4 – Effect of inter-doublet separation on the rate of cross-bridge attachment or detachment 87
Figure 6.5 – Dynamics of inter-doublet separation variables A and h. 93
Figure 6.6 – Analogous equations for A and h 95
Figure 6.7 – Propagation of inter-doublet separation 96
Figure 6.8 – Eigenvalues of the GC model from the weighted residual method........ 101
Figure 6.9 – Unstable modes of the GC model........ 101
Figure 6.10 – GC waveforms of *Chlamydomonas* flagella from time-marching simulation 103
Figure 6.11 – Nonlinear simulation of geometric clutch model 104

List of Tables

Table 2.1 – Mutants Examined 17
Table 5.1 – Parameter values for sliding-controlled model with base sliding 68
Table 5.2 – Parameter values for sliding-controlled model with no base sliding 73
Table 5.3 – Comparison of SC fundamental modes from simulation and direct eigenanalysis ... 77
Table 6.4 – Summary of equations of flagella motion and inter-doublet separation........ 89
Table 6.5 – Equations for principal (P) and reverse (R) doublet pairs 91
Table 6.6 – Parameter values of the continuum GC model 93
Table 6.7 – Comparison of GC fundamental modes from simulation to the linearized system . 104

Acknowledgments

I would like to sincerely thank and acknowledge my adviser, Dr. Philip Bayly, for his amazing patience and support throughout my research career. I have benefitted immensely from his guidance and dedication to not only producing great research, but great researchers. I also acknowledge the guidance and support of Dr. Ruth Okamoto, a fantastic educator and mentor who has cultivated great work from every member of the lab and whose outreach has surely inspired the next generation of great engineers and scientists. Finally, I acknowledge Dr. Susan Dutcher, who has managed to teach the mechanical engineers biology. Her scientific curiosity and deep understanding of *Chlamydomonas* has inspired new perspectives leading to many discoveries about these little algae with big impact.

To my colleagues, friends, and family: I sincerely thank you for supporting me, while encouraging other adventurous endeavors. I have learned much about balance and perspective from your lives and truly appreciate your friendship.

I gratefully acknowledge the support of NIH training grant T32 14855-2 to Dr. Joseph Culver through the Imaging Sciences Pathway Fellowship. Through this grant I gained valuable skills and knowledge in imaging modalities, in addition to networking and informative sessions at the 2014 NIBIB Training Grantees Meeting. Participation in this pathway has made me a more informed and well-rounded scientist. I also acknowledge NSF grant CMMI 1265447 to Dr. Philip Bayly for continued support on understanding how axonemes work.

Kate Wilson

Washington University in St. Louis

May 2015

Dedicated to my family.

ABSTRACT OF THE DISSERTATION

Probing Mechanical Forces in Flagella by Manipulation of Media Viscosity and Axonemal Structure

by

Kate Wilson

Doctor of Philosophy in Mechanical Engineering

Washington University in St. Louis, 2015

Professor Philip Bayly, Chair

Cilia and flagella are subcellular organelles used to generate fluid flow or propel the cell. These long cylindrical structures are composed of cytoskeletal elements activated by the unidirectional motor protein dynein. Cilia and flagella are crucial to a number of physiological functions, yet the specific mechanisms of dynein activation and coordination remain unclear. This work investigates the response of the flagellum of *Chlamydomonas reinhardtii* to increased mechanical loading achieved by variation of media viscosity, and to structural changes achieved by genetic manipulation. Effects of these perturbations are quantified using high spatiotemporal resolution recordings; the results demonstrate mutation-specific changes to the flagellar waveform. The flagellum may be mathematically modeled as a slender beam in viscous fluid. Two proposed mechanisms of dynein regulation are evaluated by identification of unstable modes and by numerical simulation. The sliding-controlled model of dynein regulation leads to non-propulsive retrograde modes of bend propagation. The geometric clutch model provides a mechanism of anterograde bend propagation and flagellar feedback which promotes bend switching at the base, similar to observed waveforms.

Chapter 1

Introduction: An Overview of Flagella Structure and Function

This thesis is concerned with the mechanisms that produce oscillations and waves in flagella. In this chapter, I introduce the basic structure and function of these subcellular organelles, and explain the motivation for the studies described in subsequent chapters.

1.1 Cilia and Flagella are Important Biological Motors

1.1.1 Normal Function

Cilia and flagella are thin, whip-like organelles used to propel cells or generate fluid flow. The names cilia and flagella refer to the same cytoskeletal structure – the axoneme – based on location and density of structures. Large groups, such as those found on the surface of airway epithelial cells, are termed cilia, while the individual motile structure (such as that propelling a sperm) is called a flagellum. In this work, the terms flagellum and cilium are used generally. Eukaryotic cilia are long cylindrical structures roughly 200 nm in diameter and up to10 μm long in human airway epithelia cells, although they can be up to 2mm long depending on species and function [1]. Flagella act as biological motors by actively generating bends along the length of the axoneme,. Bends are generated by the relative sliding of microtubules within the axoneme paired with elastic properties of the structure[2], [3]. Significantly, flagella are self-organized beating structures [4] that do not require innervation in order to function.

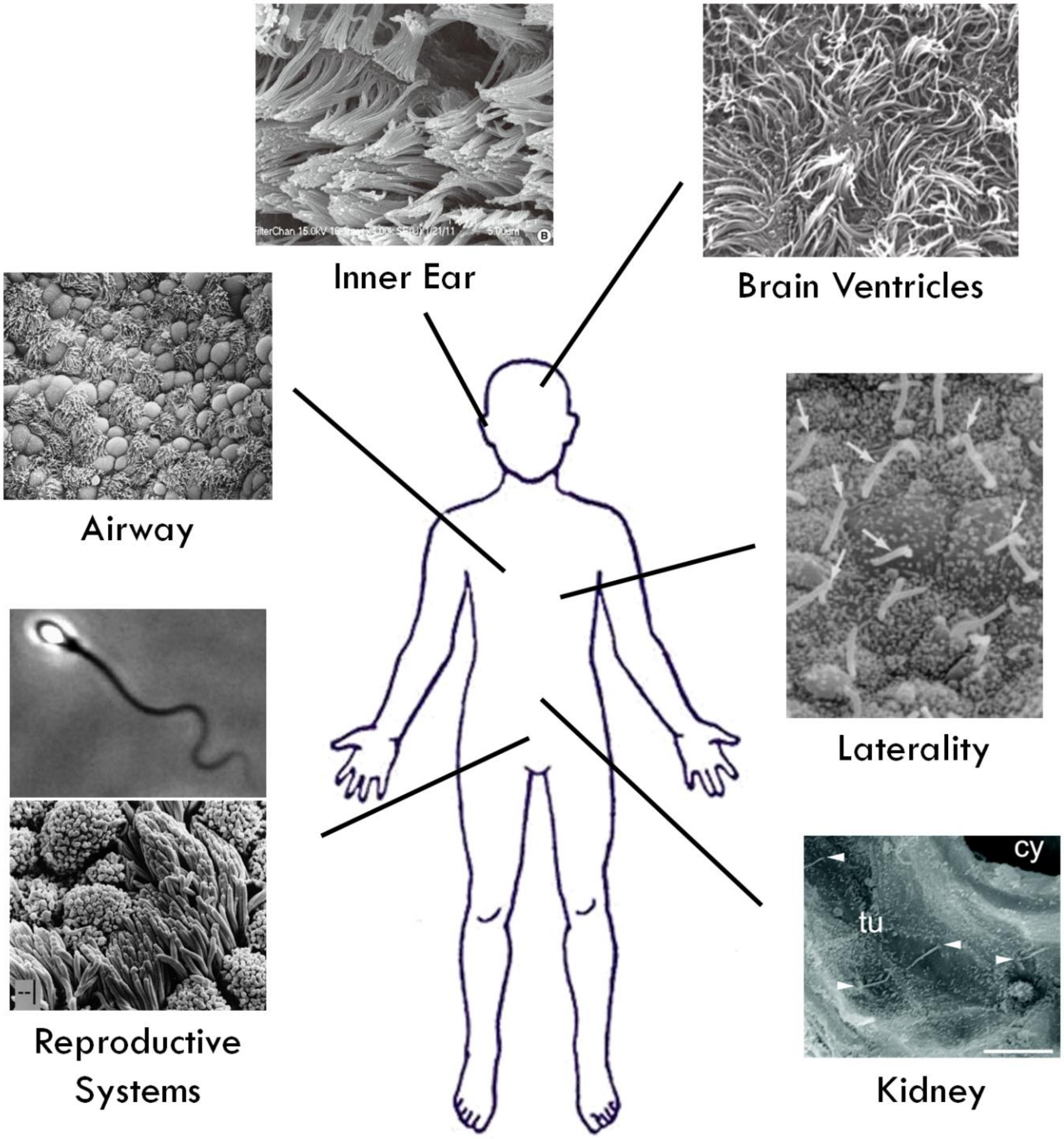

Figure 1.1 – Cilia and flagella in the body
Proper function of cilia and flagella is crucial to a number of body systems. Active structures are found in the airway epithelia, brain ventricles, embryonic node, and both male and female reproductive systems. Ciliary dysfunction and PCD is associated with laterality defects, inner ear infections, polycistic kidney disease, and congenital heart defects, among others. Images ('Inner Ear' clockwise) from references [5]–[11].

1.1.2 Dysfunction

Ciliary defects have pervasive effects on human health. Inherited ciliary disorders are generally termed Primary Ciliary Dyskinesia (PCD) and include Kartagener syndrome, Bardet-Beidel syndrome, and are often associated with Polycystic Kidney Disease (PKD) and Congenital Heart Disease (CHD) [12]–[18]. PCD is a genetically and phenotypically heterogeneous disorder with many potential effects, a few of which are shown with the associated ciliary defect in Figure 1.2 [13], [15], [16], [19]. Most commonly, PCD cases are associated with mutations in genes that cause outer dynein arm defects [18], [20]–[22].

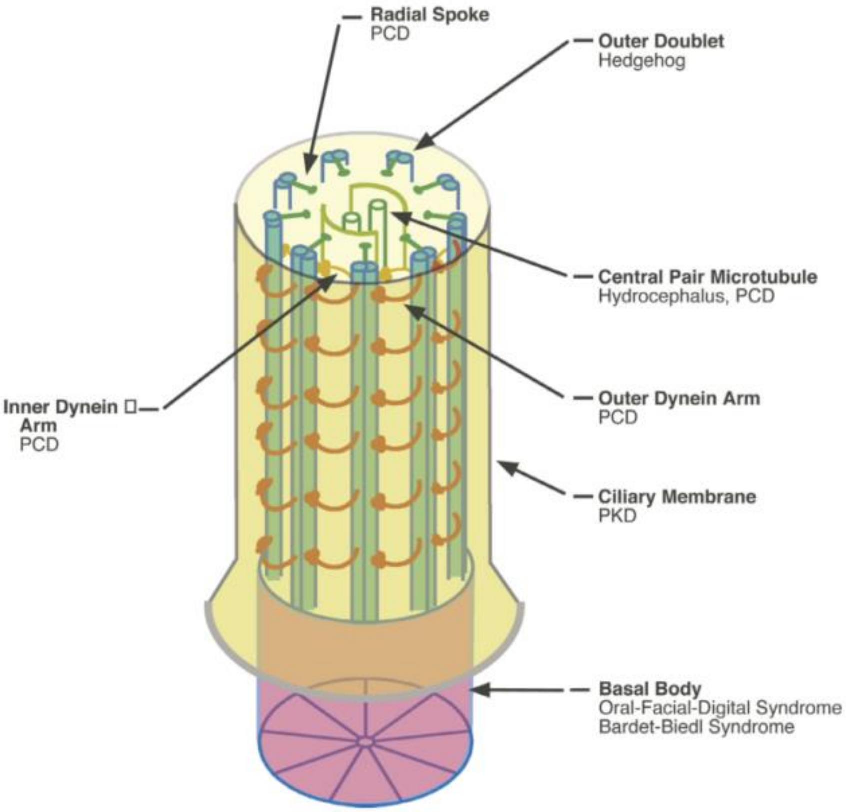

Figure 1.2– Ciliary components and associated disease
Schematic of flagellum showing basal body, transition zone, and axoneme with associated known disease states. Figure from [16].

Typically PCD is diagnosed through transmission electron microscopy (TEM) of airway epithelial cilia; however a quantitative, automatic functional assessment would contribute a valuable tool to diagnosis of this heterogeneous disease. The differences observed here between inner- and outer – dynein arm deficient mutants suggests a functional assessment could someday distinguish between these disease states. While some currently identified genes (including DNAI1 and DNAH5 [16], [18], [23]–[26]) have been shown to create outer-arm defects, the heterogeneity in the disease suggests there may be many genetic and structural defects that lead to the clinical diagnosis of PCD. In particular, outer arm defects appear to be more correlated with laterality defects than inner arm or central apparatus defects [23]. The development of such a diagnostic technique is outside the scope of this thesis. However, quantitative functional analysis methods may ultimately find value as diagnostic tools.

1.2 *Chlamydomonas reinhardtii* as a Model Organism

The single celled green alga *Chlamydomonas reinhardtii* is an excellent model organism for studying flagellar function due to a high degree of structural correlation, functional similarities in motion, and ease of lab culture and study [27].

1.2.1 Structural Similarities to Human Cilia

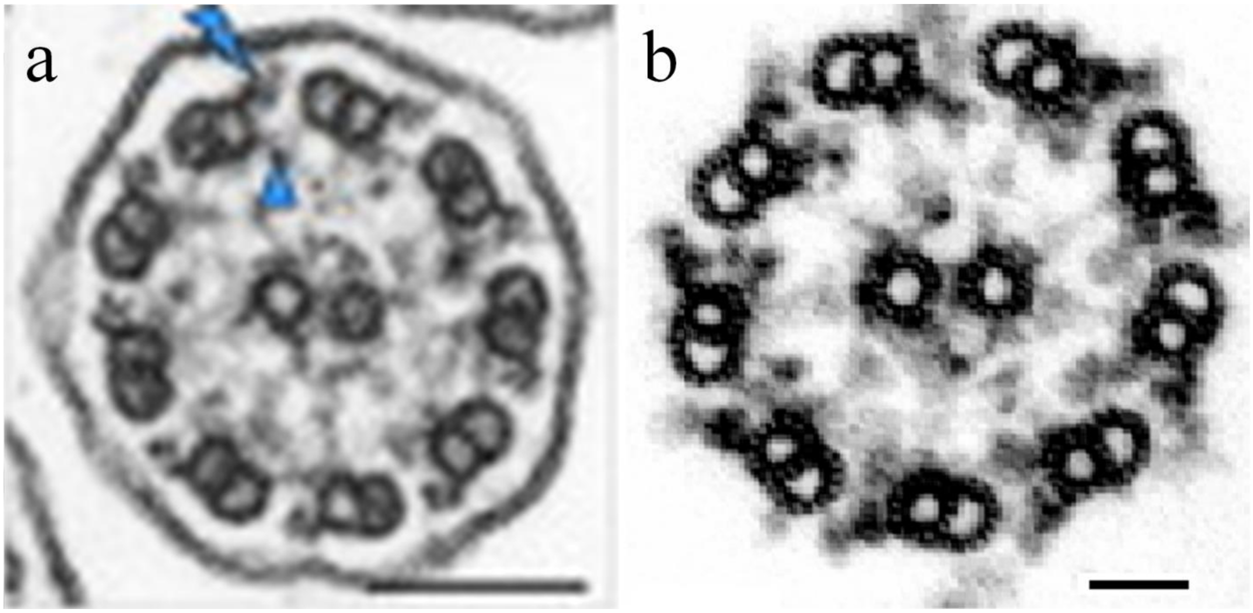

Figure 1.3 – Ciliary ultrastructure
(a) Cross sectional TEM of an airway cilium [28], arrows show dynein arms, scale bar 100 nm
(b) Cross sectional EM of Chlamydomonas flagellum [29], scale bar 50 nm

Human cilia and *Chlamydomonas* flagella share a high degree of structural similarity, as shown in Figure 1.3, thus study of this simple organism is directly relevant to the investigation of human disease [13], [27], [30]–[33]. Both the structure and the corresponding proteins in microtubules, dynein arms, radial spokes, and central pair projections are conserved among eukaryotes and *Chlamydomonas* [18], [22], [25], [34]. Human cilia display diversity in structure and function; the typical 9+2 motile structure is found in airway cilia and sperm flagella, however there are also instances of 9+0 axonemes lacking a central pair, which may be motile (in the case of nodal cilia) or immotile (in the case of most primary sensory cilia) [12], [22], [35]. Here I consider only 9+2 motile axonemes. *Chlamydomonas* mutants lacking the radial spokes or central pair are often immotile or display an irregular beat [36]. The similarity in structure and sequence makes *Chlamydomonas* an excellent model for investigation of the flagellar axoneme.

1.2.2 Cellular Characteristics

Chlamydomonas reinhardtii is a single-celled organism roughly 10 μm in length by 5μm in diameter. The cell grows two ~ 8-12 μm flagella that beat in a coordinated breaststroke fashion to propel the cell through media. Cells manipulate beating modes from an asymmetric, propulsive beat pattern to a symmetric, ‘backwards only’ waveform [37]. It is thought that cells switch between these beating modes and regulate individual flagellum activity in order to manipulate swimming direction and access sunlight and nutrients [38]. Symmetric beating patterns may also be induced in isolated axonemes at high calcium concentrations [36], [39]). The beat of the *Chlamydomonas* flagellum is approximately planar [36], [40], allowing visualization of the entire flagellum within the focal plane of a regular optical microscope.

1.2.3 Laboratory Methods

Chlamydomonas may be readily cultured in the lab under illumination in liquid or solid growth media [41]. Large numbers of cells can be quickly grown and isolated for proteomic analysis. In the lab, it is straightforward to cross mutant strains and characterize resulting progeny [19], [42]. As a result of many years of study, the *Chlamydomonas* genome has been sequenced [43]. Investigation of the flagellar proteome has identified over 600 polypeptides in the axoneme [44]–[46], proving the utility of flagellar isolation and comparative genomics techniques. Flagella are not essential for the cell cycle, thus mutations that cause flagellar dysfunction can still be investigated using standard genetics techniques. In addition, the scale of the cell and flagellum means that whole cells can be analyzed under a brightfield optical microscope with respect to flagellar motion, eliminating changes to flagellar behavior associated with demembranation and flagellar isolation.

1.3 Details of Shape and Structure

As noted above, the flagellum is a complex microtubule-based structure that generates active bending via the ATP-driven motor protein dynein [47]. The axoneme consists of structural elements (microtubules, radial spokes) as well as active elements (dyneins) that hydrolyze the cellular energy storage molecule adenosine triphosphate (ATP) to generate motion.

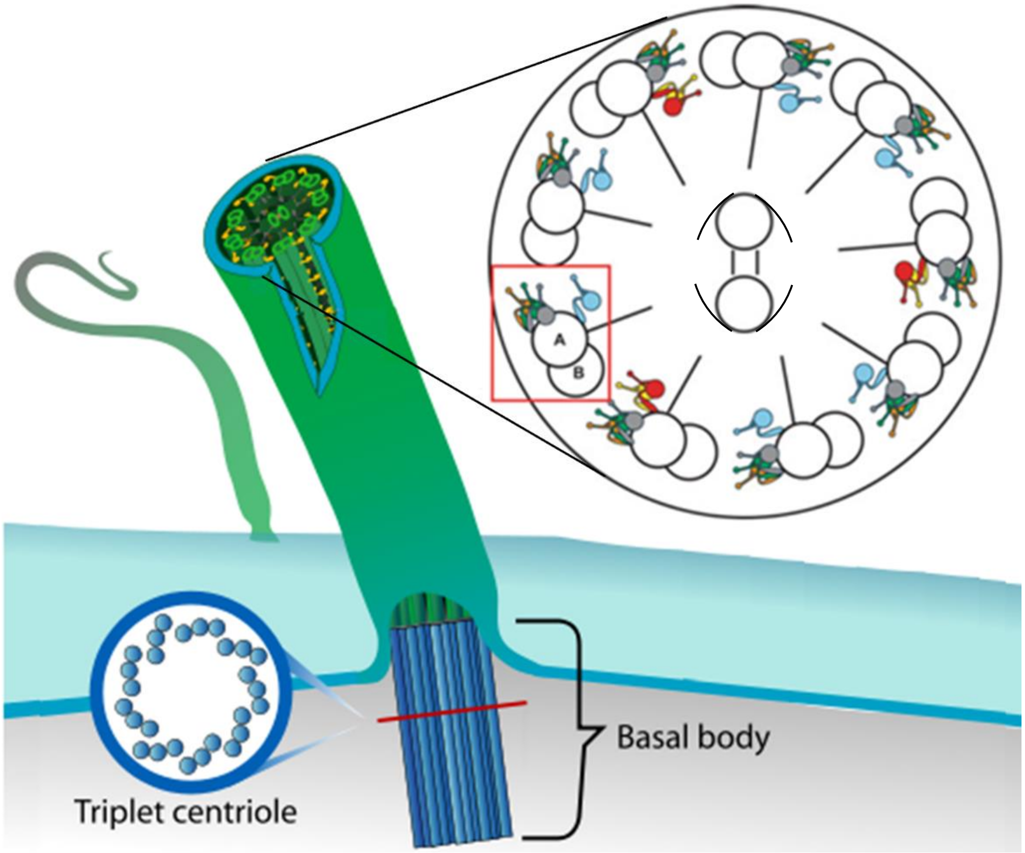

Figure 1.4 – Diagram of flagellum origin and cross-section
The flagellum protrudes from the cell membrane from an anchored centriole, termed the basal body. A cross section of the flagellum structure is shown at right, viewed from the proximal end of the flagellum. The A and B tubule of one outer doublet is labeled, along with dynein arms (gray, green, red, blue), radial spokes, and central pair with projections (adapted from [48], [49]).

1.3.1 Structure of the Flagellar Axoneme

Microtubules are polar structures that form the foundation of the flagellar axoneme (polarity here refers to organization of subunits and not to electrical charge). Roughly 25 nm in diameter, microtubules grow from a 'minus' end to a 'plus' end through association of heterodimeric tubulin subunits. As shown in Figure 1.4, the flagellum originates in a basal body composed of triplet microtubules then passes through a complex transition zone where one partial tubule terminates [50], [51]. The remaining microtubule doublets protrude away from the cell as the key structural components of the axoneme. Each microtubule doublet has a complete 'A' microtubule connected to a partial 'B' microtubule, as shown in Figure 1.4 and Figure 1.5 [52].

In the axoneme there are nine outer doublets arranged around a central pair of singlet microtubules (Figure 1.4). Protruding from each A tubule are dynein arms, labeled for their proximity to the central pair (inner dynein arms, IDAs, are closest to the central pair while outer dynein arms, ODAs, are furthest from the central pair). In addition to these motor proteins, the axoneme contains the flexible linker protein nexin that connects the A tubule to the adjacent B tubule and limits inter-doublet sliding [53], [54]. Radial spokes (RS) protrude from each A tubule towards the central pair and may interact with central pair projection proteins to regulate dynein activity [55]–[59]. The dynein regulatory complex (DRC) is located at the base of a radial spoke and is thought to associate with the outer-inner dynein linker (OID) to regulate dynein activity [52]. There is evidence that the DRC and nexin link are within the same structure, termed instead the N-DRC [60].

Dynein arms, radial spokes, and other regulatory proteins are patterned along the length of the flagellum in a series of periodically repeating 96 nm sections, with the exception of a few low-abundance proteins [61], [62]. A typical 96nm section is shown in Figure 1.5 [52]. Outer dynein arms are anchored to the A tubule every 24 nm, while 7 separate IDA heavy chains are found within the 96 nm repeat as shown.

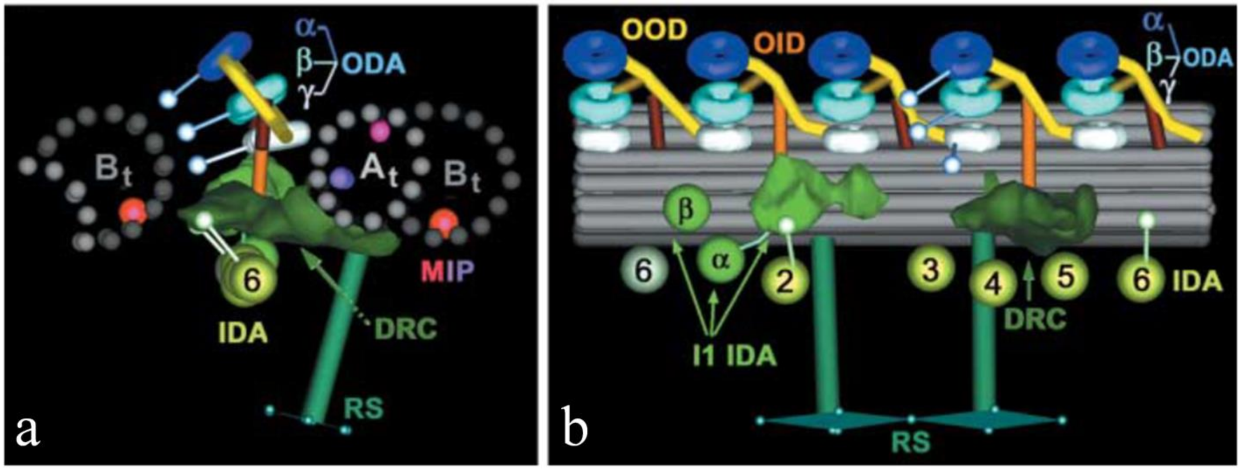

Figure 1.5 – Axonemal Elements from Cryo-EM
(a) Diagram of adjacent microtubule doublets (looking distal-to-proximal) showing locations of outer dynein arms (ODA), inner dynein arms (IDA), dynein regulatory complex (DRC), radial spokes (RS), and microtubule inner proteins (MIP); (b) Characteristic longitudinal repeat of structures along the doublet (proximal - end to the left, distal + end to the right) including ODAs, IDAs (labeled I1α, β, 2-6), RS, and DRC as well as the outer-outer dynein linker (OOD) and outer-inner dynein linker (OID). Figure from [52].

1.3.2 Active Elements of the Flagellar Axoneme

Dynein is a uni-directional molecular motor that moves towards the minus end of a microtubule (a structural protein composed of polar tubulin subunits) through ATPase activity of a ring of 6 AAA+ domains [48]. Dyneins are differentiated from the other molecular motor proteins kinesin and myosin by their large heavy chain (HC) domain, which is over 500 kDa [48]. Specific dynein molecules vary in the number and composition of heavy chains as well as the size and types of smaller associated subunits. In the *Chlamydomonas* axoneme, outer dynein arms are trimeric with 3 heavy chains (α, β, γ) attached permanently to the A tubule by the tail domain. Outer dynein arms also contain a tail subcomplex of 2 intermediate chains and 8 light chains [48]. In contrast the inner dynein arms are simpler monomeric motors with only one HC, with the exception of IDA I1/f which contains two HC domains[48]. During the power stroke, the dynein stalk attaches to a neighboring microtubule via the microtubule binding domain (MTBD) and slides the microtubule by conformational changes induced by ATPase activity in the motor domain. Studies have shown the dynein power stroke to act over a distance of ~15nm [63].

1.4 Function: How do Flagella Generate Motion?

Flagella are ‘self-organized’ oscillators – requiring no external input or pacing source, although calcium and mutations can change beat characteristics [36], [39], [64]. Within the axoneme, dynein motors must overcome elastic structural resistance (from at least microtubules, radial spokes, and N-DRC) in order to generate bends [55], [65]. While single molecule studies and electron microscopy have provided a basis for understanding the mechanism of the dynein power stroke [33], [63], [66], [67], the spatiotemporal control of activation along the axoneme remains unknown. Each dynein heavy chain is able to generate a different amount of sliding force and is characterized by a specific force-velocity curve [42], [48], [68], [69]. Even at the level of the I1/f dyneins, the α and β heavy chains are thought to play different roles in the generation of force between adjacent microtubule doublets [70]. Despite the complexity of this structure, the flagellum is able to generate productive bends that not only move the axoneme, but provide a driving force to the attached cell or surrounding fluid.

This work examines the importance of mechanical feedback in regulating flagellar dynein coordination. The periodicity and consistency of dynein motors makes it unlikely that individual heavy chains are responsible for bends at a given length along the flagellum. Likewise, the presence of diverse polypeptides within the axoneme (including motor protein kinesins used for intraflagellar transport) makes it unlikely that dynein activation is controlled exclusively by a propagating wave of ATP. Testing this hypothesis requires varying the mechanical loading of the flagellum, which is achieved by manipulating media viscosity.

The goal of this thesis is to better understand how mechanically feedback affects the function of the axoneme. By quantifying waveforms of genetic mutants under different viscosity conditions, we hope to gain insight regarding the functions of specific dyneins as well as the action of the flagellum as a whole.

1.5 Mathematical Modeling of Flagellar Beating

Mathematical models of the flagellum have been developed in an effort to understand the underlying principles governing flagellar motion. Even prior to the discovery of dynein, mathematical modeling provided evidence for the existence of a distributed force-generating mechanism along the length of the flagellum [71]. The spatiotemporal control of this force-generation mechanism (now known to be dynein) remains a subject of debate. A model of inter-doublet sliding dependent force generation (see Figure 1.6) was first proposed by Brokaw and has since been refined [2], [72]–[77]. A fundamental continuum model of the flagellum as a beam was developed in 1978 by Hines and Blum, with a proposed curvature-controlled force term [78]. This basic continuum model of the flagellum is described more fully later in this thesis (Chapter 4). Finally, a series of papers by Lindemann propose that transverse force between doublets (Figure 1.7) is the key regulator of dynein activity propagation along the axoneme [79]–[83]. Lindemann's ideas are explored further in Chapter 6 of this thesis.

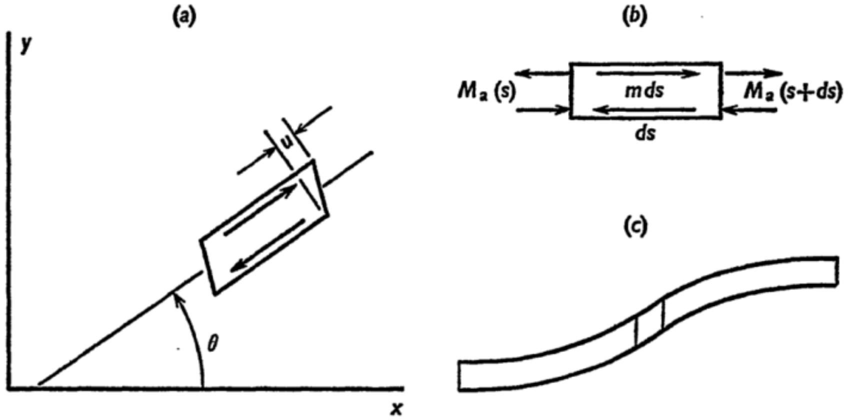

Figure 1.6 – Diagram of sliding filaments
Fundamental description of the axoneme as a beam subject to bending via active sliding elements, proposed by Brokaw (Figure from [2]).

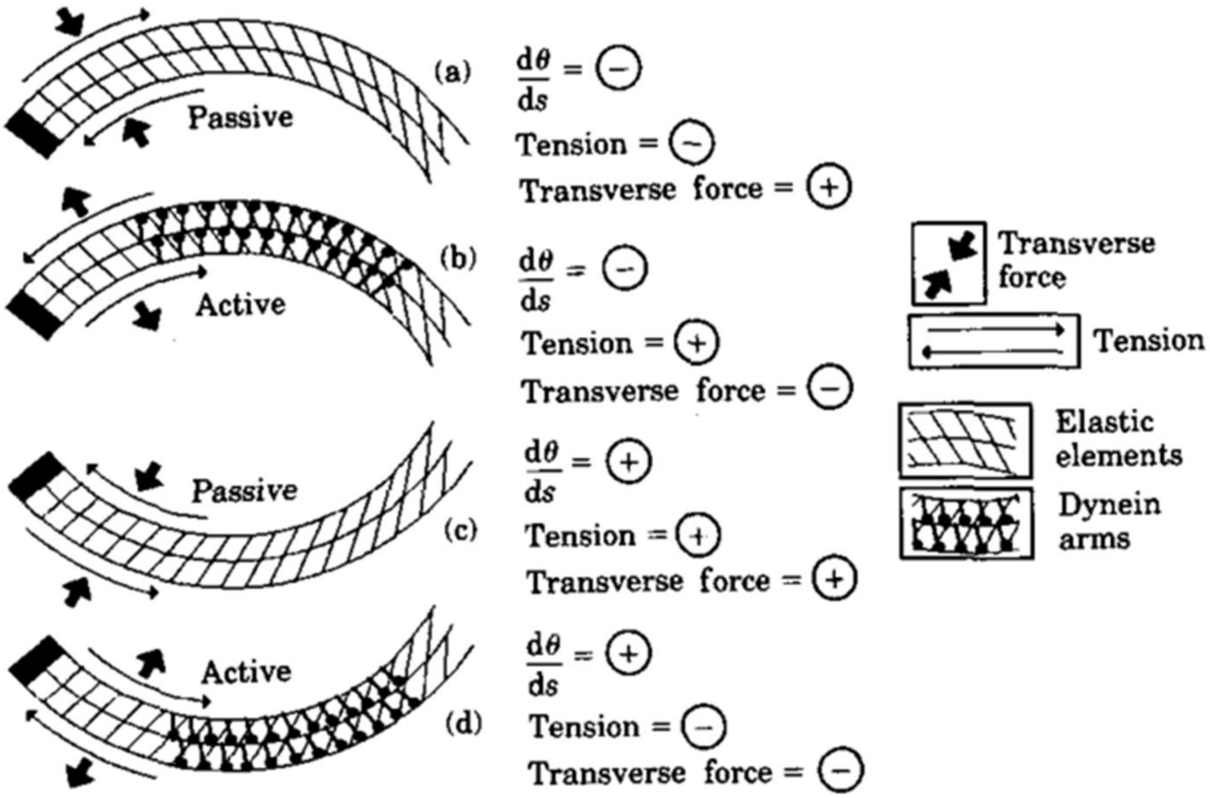

Figure 1.7 – Diagram of transverse force and curvature
Geometric clutch model proposed by Lindemann: Passive and active elements depicted at negative (a-b) and positive (c-d) curvatures, along with tension within the axoneme and transverse force. Figure from [79]. This model is described in more detail in Chapter 6.

The fundamental utility of a model is to inform our understanding of an observed process, not necessarily to exactly replicate the behavior. Essentially, a model is a precise, quantitative hypothesis that can be tested by comparison to observations and experiments. Here, we allow many simplifications including describing active force by a single continuous function of space and time (instead of individual dynein heads), the use of resistive force theory to describe fluid-flagellum interactions, and simplification of the axoneme geometry.

We examine the premise of periodic response developed by Riedel-Kruse [75] and extend the closed-form solution for a sliding filament model to a more general approach, discovering non-periodic modes at the same parameter values [84]. In addition, we formulate the geometric clutch as a continuum model which can only be resolved through time-marching simulation. For each model, we examine the stability of the identified solutions and comment on the feasibility of the obtained solution as a mechanism for flagellar control.

1.6 Dissertation Organization

1.6.1 Specific Aims

This dissertation describes progress toward three specific aims, all tied toward the over-arching objective of understanding the generation of autonomous, propulsive oscillations of flagella and cilia.

- Specific Aim 1: Investigate the mechanics of flagella in wild-type *Chlamydomonas* by characterizing the effects of viscosity on waveform,
- Specific Aim 2: Investigate the mechanics of flagella in mutant *Chlamydomonas* lacking specific axonemal components by characterizing the effects of viscosity on waveform in these mutants.

- Specific Aim 3: Evaluate and improve upon existing computational models of the flagellar waveform.

The overall goal of this work is to use tools and concepts from mechanical engineering to understand how the flagellum develops a propulsive, coordinated waveform. Key mechanical engineering concepts include nonlinear, slender elastic beam theory, low-Reynolds number fluid mechanics, stability analysis, and computational modeling schemes. Manipulation of loading force is achieved through increasing media viscosity.

This study provides experimental evidence and theoretical arguments to answer the question, “How does mechanical force contribute to control of the flagellar waveform?”

1.6.2 Chapter Organization

The remainder of the dissertation is organized as follows:

Chapter 2 introduces the methods used to acquire and analyze experimental data.

Chapter 3 describes the effects of changes in viscosity and various genetic mutations on the *Chlamydomonas* flagellum waveform.

Chapter 4 reviews the derivation of the equations of a slender beam in viscous fluid; these equations underlie the mathematical modeling of flagellar motion.

Chapter 5 examines a previously-published model of a sliding-controlled mechanism of flagellar bending. Unstable modes are found at the same parameters used in the prior study to identify periodic modes; this new evidence weakens the case for the particular model.

Chapter 6 examines the “geometric clutch” mechanism of flagellar bending and formulates a continuum model of the flagellum with inter-doublet shear force regulated by transverse separation between the doublets.

Chapter 7 presents a summary of the project, as well as conclusions, discussion of limitations, and speculation into future work.

Chapter 2

Experimental Methods for Characterization of the Flagellar Waveform

Quantification of waveform parameters requires cell preparation, microscopy, video recording, image processing, and data analysis. This chapter presents a description of the steps taken to obtain and evaluate data to quantitatively describe the flagellar beat.

2.1 Introduction and Motivation

Chlamydomonas flagella are typically around 200 nm in diameter and range from ~8-12 µm. Optical microscopy is possible at this scale, but the diameter of the flagellum is close to the theoretical limit of optical resolution, $r = \lambda/2NA$ with a numerical aperture of 1.0 and standard white light with wavelengths ranging ~ 400-700 nm. We used methods to maximize resolution at recording through the use of DIC optics, as well as post-processing techniques to increase contrast. We have developed and refined automated analysis algorithms to concisely characterize flagellar waveforms and summarize spatiotemporal patterns for mechanical analysis[85], [86]. This chapter outlines the tools and techniques developed in order to quantify *Chlamydomonas* flagellum waveforms.

2.2 Cell Culture and Genetics

The wild-type strain of the single-celled alga *Chlamydomonas reinhardtii* swims propulsively through media with two flagella in order to access sunlight and photosynthesize. In 1982, mutant cells growing only a single flagellum were isolated and characterized by their distinct spinning phenotype [87]. Uniflagellate cells provide a distinct advantage in waveform analysis – without net forward motion cells spin in place and may be recorded over longer periods of time within a specific field of view. This allows focused, high resolution optical microscopy at high speeds (350 frames per second) and tuning of microscope settings to each particular cell.

To evaluate the effects of specific dynein arm proteins, each mutant was crossed into the *uni1* background with desired progeny selected by phenotype [88], performed by the Dutcher lab. Uniflagellate cells and biflagellate mutant cells were obtained from the *Chlamydomonas* Resource Center (St. Paul, MN). Each dynein arm mutant (described in Table 2.1) was crossed with uniflagellate cells to generate *Chlamydomonas* cells with the desired dynein arm mutation within only one flagellum. Note, double-mutants are described only with respect to structural defect (hence, *ida1*;*uni1* cells are referred to as *ida1*, etc).

Table 2.1 – Mutants Examined

Gene	**Protein Encoded**	**Structural Phenotype**	**Observed Phenotype**	**References**
ida1	1α HC	Lacks inner arm I1 (f)	Slow swimming	[42], [89]–[91]
ida4	p28	Lacks inner arms a, c, d	Slow swimming	[42], [89], [90], [92]
oda2	γ HC	Lacks outer arms	Very slow swimming	[42], [72], [93]

After phenotypic selection, cells were allowed to grow on rich medium agar plates [94] for 2 days. Cultures were then scraped into tubes with 2 mL rich liquid medium (‘R medium’) [41], [94], [95], and allowed to grow for 48 hours under constant illumination at 25C.

2.3 Optical Microscopy Recordings

Uniflagellate cells were recorded using bright field microscopy on a Zeiss Universal Microscope (Carl Zeiss, Oberkochen, Germany) using a 40x Planapo oil-immersion objective with DIC optics. A sample was prepared by pipetting 20μL liquid culture onto an acid washed slide, and then covered by an 18x18mm coverslip. A periodically rotating cell was located by inspection and centered in the field of view. Microscope settings were then adjusted to provide maximum contrast between the flagellum and background. Videos were recorded at 350 frames per second with 2.86 ms shutter speed at 320x240 pixel resolution using a Dragonfly Express IEEE-1394b Digital Camera System and FlyCapture software (Point Grey Research, Scottsdale, AZ). Each video was 1 second in length (around 350 frames), recorded in AVI format.

2.4 Viscosity

Media viscosity was increased through the addition of Ficoll 400 (Sigma Aldrich, St. Louis, MO), a 400 kD inert polysaccharide often used in biological filtration systems and in other viscosity studies [92], [96], [97]. A 40% w/v Ficoll solution was created by slowly mixing Ficoll lyophilized powder with autoclaved R medium [94] until no powder could be seen in the viscous solution. For increased viscosity trials, an appropriate volume of 40% w/v Ficoll solution was pipetted onto the appropriate liquid cell culture volume, such that the total examined volume was 20 μL at the specified viscosity. The Ficoll solution was pipetted with the liquid culture slowly to allow complete mixing of solutions, even at maximum viscosity. Viscosity of the mixed solution was verified in separate trials by an AR-G2 Rheometer (TA Instruments, New Castle, DE).

2.5 Image Processing

Videos were analyzed in Matlab™ (The Mathworks, Natick, MA) using custom algorithms. For each video, at least 200 consecutive frames were selected for optimal flagellum contrast. Only frames in which the flagellum was clearly visible were used. In addition, only videos in which the entire cell body and flagellum remain in the field of view were used. First, a region of interest around the cell body was selected to establish a cell-based reference frame (x',y') and laboratory reference frame (X,Y), as shown in Figure 2.1 [85]. The region of interest was then rotated 360 degrees in increments of 0.5 degree to develop a set of potential images, indexed by angular rotation. Each video frame was then compared to the entire generated set of rotated images and the angular rotation amount with the highest correlation to the given video frame was assigned as the 'true' orientation of the cell body (based on the selected region of interest)[85]. From this analysis we obtained angular rotation vs time (as shown in Figure 2.2).

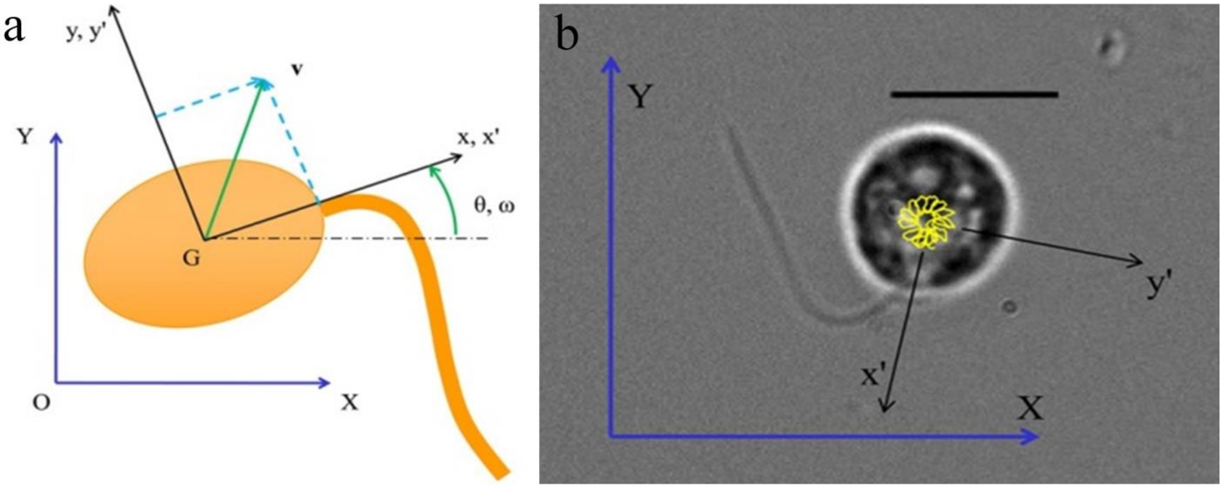

Figure 2.1 – Cell body registration
(a) Cell (x',y')and laboratory (X,Y) based reference frames shown on a cartoon of a uniflagellate *Chlamydomonas* cell. (b) Reference frames superimposed on one frame of a recorded uniflagellate cell, yellow trace shows tracked motion of the centroid of the cell body over the course of a full rotation (figure adapted from [85]).

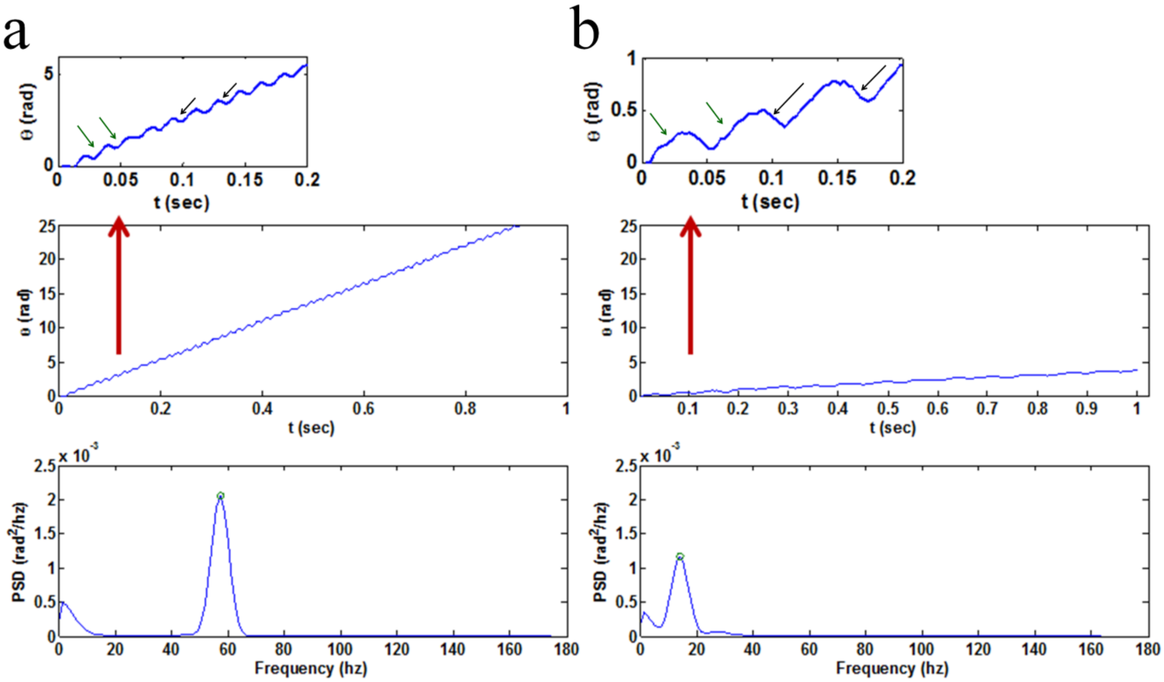

Figure 2.2 – Fourier analysis of uniflagellate cell rotation
Uniflagellate cell rotating in (a) regular 1.6 cP media, (b) high viscosity 6.2 cP media. Top image shows detailed section of cell body angle vs time demonstrating power stroke (green arrows) and recovery stroke (black arrows). Middle image shows 1 second of angular data, bottom image shows PSD of frequency data where peak indicates recorded beat frequency.

A power spectral density (PSD) estimate was obtained from the fast Fourier transform of the time-series of angular rotation data (*psd* function in MATLAB, The Mathworks, Natick, MA); the peak frequency was defined as the beat frequency of the cell. Increases in cell body angle (green arrows in insets, Figure 2.2) represent counter-clockwise rotation as a result of the power stroke of the flagellum, while decreases in angle (black arrows in insets, Figure 2.2) represent the backwards (clockwise) rotation of the cell during the recovery stroke. The overall positive trend in the slope of the angle vs. time curve indicates the rotation rate of the given cell (faster cells have a higher angle vs time slope).

The number of full cell body rotations per second was calculated from a linear fit to the angle vs time data, converted to rotations by dividing by 2π radians per rotation [85]. The number of beats per revolution was then calculated from:

$$Beats\ per\ Revolution = \frac{Beat\ Frequency\ (Hz)}{Rotations\ per\ Second} \tag{2.1}$$

2.6 Waveform Analysis

Rigid body rotation and translation algorithms could be used to characterize swimming and spinning speeds of either biflagellate or uniflagellate cells, however to understand waveform properties and changes we developed additional protocols to isolate and mathematically describe the axoneme shape in every frame. Wild-type *Chlamydomonas* flagella typically beat around 50-60 Hz, thus when recording at 350 frames/second only ~6-7 frames per beat can be collected. Because of mismatch between sampling frequency and flagellar beat frequency, the phase of flagellar waveforms in the frames collected varies relatively evenly over the entire beat cycle [85]. In order to increase the time density of waveform information, we assume periodicity of the beating flagellum and re-organize individual video frames into one stereotypical waveform per cell recorded [85].

While microscope settings were optimized at the time of recording, often video frames were difficult to process using only automatic selection procedures. To improve contrast between the flagellum and background, the stack of individual images was first optimized to remove artifacts and the region containing the flagellum was manually selected to reduce the total amount of stored data. Image stacks were exported to .avi files and opened in ImageJ [98]. The flagellum was manually traced in each frame, and then saved again as an .avi with increased contrast. The traced videos were then imported back to the original processing file in Matlab as a stack of images (Figure 2.3).

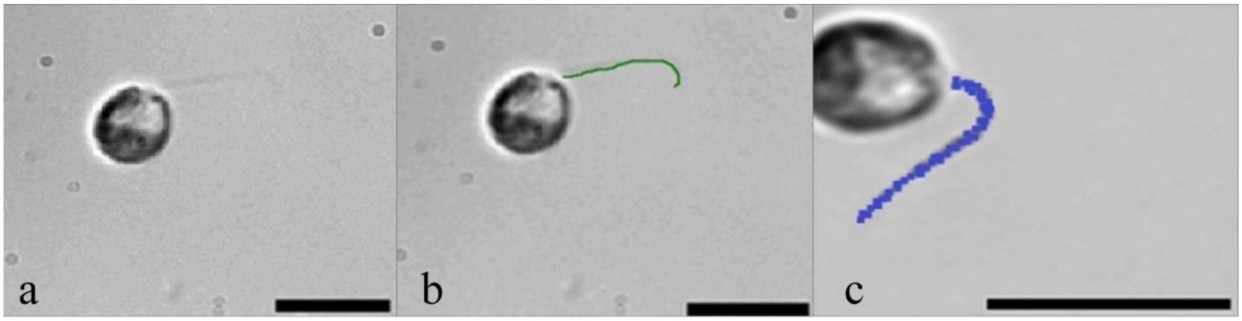

Figure 2.3 – Waveform tracing steps.
(a) Image from recorded video file displaying poor flagellar contrast, (b) traced image, (c) cloud of 100 points (blue) fitted to traced flagellum. Scale bar, 10µm.

To quantify the shape of the flagellum in each image, a ‘cloud’ of 100 points was assigned to the darkest pixels in each of the enhanced images in the traced video stack (Figure 2.3(c)). Each frame was reviewed for misalignments and artifacts, which were corrected by hand. The Isomap algorithm [99] was used to correlate point clouds throughout multi-dimensional space, aligning images based only on progress through the characteristic beat (phase) instead of through recorded time. A series of unsorted point clouds is shown in Figure 2.4(a). Point clouds sorted by phase similarity by Isomap are shown in Figure 2.4(b) [85], [99].

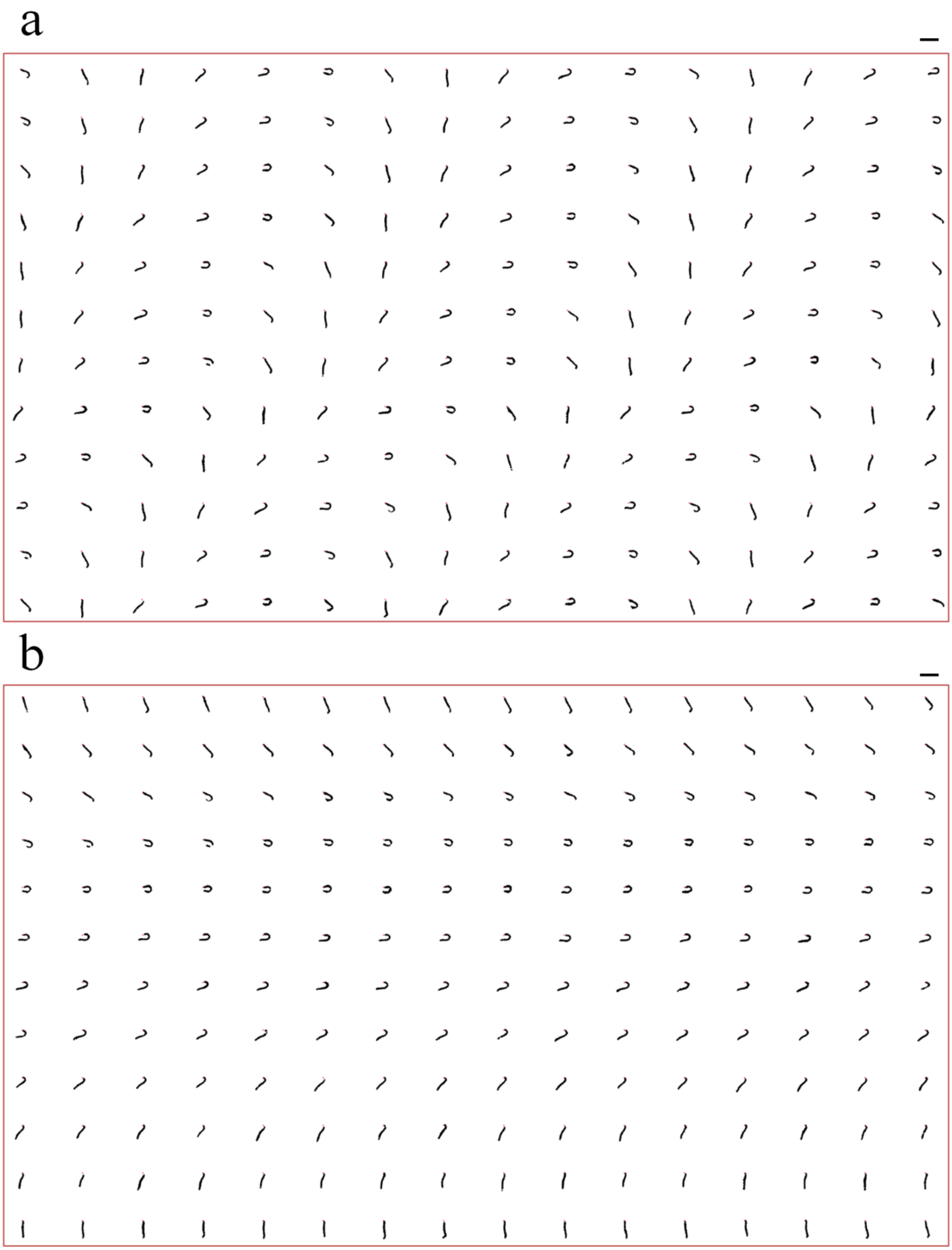

Figure 2.4 – Demonstration of Isomap sorting
(a) Unsorted point clouds. Recorded frames progress left to right, top to bottom. (b) point clouds after phase sorting by Isomap [99]. Scale bar 10 µm, upper right of each subfigure. [85]

The sorted point clouds still only describe discrete points along the flagellum in space and time, however we can more concisely describe the flagellum as a curve of given length (measured for each cell). In each frame we calculated a 4th order polynomial describing the waveform, determining the coefficients through least-squares regression to the point cloud. The entire flagellar waveform can then be described in a concise, quantitative manner. By smoothing and interpolating in time and space, we can generate a complete time-periodic surface of position and shear angle (ψ) as a function of time and space, as shown in Figure 2.5 (data from point clouds shown in black, polynomial fits shown every 1/12th of a cycle to give an overall impression of the waveform).

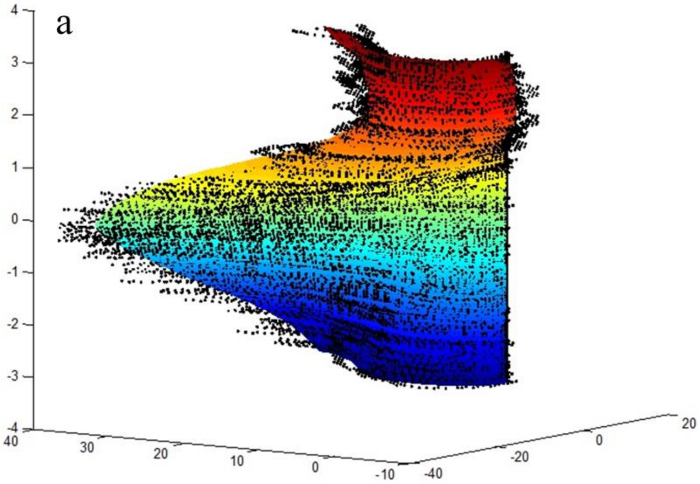

Figure 2.5 – Polynomial fit figures
(a) Smoothed surface of flagellar beat, color-coded by time (z-axis) with individual point clouds in black. (b) Polynomial fits every 1/12th period of data shown in (a). Scale bar 5 μm.

2.6 Post-Processing

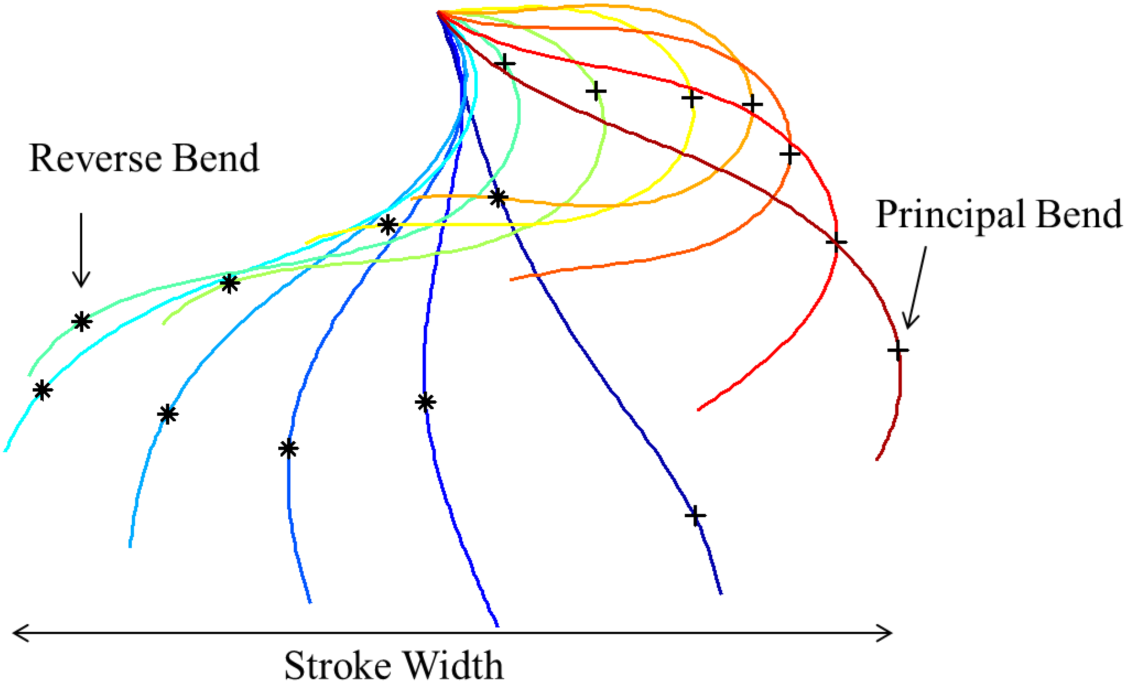

Figure 2.6 – General beat characteristics
Diagram of a typical waveform by polynomial fits every 1/12th period color-coded in time (blue to red) showing principal bend (negative curvature, marked with '+') and reverse bend (positive curvature, marked with '*', some markers removed for clarity). Stroke width is defined as the maximum x-distance between any points throughout the flagellar beat.

Following mathematical description of the flagellar beat in space and time, summary parameters were saved for further analysis. In particular, the matrix of angular data $\psi(s,t)$ in space and time was used to determine flagellar bend parameters such as:

- maximum and minimum curvature values in space and time $\frac{\partial\psi(s,t)}{\partial s}|_{max,min}$
- bend propagation speeds $\frac{\partial}{\partial t}(s^{kmax})$ for maximum curvature or $\frac{\partial}{\partial t}(s^{kmin})$ minimum curvature (where s^{kmax}, s^{kmin} are the spatial locations of the maximum or minimum curvatures, respectively)

- maximum and minimum sliding velocities $\frac{\partial\psi(s,t)}{\partial t}|_{max,min}$

A sample plot of normalized curvature ($L\frac{\partial\psi(s,t)}{\partial s}$), in space and time is shown in Figure 2.7; bend propagation speeds are shown by white and black lines fitted to the minimum and maximum curvatures, respectively. In addition, other parameters such as delay time between bends entering the flagellum were calculated from the output angular data (similar to calculations described [86]). These parameters were compared among loading and genetic conditions to analyze specific flagellar response to altered conditions or structure.

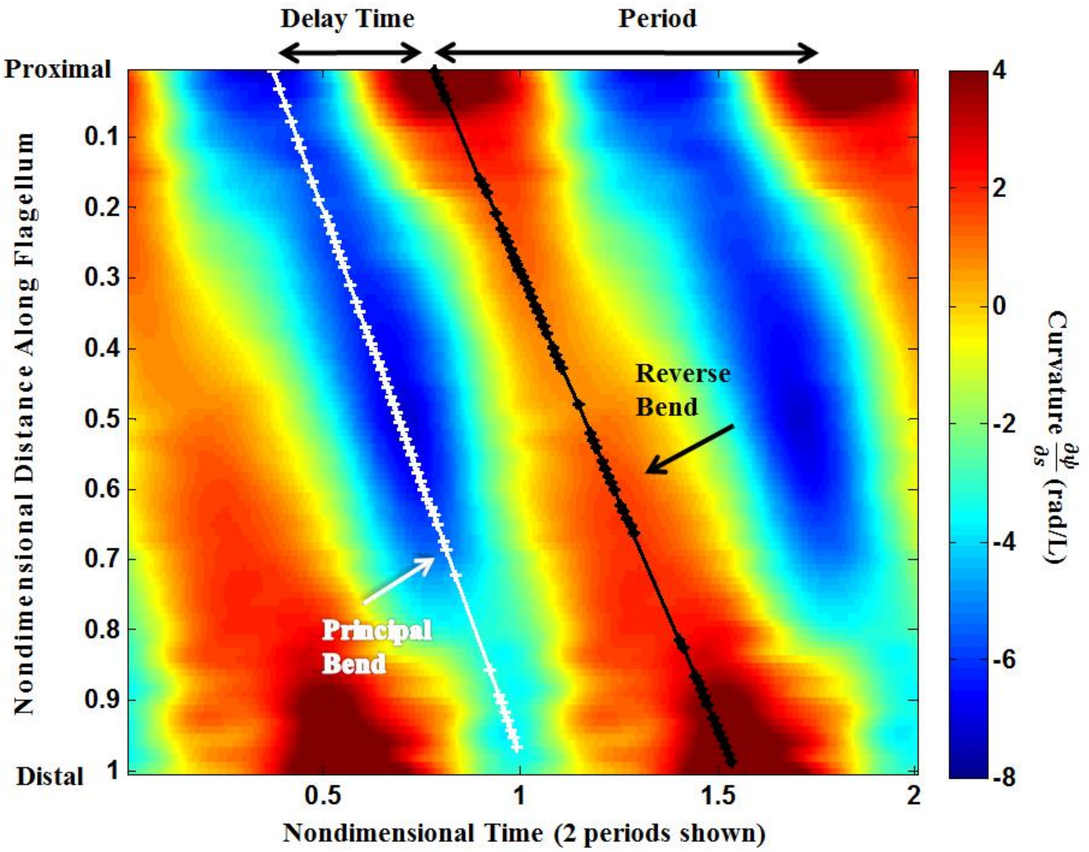

Figure 2.7 – Typical normalized curvature map
Normalized curvature $L\frac{\partial\psi(s,t)}{\partial s}$. Two periods (x-axis) vs nondimensional length along flagellum (y-axis), oriented so that flagellum origin is at the top left of figure (proximal and distal regions marked). Delay time is defined as the time from minimum negative curvature (principal bend initiation) to maximum positive curvature (reverse bend initiation) at the base of the flagellum

(normalized by period).

The experimental methods and image processing techniques outlined above enable quantitative description of the flagellar waveform in media of different viscosities. These methods condense large volumes of data (videos) into concise, quantitative descriptions of the flagellum in space in time. This quantitative description can be used to estimate curvatures, forces, bend propagation speeds, and other system parameters [86] to describe flagellar response to specific testing conditions. Mathematical quantification of the waveform can also be used to parameterize and validate computational models of flagellar behavior. Most waveform parameters are normalized by flagella length, L, or the beat frequency, f_b, or both.

Chapter 3

The Effects of Viscosity on Flagellar Waveform in Normal and Mutant Flagella

Flagella of wild-type and mutant *Chlamydomonas* axonemes (*uni1*, *ida1*, *ida4*, and *oda2*) were examined in regular and high viscosity media. Waveforms were quantified as described in Chapter 2 and parameters were analyzed with respect to structural mutation and viscosity.

3.1 Introduction and Motivation

The green alga *Chlamydomonas* has been used for many years to investigate flagellar behavior, however little is known about the flagellar response to increased loading. The response to varying external forces could help evaluate hypotheses concerning feedback control of dynein. Here we quantify waveform changes in uniflagellate *Chlamydomonas* at high viscosities, using methods described in Chapter 2. We observe a reduction in beat frequency with viscosity in the wild-type (*uni1*), γ HC (outer dynein arm) deficient (*oda2*), and p28 deficient (inner dynein arm a, c, d) (*ida4*) uniflagellate cells. Inner dynein arm mutant *ida1* (lacking the 1α HC of IDA1/f) continues to beat at high viscosities but alters its waveform to compensate for reduced force production in this high loading environment. All cell types produce significantly less power at high viscosity. The current results suggest that, in the absence of IDA1/f dynein, direct force feedback primarily in the outer dynein arm system leads to earlier switching in response to viscous loading. IDA1/f dynein delays the initiation of the recovery stroke and ensures a complete power stroke at all viscosities, perhaps by controlling inter-doublet separation.

3.2 Cell Body Parameters

At each viscosity and genetic mutation condition 10 cells were analyzed. The effects of viscosity were characterized (1) by the beat frequency and cell rotation rate, (2) by average force and power generated by the flagellum, and (3) by the flagellar waveform. Prior work [92], [100] has not addressed systematically the effect of viscosity on *Chlamydomonas* waveform, either in wild-type or dynein arm deficient flagella.

3.2.1 Beat Frequency and Rotation Rate

Data regarding beat frequency and beats per revolution was calculated from the overall cell body registration procedure [85]. Beat frequency decreased with increasing media viscosity for all cells. As shown in Figure 3.1, *oda2* cells decreased beat frequency significantly with increasing viscosity, while *ida1* cells were able to maintain beat frequency up to 8 cP. Cells missing outer arms were unable to beat at wild-type frequencies, as described by Minoura and Kamiya [100]. In contrast to prior work, our results did not show an increase in beat frequency at any viscosity. In addition, we observed *ida4* cells beating at high viscosities in comparison to the sharp decrease in beat frequency found by Minoura and Kamiya [100].

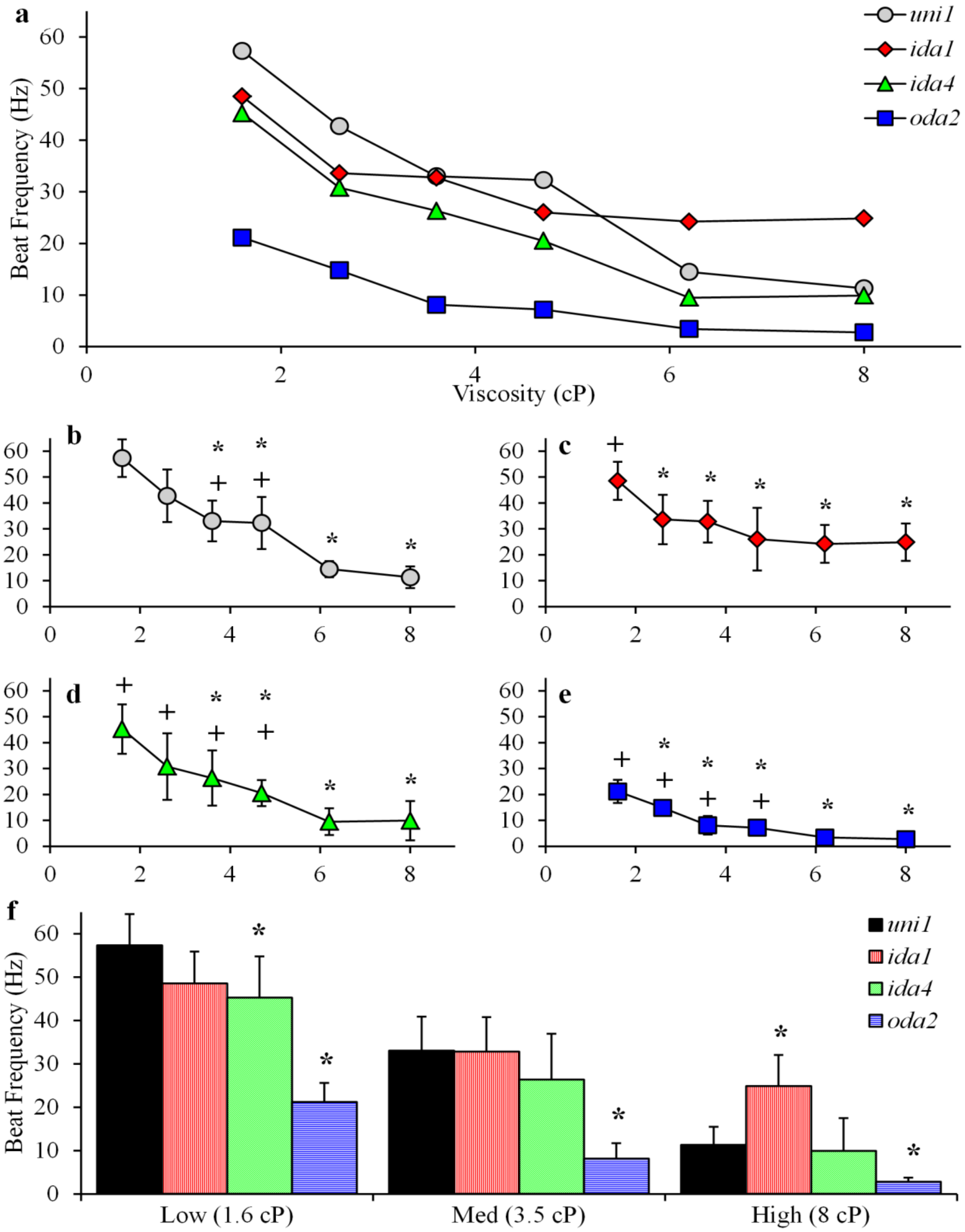

Figure 3.1 – Beat frequency vs viscosity
(a) Average beat frequency vs viscosity for all cells tested. Error omitted for clarity. Beat frequency significantly decreased with viscosity for each cell type by single factor ANOVA ($p<0.01$). (b-e) Individual cell type plots from (a) with error bars showing standard deviation. * indicates significant difference from beat frequency at 1.6 cP (baseline), ($p<0.01$ by two-tailed student t-test) + indicates significant difference from beat frequency at 8 cP ($p<0.01$ by two-tailed student t-test). (f) *ida4* and *oda2* cells beat significantly slower than *uni1* cells at 1.6 cP; *ida1* cells beat faster than *uni1* at 8cP ($p<0.01$ shown by *).

As expected, the number of cell body rotations per second decreased with viscosity (Figure 3.2). Subsequently, the number of flagellar beats per cell revolution was calculated by Equation (2.1). The number of beats per cell revolution increased for all cells (Figure 3.3), illustrating that cell rotation rate decreases faster than beat frequency as load increases. *ida1* and *uni1* cells displayed a significant increase in beats per revolution with media viscosity. *ida4* and *oda2* cells did not have a significant increase in beats per revolution with viscosity by single-factor ANOVA at the P<0.01 level.

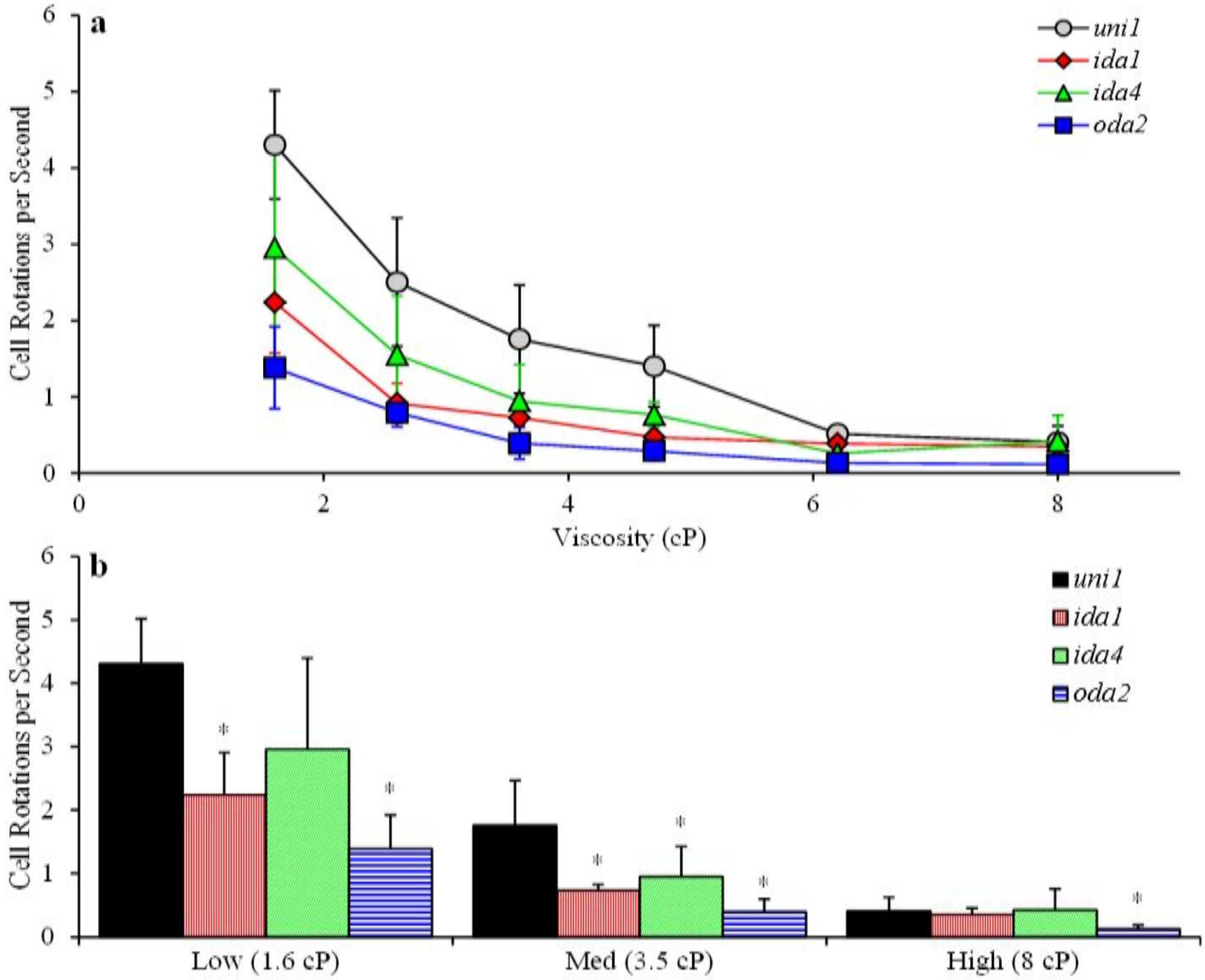

Figure 3.2 – Cell body rotations per second
(a) All cell types showed significant reduction in cell body rotations per second with increasing viscosity by 3.5 cP (p<0.01, ANOVA followed by paired t-test). (b) Among mutants, significant difference from *uni1* is given by (*) (p<0.01). Error bars show standard deviation.

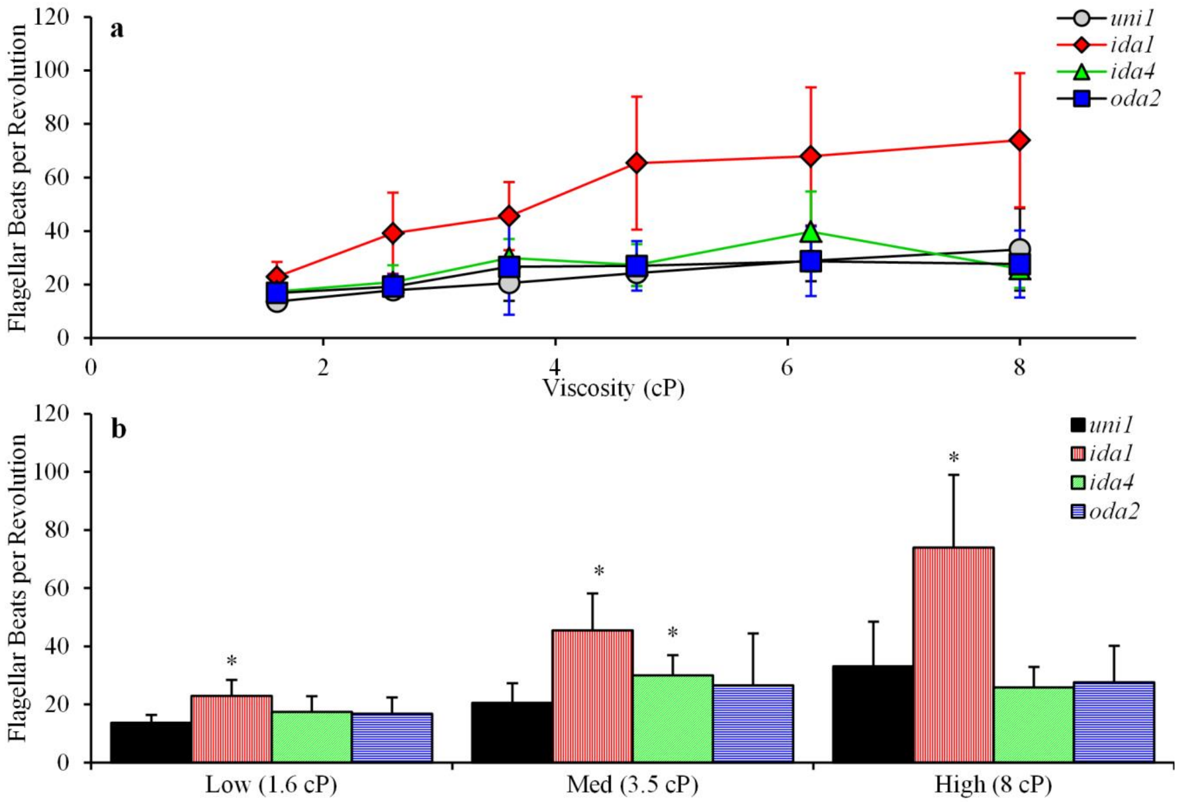

Figure 3.3 – Beats per revolution
(a) *uni1* and *ida1* showed significant variation with viscosity (ANOVA followed by paired t-test, $p<0.01$). (b) Among mutants, *ida1* was significantly higher than *uni1* at all viscosities (ANOVA followed by paired t-test $p<0.01$). Error bars show standard deviation.

3.2.2 Torque and Power

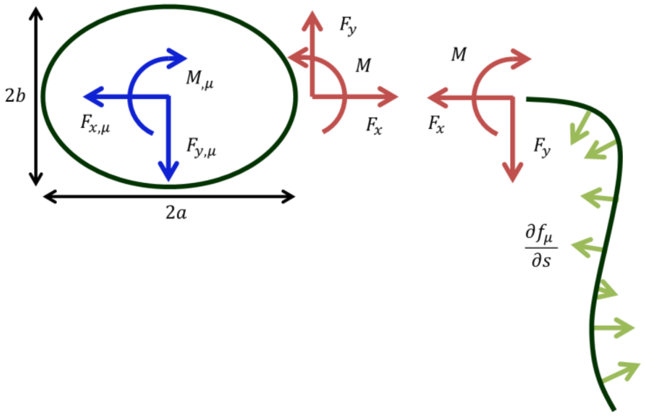

Figure 3.4 – Force balance between cell body and flagellum
Schematic showing cell body major axis $2a$ and minor axis $2b$. Assuming all forces and moments originate in the flagellum and are completely transferred to the cell body (red), the motion of the cell body through a viscous fluid reflects the flagellum force generation (blue forces and moment indicate cell body reaction forces to viscous load, which can be calculated from measurements of cell body motion and fluid mechanics).

Using angular rotation of the cell body and measurements of the minor and major axes of the cell, we calculated the average torque produced by each cell as described [86]. Briefly, the torque required to move the ellipsoid cell through a viscous fluid is proportional to viscosity of the fluid μ and rotation rate ω, along with shape parameters a, b, and C_{f3} (a nondimensional parameter ~1-1.4 derived from the eccentricity of the cell body) [86]:

$$M_\mu = 8\pi\mu ab^2\omega C_{f3} \tag{3.1}$$

The torque M_μ is equivalent to the average work per cell body revolution (Figure 3.5(a)). Dividing the average work per revolution by recorded beats per revolution we obtain the work per flagellum beat (Figure 3.5(b)).

Assuming the force exerted by the flagellum on the cell body occurs as shown in Figure 3.4, we convert from average torque to 'propulsive force' by dividing the torque by the major semi-axis dimension, a:

$$M_\mu = aF_y + F_x(\Delta y) \tag{3.2}$$

where Δy is the y-distance from the centroid of the cell body to the base of the flagellum. Assuming $\Delta y \approx 0$, the equivalent propulsive force from the flagellum is $F = \frac{M_\mu}{a}$. The power developed by the rotating cell body was calculated by multiplying torque by angular rotation rate: $P = M_\mu\omega$, data shown in Figure 3.6. All cells showed a significant decrease in power with viscosity, force and power values are comparable to prior work [100]. Wild-type axonemes (*uni1*) are able to produce the most force and power. Both *ida4* and *ida1* cells are able to produce work at high viscosities (Figure 3.5), however the lower magnitude of force and slower rotation rate (Figure 3.2) of *ida1* cells means they are unable to produce as much power at high viscosities (Figure 3.6).

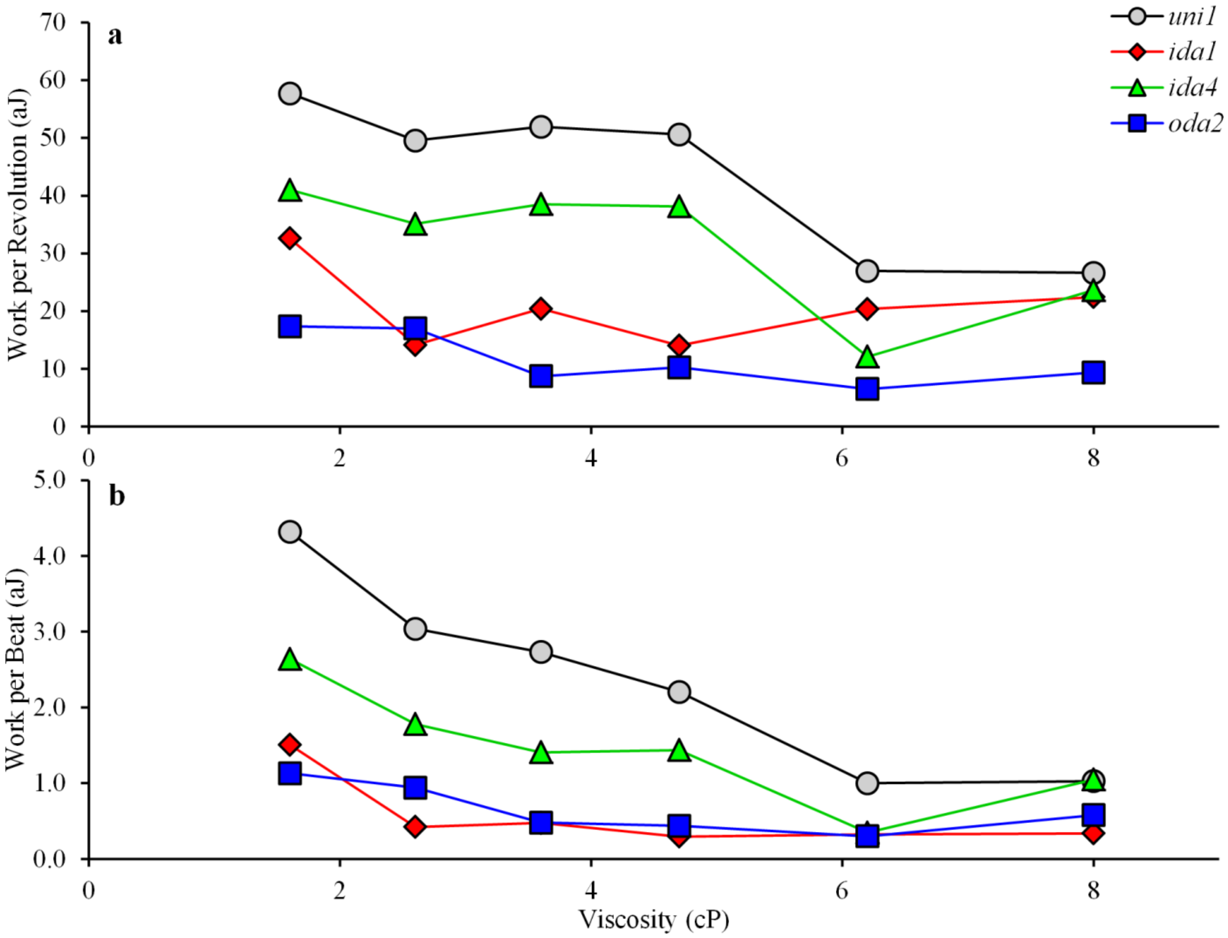

Figure 3.5 – Work generated by the flagellum vs viscosity
(a) All cells showed significant variation in average work per revolution with viscosity (ANOVA $p<0.01$). (b) All cells showed significant variation in work per flagellum beat with viscosity (ANOVA $p<0.01$, standard deviations omitted for clarity). Calculating the work per beat emphasizes lower average torque production of *ida1* flagella, despite sustained beat frequency at high viscosity. Error bars omitted for clarity.

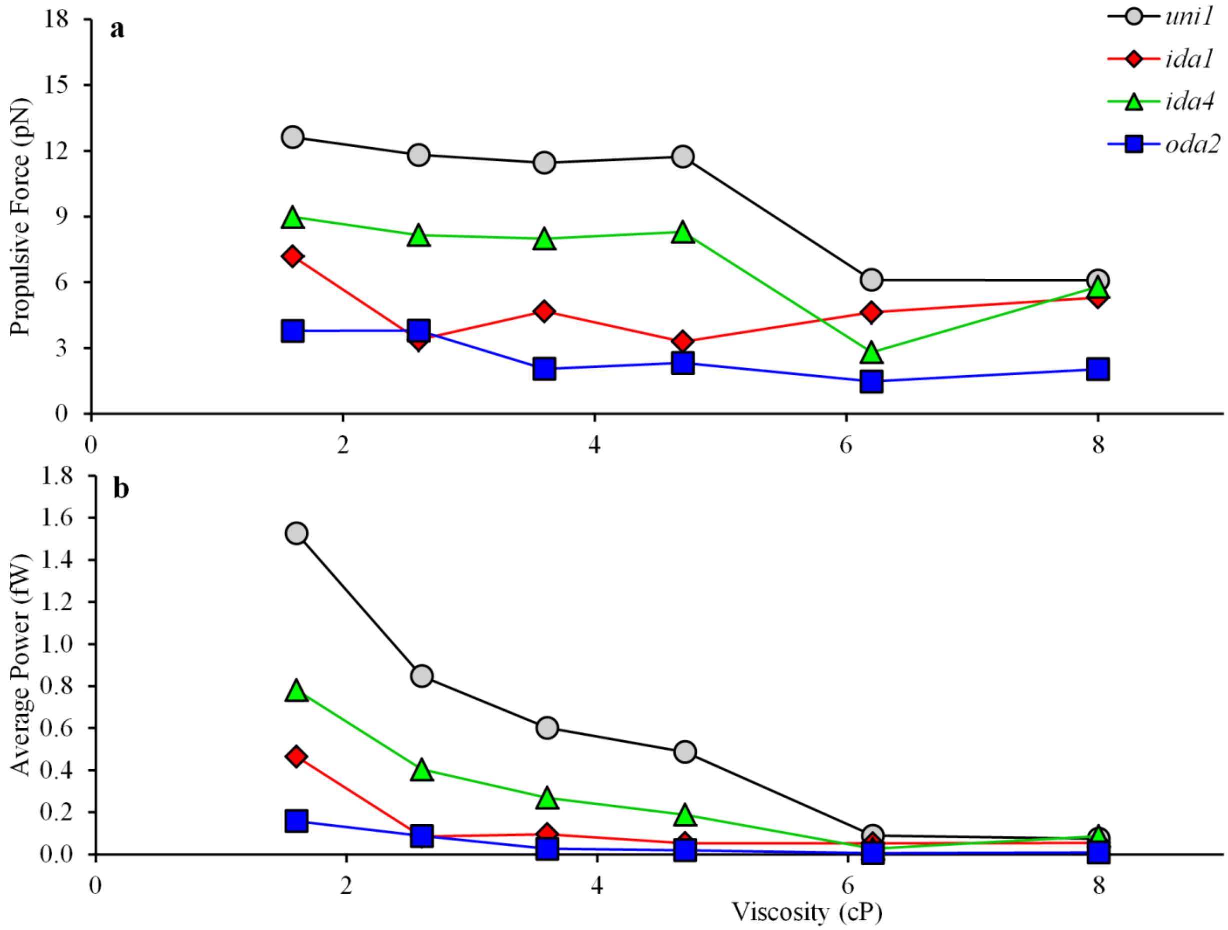

Figure 3.6 – Propulsive force and power vs viscosity
(a) Propulsive force calculated from Equation (3.2). *uni1, ida1,* and *oda2* cells showed significant variation in propulsive forces with viscosity (ANOVA, $p<0.01$) (b) *uni1* cells generate much more power than axonemal mutants, and are able to develop the most power in regular 1.6 cP media. Change in power with viscosity was significant for all mutants (ANOVA, $p<0.01$, standard deviations omitted for clarity). These values are close to previous estimates of propulsive force and power in biflagellate cells [92], [100]. Error bars omitted for clarity.

3.3 Waveform Parameters

Representative cells from selected experimental conditions are shown in Figure 3.7a. Each subfigure displays the polynomial fit to the observed flagella shape, at intervals of 1/12th beat period, to provide an image of the waveform. In these cells, beat shape exhibited changes in response to increased media viscosity, most noticeably as reduced stroke width. In all mutant cells, the most distal part of the flagellum displays higher curvature values at higher viscosities

(Figure 3.7b). Mutants displayed variable response to increasing viscosity; *ida1* in particular displayed a reduced stroke width at high viscosity. Figure 3.7b shows the curvature plots over space and time for the same individual cells plotted in Figure 3.7a.

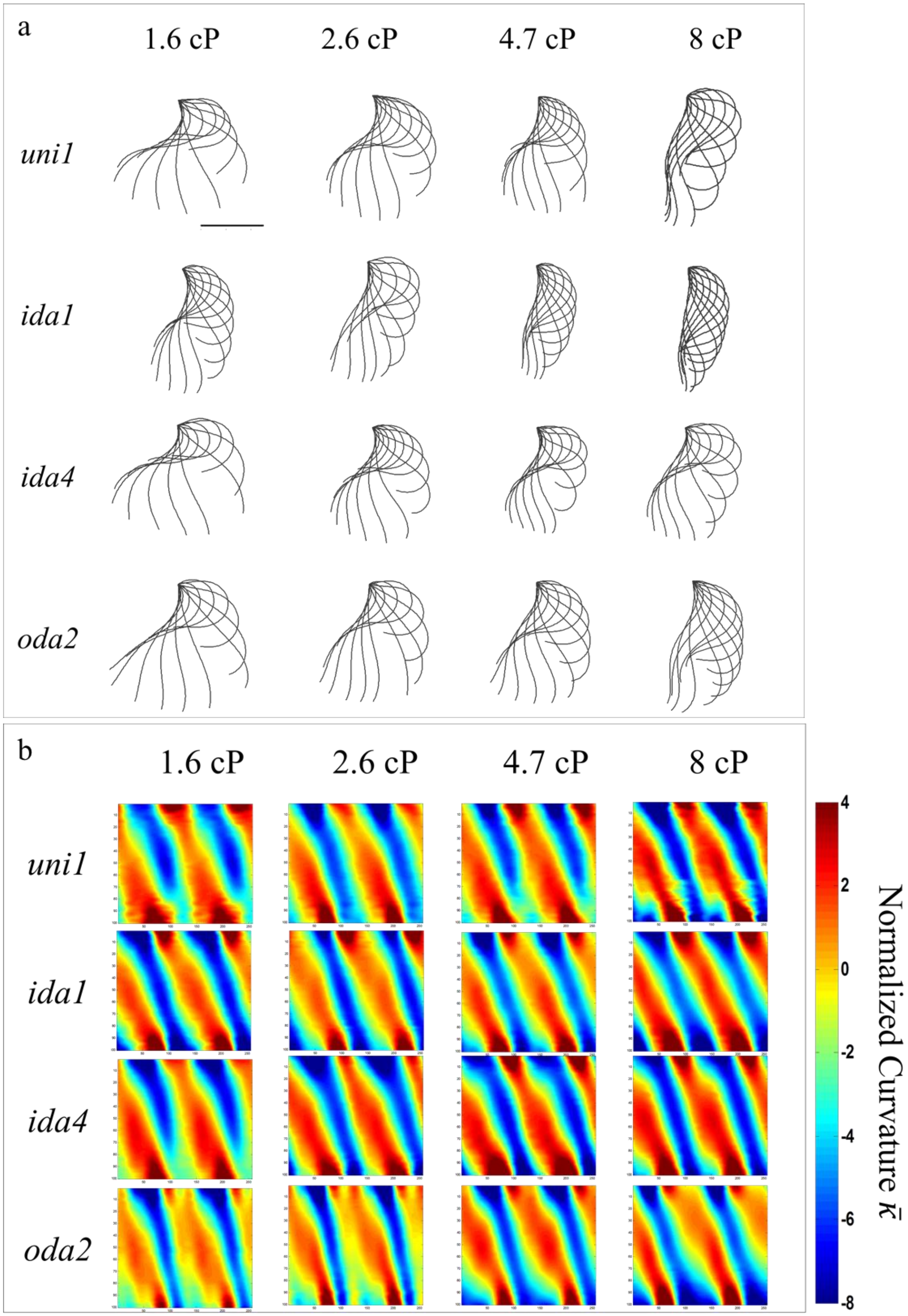

Figure 3.7 – Characteristic waveforms for selected experimental conditions.
Viscosity of media given by column, genetic mutation shown by row. (a) Polynomial fits to characteristic cells every 1/12th period, scale bar 5 μm. (b) Corresponding plot of normalized curvature $\bar{\kappa}$ plotted vs non-dimensional time (x-axis) and space (y-axis).

3.3.1 Beat Width

To quantify waveform parameters, the characteristics of sequential polynomial fits were investigated. The apparent trend of reduction in beat width with viscosity (Figure 3.8) was quantified by calculating the maximum x-distance across the dataset in both space and time to determine the parameter ‘stroke width’. Consistent with inspection, *ida1* cells had a significantly reduced stroke width at increased viscosity levels. Of the other mutants examined, a decrease in stroke width was only found to be significant in *uni1* cells at viscosities over 3.5 cP.

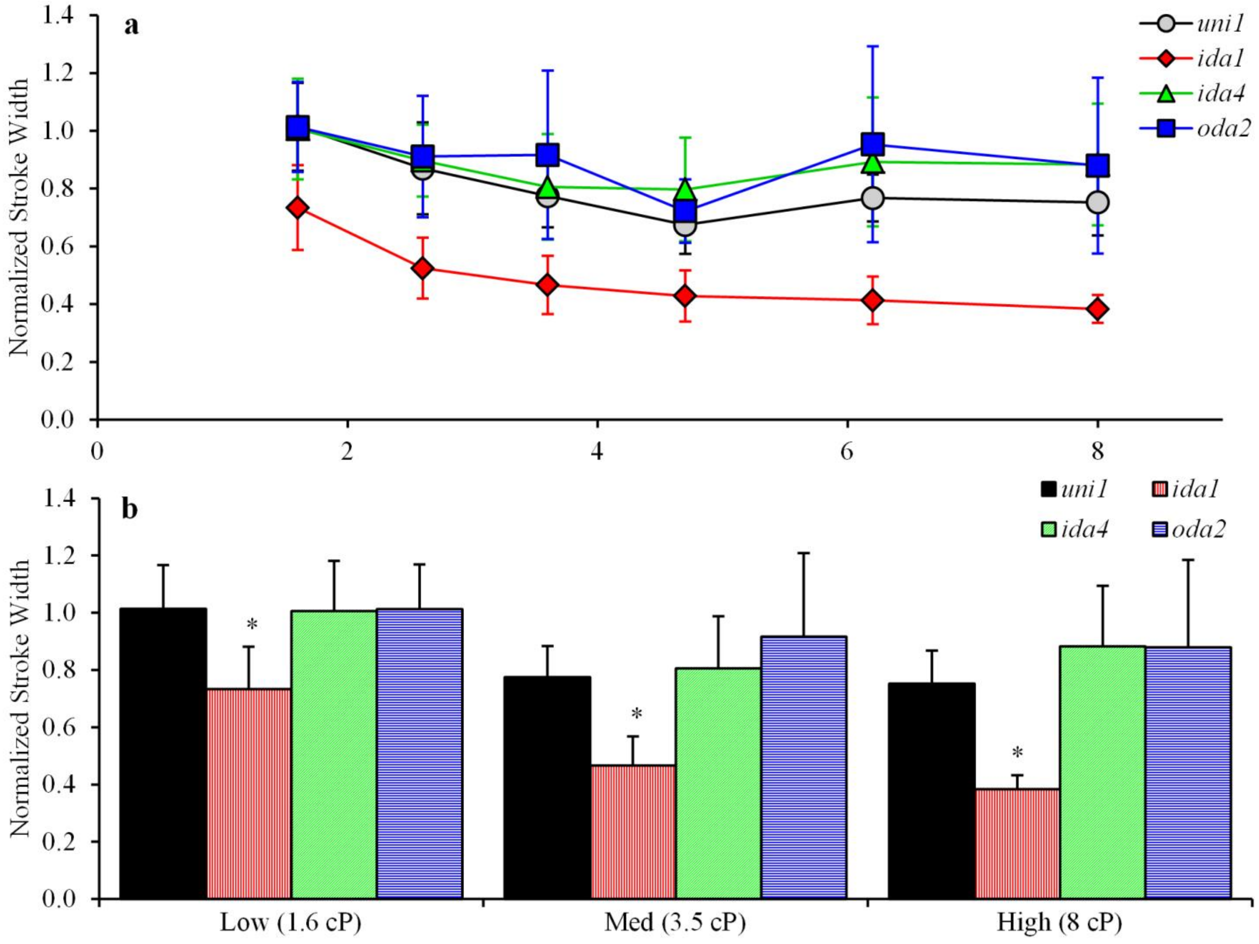

Figure 3.8 – Normalized flagellar stroke width
Maximum x-distance between any points in flagellar beat, normalized by *L*. (a) *uni1* and *ida1* showed significant variation in stroke width with viscosity (ANOVA, $p<0.01$) (b) Significant differences in stroke width between *uni1* and *ida1* were identified at all viscosities (paired t-test, $p<0.01$). Error bars show standard deviation.

3.3.2 Curvature Values

Values of minimum and maximum curvature correspond to the principal and reverse bends, respectively. It is important to note the principal bend (negative curvature) characterizes the recovery stroke, while the reverse bend (positive curvature) characterizes the power stroke. As shown in Figure 3.9, only *uni1* cells displayed a significant increase in the magnitude of both negative and positive curvature with viscosity. Note all curvature values are normalized by flagellum length and beat period.

By inspection, *ida1* cells appear to increase in curvature (Figure 3.7), yet maximum or minimum curvature values do not exhibit significant changes (Figure 3.9). To elucidate specific waveform changes with viscosity, we considered the mean of the absolute value of the flagellum curvature over its entire length. As shown in Figure 3.10, the average absolute curvature for *ida1* cells remained nearly constant with increasing viscosity, while *uni1* average absolute curvature increased significantly ($p<0.01$) and *oda2* average absolute curvature decreased (not significant) with viscosity.

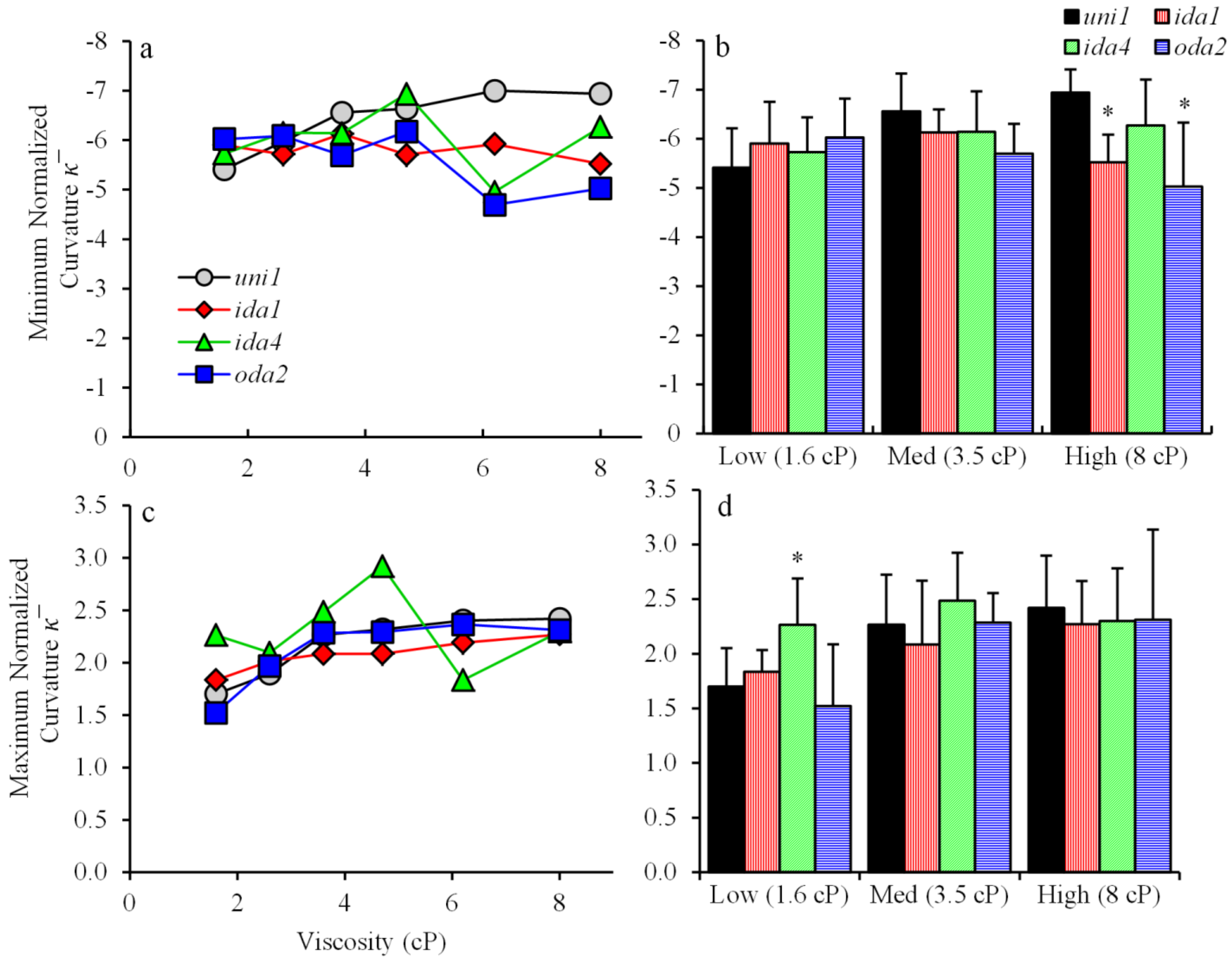

Figure 3.9 – Maximum and minimum normalized curvature values $\bar{\kappa}$

Curvature values normalized by $\frac{\partial \psi}{\partial s}|_o = \frac{1}{L}$ rad/µm. (a) *uni1*, *ida4*, and *oda2* cells had significant variation in minimum negative curvature with viscosity (ANOVA, p<0.01), however only *uni1* displayed a significant trend in increasing magnitude of negative curvature with viscosity (paired t-test between viscosities, p<0.01). (b) Comparison among mutants shows only a significant difference between *uni1* and *ida1*, *oda2* at high viscosity (student t-test following ANOVA, both p<0.01). (c) *uni1*, *ida4*, and *oda2* cells had significant variation in maximum positive curvature with viscosity (ANOVA, p<0.01), both *uni1* and *oda2* displayed a significant trend in increasing magnitude of curvature with viscosity (t-test between viscosities, p<0.01). (d) Significant variation between mutants was detected at low viscosity (ANOVA, p<0.01) with subsequent analysis revealing only a significant difference between *uni1* and *ida4* (p<0.01). (a,c) Error bars omitted for clarity (b,d) Error bars show standard deviation.

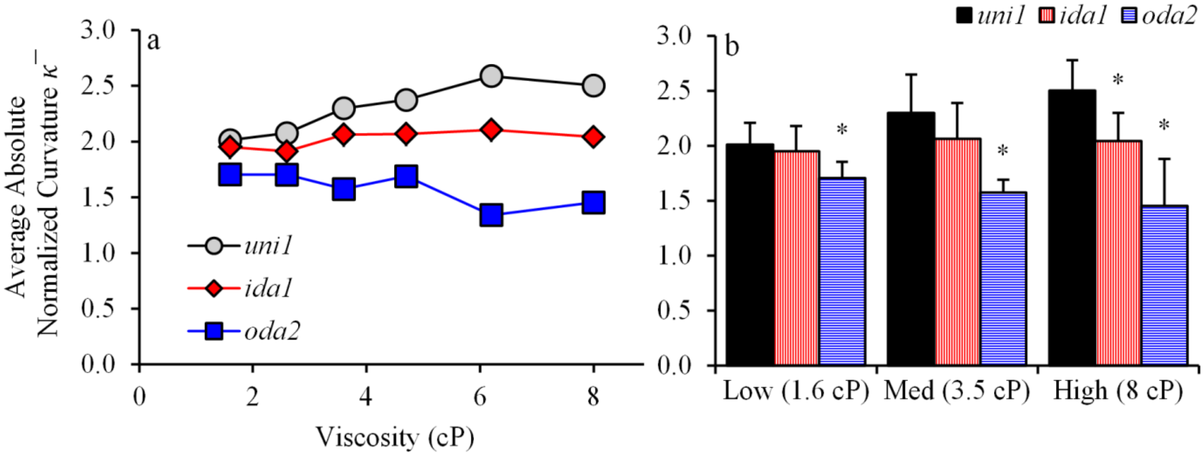

Figure 3.10 – Average normalized absolute curvature
Mean of absolute value of normalized curvature $\bar{\kappa}$. (a) Average of absolute value of curvature over the entire length of the flagellum at every point in time. Only *uni1* showed significant variation in total absolute curvature (ANOVA, p<0.01). *ida4* data and standard deviations omitted for clarity. (b) o*da2* differed significantly from *uni1* at all viscosities (p<0.01), error bars show standard deviation.

3.3.3 Bend propagation speeds

The propagation speeds of principal and reverse are shown in Figure 3.11. Propagation speeds are normalized by flagella length and beat frequency ($v_0 = Lf_B$) to account for the effects of very low beat frequencies. The propagation speed of maximum curvature, $\frac{\partial}{\partial t}(s^{kmax})$, gives the average velocity of the reverse bend (which drives the power stroke) as it propagates from the base to the tip of the flagellum. Likewise, the propagation speed of the minimum curvature point, $\frac{\partial}{\partial t}(s^{kmin})$, gives the proximal-to-distal velocity of the principal bend (characterizing the recovery stroke). The propagation speeds of the minimum curvatures are always higher than the propagation speed of the maximum curvature (Figure 3.11). *oda2* mutants show the greatest difference between propagation speeds of the minimum and maximum curvature, consistent across all viscosity levels.

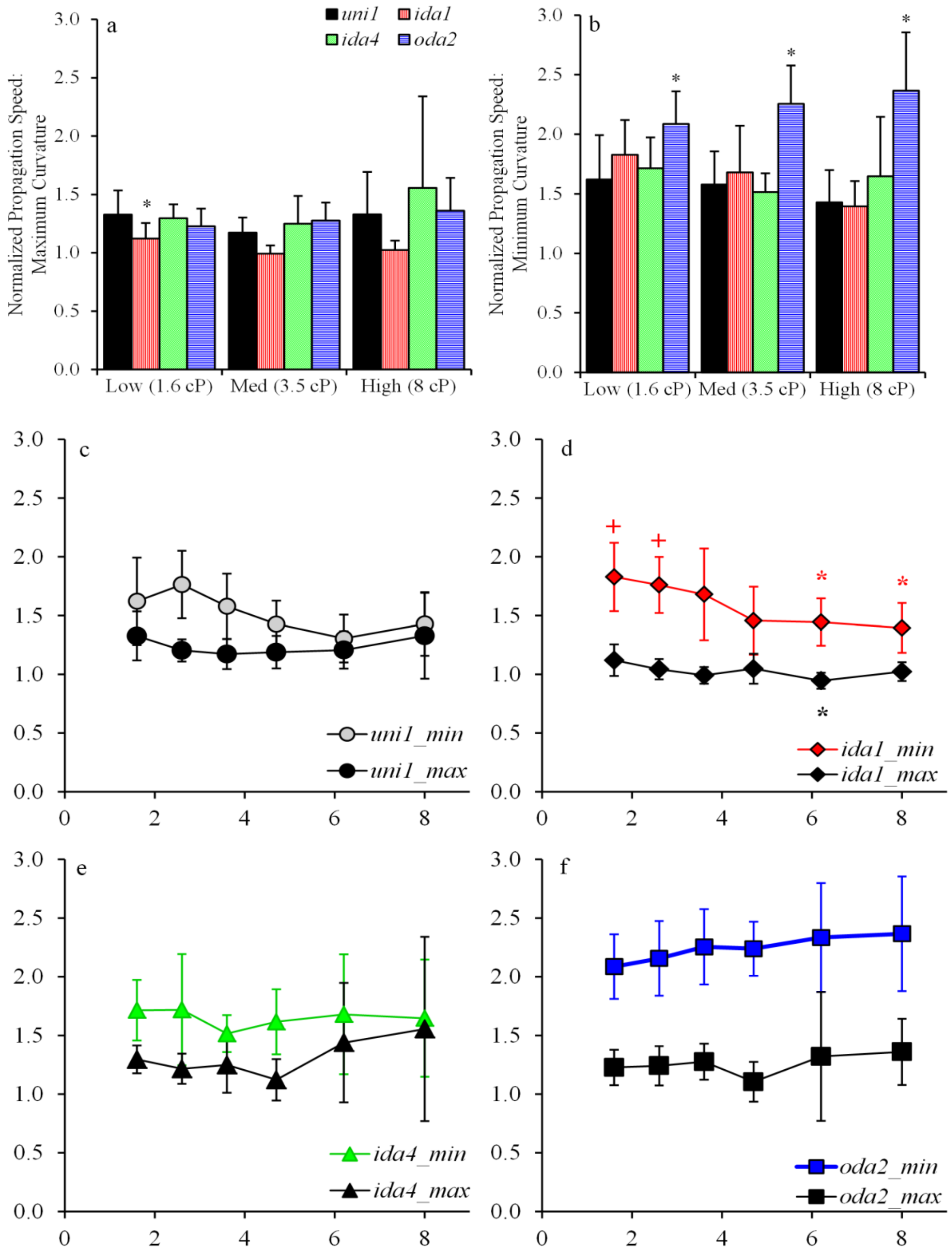

Figure 3.11 – Normalized bend propagation speeds
Bend propagation speeds normalized by $v_0 = Lf_B$. (a) There was no significant trend in maximum curvature (reverse bend, power stroke) propagation speed among mutants at different viscosities. (b) At all viscosities, *oda2* cells had significantly higher minimum curvature propagation (principal bend, recovery stroke, ANOVA p<0.01). (c-f) plots of maximum curvature (reverse bend, power stroke) and minimum curvature (principal bend, recovery stroke) propagation speed vs viscosity by cell type. Markers * and + indicate significant differences at a given viscosity and cell type from 1.6 cP, 8 cP values, respectively (p<0.01 by paired t-test). Error bars show standard deviation.

3.3.4 Delay Times

The delay time between the principal bend (minimum curvature) and reverse bend (maximum curvature) was calculated as shown (Figure 2.7). There were no significant trends in delay times with viscosity, however both *oda2* cells and *ida1* cells had significantly lower time delay at the base of the flagellum than *uni1* cells, particularly at low viscosities.

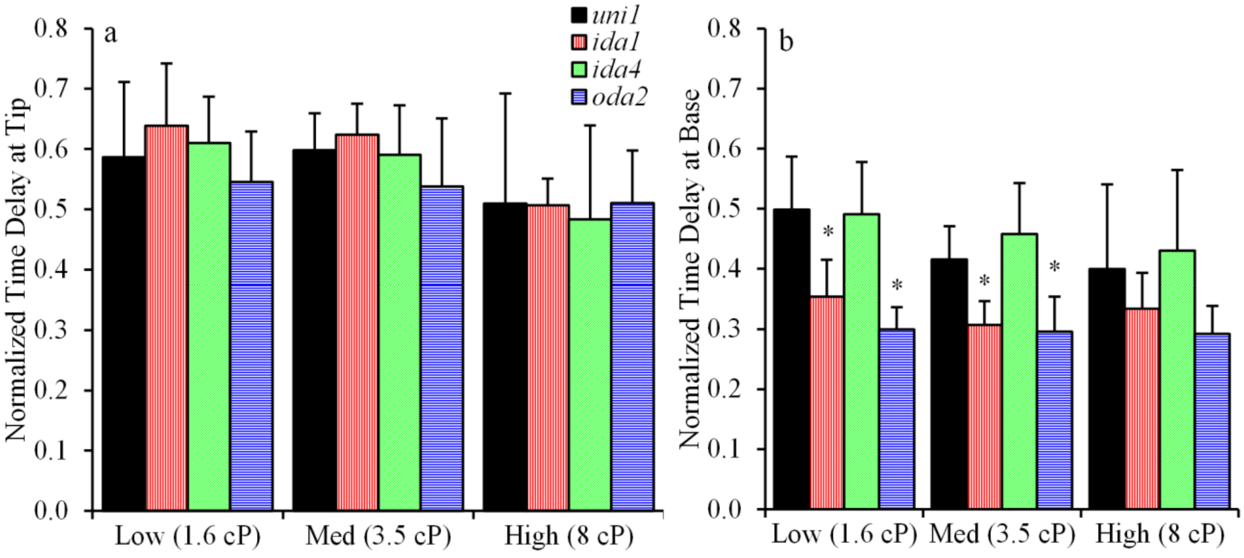

Figure 3.12 – Normalized delay times
Delay times were calculated as show in Figure 2.7, normalized by period. There were no significant trends in delay time with viscosity. (a) There were no significant trends in delay time at the tip of the flagellum among mutants at any viscosity level. (b) Among mutants, both *ida1* and *oda2* cells differed significantly from *uni1* time delay at the base of the flagellum ($p<0.01$). Error bars show standard deviation.

3.3.5 Power and Recovery Stroke Completion

We define the completion of a bend as the distance that bend has traveled down the length of the flagellum at the time the opposite bend enters the base of the flagellum. Power stroke completion describes the fraction of the flagellum the maximum positive curvature has traveled when the negative curvature enters the flagellum. Similarly, recovery stroke completion describes the fraction of the flagellum the minimum negative curvature has traveled down the length of the flagellum when the positive curvature enters the base of the flagellum. *ida1* cells have a significantly reduced power stroke completion relative to other cell types (Figure 3.13(a)). *oda2* cells have increased recovery stroke completion at all viscosities (Figure 3.13(b)).

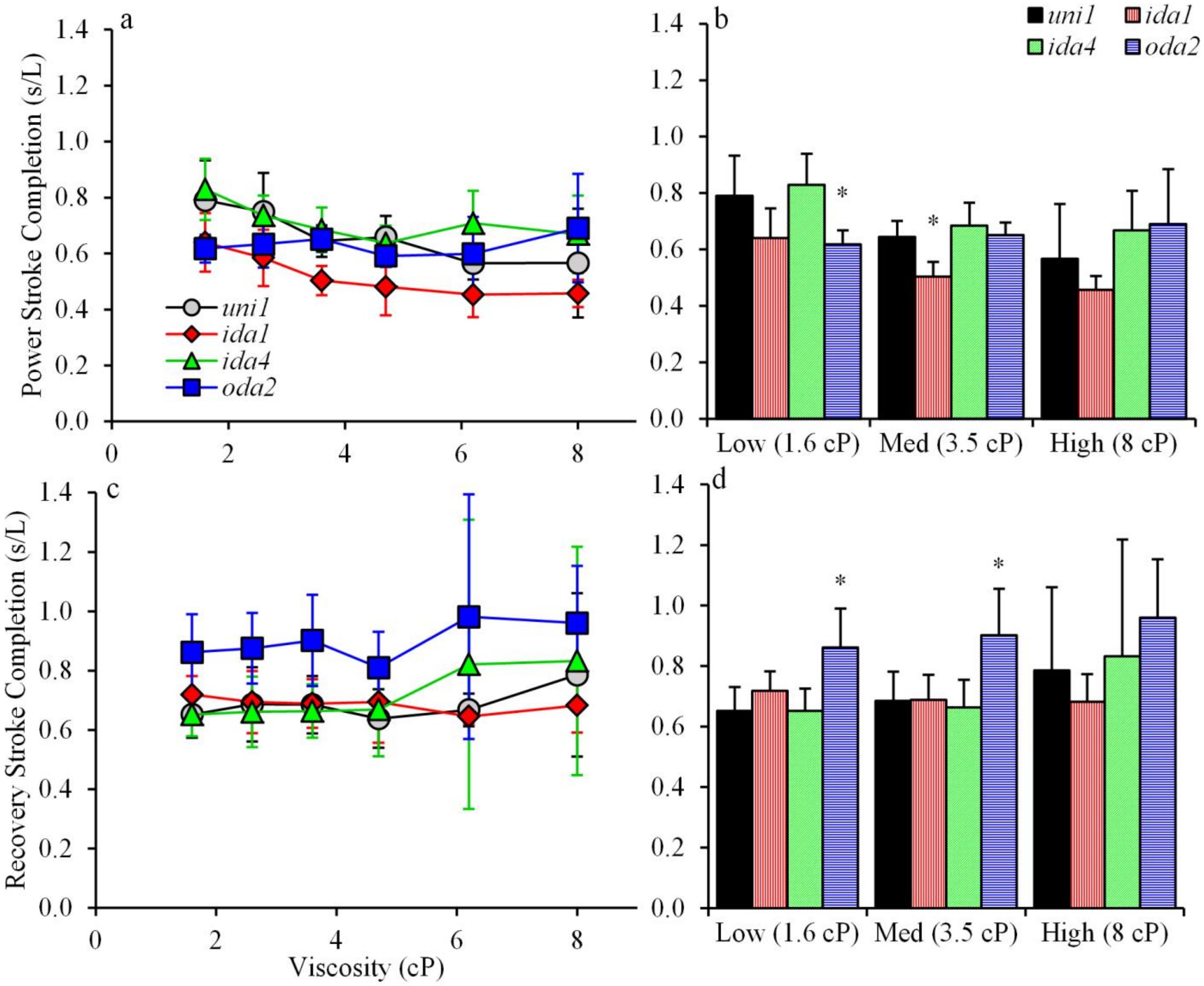

Figure 3.13 – Power and recovery stroke completion with viscosity
Completion is characterized by distance the bend propagates, normalized by flagellum length *L*, before the opposing bend begins. (a-b) Power stroke completion. (a) *ida1* cells have a reduced distance to positive curvature (power stroke) when the negative curvature (recovery stroke) enters the flagellum. (b) *oda2* and *ida1* cells differ significantly from *uni1* completion lengths at low and medium viscosities ($p<0.01$). (c-d) Recovery stroke completion. (a) *oda2* cells have an extended distance to negative curvature (recovery stroke) when the positive curvature (power stroke) enters the flagellum. (d) *oda2* cells have a significantly longer recovery stroke completion than *uni1* cells at low and medium viscosities ($p<0.01$). Error bars show standard deviation.

3.4 Discussion

We have shown that *Chlamydomonas reinhardtii* flagella respond to mechanical loading and to structural perturbations of the axoneme. Here we quantify not only general beat frequency characteristics, but also waveform characteristics, in media of increased viscosity. Genetic mutants with specific dynein-arm protein deficiencies displayed distinctly different waveforms under increased mechanical loading conditions.

Through cell-body registration we obtained information regarding the beat frequency of each flagellum (Figure 3.1). Cells lacking outer dynein arms (*oda2*) have a much lower beat frequency than *uni1* [92], [100]. As viscosity of media increases, *uni1*, *ida4*, and *oda2* cells respond by decreasing beat frequency. Notably *ida1* cells are able to maintain beat frequency after an initial decrease (at loading from 1.6 to 2.6 cP). These results are similar to the results of Minoura and Kamiya [100] which showed a decrease in beat frequency for *uni1*, *ida1*, *ida4*, and *oda1* biflagellate cells with increasing viscosity. In contrast, *ida4* cells in our experiments were able to continue beating past 2.6 cP and did not show any increase in beat frequency with viscosity. Both *oda1* and *oda2* mutants have complete loss of the outer dynein arms [93], thus we expect similar results between our observations of *oda2* and previous data from *oda1* [100]. We found good agreement between beat frequency values obtained in this study and from the literature [92], [100]. In comparison to [100] we have extended the range of viscosities studied and observe a drop in beat frequency above 6 cP for all mutants except *ida1*. Thus, even structurally wild-type axonemes react to increased loading by decreasing beat frequency. In addition, both *ida1* and *uni1* axonemes showed a significant increase in beats per revolution with viscosity. The key observation of this study is that *ida1* cells were able to continue rotating at high viscosities by dramatically increasing the flagellar beats per revolution.

In terms of the flagellar waveform, maximum and minimum curvature values did not change much with increased viscosity. *ida1* cells showed a significantly reduced beat width, as expected, however the biophysical cause of this reduction is not obvious. The incomplete power stroke of *ida1* axonemes (Figure 3.13(a)) along with total absolute curvature (Figure 3.10) suggest the reduction in *ida1* stroke width is due to early activation of the recovery stroke, not the actual minimum and maximum values of principal and reverse bend curvatures (Figure 3.9). In contrast, *oda2* cells are able to maintain a wide beat despite lower average curvature values (Figure 3.10). These cells complete more of the recovery stroke before the power stroke begins, allowing a wider stroke (Figure 3.13(b)).

Mutants lacking inner dynein arm I1/f respond to increased viscous loads by switching earlier in the power stroke. This implies a significant role for force feedback in regulating activity of dynein arms other than I1. King (2010) has described a mechanism for force-feedback in the outer dynein arms based on tension sensing by the γHC-LC1-LC4- microtubule complex [101]. Lindemann and his co-authors [79], [82] have presented a large body of evidence in support of a relationship between interdoublet-spacing, transverse force, and dynein activity. Since the transverse force is roughly proportional to the product of cumulative dynein force and curvature [84], it is plausible that at high viscosity the threshld levels of transverse force required for switching are reached earlier in the stroke. In contrast, mutants with I1 delay switching until the power stroke is complete. The differences in timing suggest that the primary role of the I1 dynein arm may be to restrict inter-doublet separation, and delay the point in the cycle when inter-doublet separation leads to switching. This effect is amplified in the mutants lacking outer dynein arms, suggesting that the outer arms may be most responsive to inter-doublet separation.

The *uni1* mutants were the only cell type to exhibit significant increases in curvature magnitudes with viscosity (Figure 3.9). This suggests that all dynein arms are required to produce enough force and power to affect flagella deformation at increased viscosity loads. Inner or outer dynein arms alone do not produce enough force to overcome the additional resistance; rather the flagella decrease their speed to reduce the viscous load. While maximum and minimum bend values are similar among genetic variants (Figure 3.9), the average curvature magnitudes (Figure 3.10) suggest that *oda2* cells maintain less force. Overall, this study provides evidence that both the outer dynein arms and inner-arm dynein I1 (f) are important for flagellar power generation, but that the differences in their behavior and roles are amplified at high viscosities.

This work has provided a basis for study of specific flagellar waveform response to mechanical loading. We have identified beat frequency and beats per cell revolution as important parameters in quickly estimating the ability of the flagellum to generate power, supported by in-depth waveform analysis. We have confirmed that inner arm dynein I1 (f) is particularly important for maintaining stroke width at high viscosities, while outer dynein arms are important for maintaining beat frequency at any viscosity [92], [93], [100], [102]. Both inner and outer arms appear to play a role in the feedback mechanism that produces oscillations. The methods presented give a dense mathematical description of periodic flagellar waveform, however more work remains to be done in applying these techniques to non-periodic observations.

Next steps include the comparison of experimental data with mathematical modeling schemes. Currently little work has been done to evaluate the predictive capabilities of various flagellar models – the data presented here may be helpful in evaluating models based on their predictions of flagellar response to increased viscosity. Finally, investigation of different structural mutants will continue to add insight regarding the specific roles of different motor proteins within the flagellar axoneme.

Chapter 4

Methods for Mathematical Modeling of Flagella Motion

Mathematical modeling of the flagellum is based on analysis of the flagellum as a slender beam in viscous fluid. In this chapter, the nonlinear governing equations of motion are derived from first principles following the method of Hines and Blum [78].

4.1 Introduction and Motivation

Mathematical models are formal, quantitative hypotheses about the mechanisms of observed processes; their main function is to lend insight to the driving forces behind those processes. Models are most useful when they can be directly tested by comparison to quantifiable biological measurements. A complete model of all axoneme proteins may not be necessary for enhancing understanding of dynein regulation; even basic models help clarify the governing principles behind waveform generation. A good model is one that not only captures the behavior of the system under ‘normal’ conditions, but which is able to predict the performance of the system under different experimental tests.

4.2 Background

Brokaw mathematically confirmed the sliding filament theory of flagellar regulation [2] based on micrographs of Satir, 1965 [103]. Subsequently a full derivation of nonlinear beam mechanics was published in 1978 by Hines and Blum [78]. This model provides a concise description of the flagellum as a two-dimensional beam based on an understanding of solid mechanics and simple hydrodynamic resistance. The derived equations of motion accurately describe motion of a nonlinear slender beam in viscous fluid; the uncertainty in flagella models primarily lies in defining the force generation term (biologically, this corresponds primarily to the contributions of dynein arms to flagellar bending). Ambiguity in flagellar models surrounds this term, as the complete activation mechanism of the dynein motor remains unknown [75]–[77]. We hypothesize that mechanical feedback is important in the regulation of flagellar dyneins. In this chapter, I will review the basic assumptions of the Hines and Blum model and outline the derivation of the governing equations of motion. Both the sliding-controlled and geometric clutch models, as well as the original curvature-controlled model of Hines and Blum [78], are based on this initial nonlinear system of equations with different assumptions regarding the form of the active shear force term.

4.3 General Equations of Flagella Motion

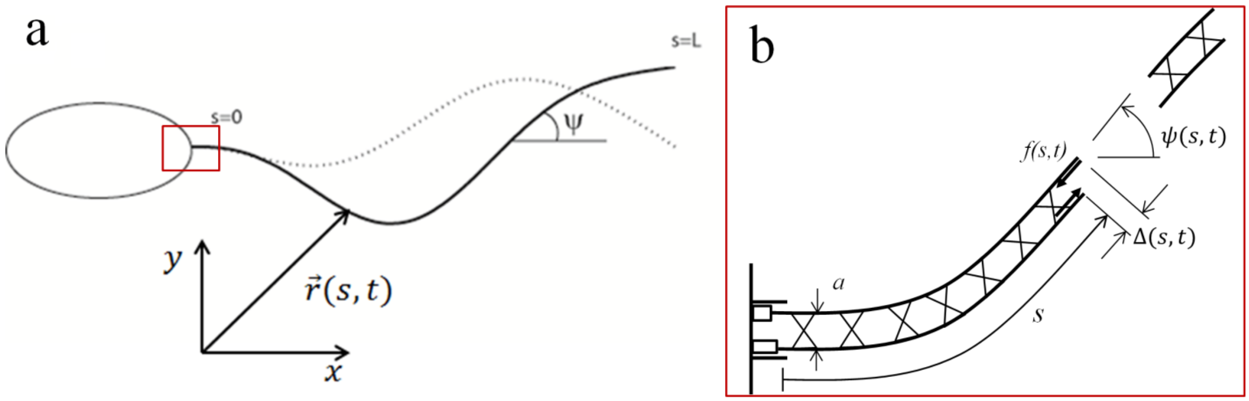

Figure 4.1 – Flagellum schematics
(a) Diagram of cell body and flagellum showing position vector $\vec{r}$ and tangent angle ψ. (b) Schematic of flagellum as cantilever beam showing tangent angle $\psi(s,t)$, displacement $\Delta(s,t)$, beam diameter a, and shear force $f(s,t)$.

This derivation follows the seminal paper of Hines and Blum (1978); some details are added for clarification. The flagellum is modeled as an elastic beam in viscous fluid driven by internal forces.

4.2.1 Kinematics

Flagella shape is defined by the tangent angle which may vary with respect to time and space, $\psi(s,t)$, as shown in Figure 4.1. Position along the beam is defined by the space variable s, located a vector $\vec{r}$ from the reference frame (Figure 4.1(a)). Following the original derivations of Hines and Blum, we define normal and tangent unit vectors relative to the beam:

$$\overrightarrow{e_T} = [cos\psi, sin\psi] = \frac{\partial \vec{r}}{\partial s} \tag{4.3}$$

$$\overrightarrow{e_N} = [-sin\psi, cos\psi] \tag{4.4}$$

Thus

$$\frac{\partial \overrightarrow{e_T}}{\partial s} = [-sin\psi, cos\psi]\frac{\partial \psi}{\partial s} = \frac{\partial \psi}{\partial s}\overrightarrow{e_N} \tag{4.5}$$

$$\frac{\partial \overrightarrow{e_N}}{\partial s} = [-cos\psi, -sin\psi]\frac{\partial \psi}{\partial s} = -\frac{\partial \psi}{\partial s}\overrightarrow{e_T} \tag{4.6}$$

4.2.2 Equilibrium Conditions

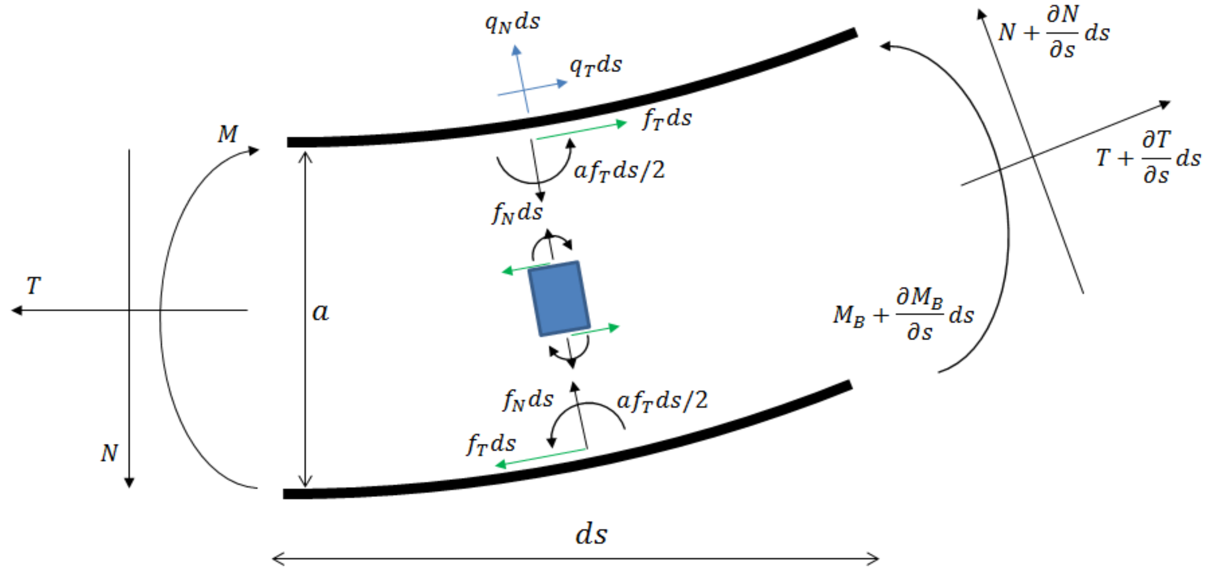

Figure 4.2 – Free body diagram of a differential element of a beam in viscous fluid
Tangential T and normal N force within the beam are shown along with internal moment M. Internal forces are lumped into the distributed force $f_T ds$ and distributed normal force $f_N ds$. Distributed viscous resistance in the tangential and normal directions is labeled $q_T ds$ and $q_N ds$, respectively. Internal active shear is balanced by an unknown internal resistance (blue rectangle) which can support normal and tangential forces as well as the applied moment due to dynein activity

Considering the flagellum as a single, continuous beam, we can define the developed tangential and normal forces at any point (T and N) over a differential element as shown in Figure 4.2. The active force component (dynein contribution to motion) is represented by the distributed shear force couple $f_T ds$ (green arrows) acting along the length of the beam. A force balance on the representative element shown in Figure 4.2 becomes (eliminating balanced forces):

$$\frac{\partial \vec{N}}{\partial s} ds + \frac{\partial \vec{T}}{\partial s} ds + \overrightarrow{q_N} ds + \overrightarrow{q_T} ds = 0 \tag{4.7}$$

Considering the identities $\vec{N} = \mathrm{N}\overrightarrow{e_N}; \vec{T} = \mathrm{T}\overrightarrow{e_T}$, using chain rule and Equations (4.5)and (4.6):

$$N \frac{\partial \overrightarrow{e_N}}{\partial s} + \frac{\partial N}{\partial s} \overrightarrow{e_N} + T \frac{\partial \overrightarrow{e_T}}{\partial s} + \frac{\partial T}{\partial s} \overrightarrow{e_T} + \overrightarrow{q_N} + \overrightarrow{q_T} = 0 \tag{4.8}$$

$$-N\frac{\partial\psi}{\partial s}\overrightarrow{e_T}+\frac{\partial N}{\partial s}\overrightarrow{e_N}+T\frac{\partial\psi}{\partial s}\overrightarrow{e_N}+\frac{\partial T}{\partial s}\overrightarrow{e_T}+q_N\overrightarrow{e_N}+q_T\overrightarrow{e_T}=0 \tag{4.9}$$

Separating into normal and tangential components:

$$-N\frac{\partial\psi}{\partial s}+\frac{\partial T}{\partial s}+q_T=0 \tag{4.10}$$

$$\frac{\partial N}{\partial s}+T\frac{\partial\psi}{\partial s}+q_N=0 \tag{4.11}$$

A moment balance about the left side of the beam (ignoring higher-order terms) gives:

$$\frac{\partial M_B}{\partial s}+N-af=0 \tag{4.12}$$

4.2.3 Constitutive Relations

To specify the normal and tangential distributed loads due to fluid, we consider resistive force theory [78], [104]. The fluid at very low Reynolds number (Stokes flow) is assumed to provide a force proportional but opposite to velocity [78], appropriate here due to the very small length scales (even for a biflagellate cell traveling at 100 µm/s in regular media, $Re \approx 3x10^{-10} \ll 1$). The velocity of any point along the flagellum can be written in terms of tangential and normal components: $\vec{v}=v_T\overrightarrow{e_T}+v_N\overrightarrow{e_N}$. The spatial derivatives of the components of velocity are (again, based on the identities of Equations (4.5) and (4.6)):

$$\frac{\partial v_T}{\partial s}=v_N\frac{\partial\psi}{\partial s} \tag{4.13}$$

$$\frac{\partial v_N}{\partial s}=\frac{\partial\psi}{\partial t}-v_T\frac{\partial\psi}{\partial s} \tag{4.14}$$

The viscous resistive force, q, can be written in component form as:

$$q_T=-c_Tv_T \tag{4.15}$$

$$q_N = -c_N v_N \tag{4.16}$$

Finally, the constitutive equation for the bending moment of a beam with flexural rigidity EI is needed to derive the complete equations of motion of the beam under the given constraints:

$$M_B = EI\frac{\partial \psi}{\partial s} \tag{4.17}$$

4.2.4 Derivation Steps

First, Equation (4.11) is combined with Equation (4.16) and differentiated with respect to space:

$$\frac{\partial N}{\partial s} + T\frac{\partial \psi}{\partial s} - c_N v_N = 0 \tag{4.18}$$

$$\frac{\partial^2 N}{\partial s^2} + T\frac{\partial^2 \psi}{\partial s^2} + \frac{\partial T}{\partial s}\frac{\partial \psi}{\partial s} - c_N\frac{\partial v_N}{\partial s} = 0 \tag{4.19}$$

Substituting Equation (4.14):

$$\frac{\partial^2 N}{\partial s^2} + T\frac{\partial^2 \psi}{\partial s^2} + \frac{\partial T}{\partial s}\frac{\partial \psi}{\partial s} - c_N(\frac{\partial \psi}{\partial t} - v_T\frac{\partial \psi}{\partial s}) = 0 \tag{4.20}$$

$$\frac{\partial^2 N}{\partial s^2} + T\frac{\partial^2 \psi}{\partial s^2} + \frac{\partial T}{\partial s}\frac{\partial \psi}{\partial s} - c_N\frac{\partial \psi}{\partial t} + c_N v_T\frac{\partial \psi}{\partial s} = 0 \tag{4.21}$$

Combining Equations (4.10) and (4.15):

$$c_T v_T = -N\frac{\partial \psi}{\partial s} + \frac{\partial T}{\partial s} \tag{4.22}$$

Combining Equations (4.22) and (4.21):

$$\frac{\partial^2 N}{\partial s^2} + T\frac{\partial^2 \psi}{\partial s^2} + \frac{\partial T}{\partial s}\frac{\partial \psi}{\partial s} - c_N\frac{\partial \psi}{\partial t} + \frac{c_N}{c_T}(-N\frac{\partial \psi}{\partial s} + \frac{\partial T}{\partial s})\frac{\partial \psi}{\partial s} = 0 \tag{4.23}$$

Thus, the beam tangent angle ψ may be described by net tangential forces T and normal forces N. Combining equations (4.12) and (4.17):

$$EI\frac{\partial^2\psi}{\partial s^2}+N-af=0 \tag{4.24}$$

Rearranging Equation (4.24) and substituting N and its spatial derivatives into Equation (4.23):

$$a\frac{\partial^2 f}{\partial s^2}-EI\frac{\partial^4\psi}{\partial s^4}+T\frac{\partial^2\psi}{\partial s^2}+\frac{\partial T}{\partial s}\frac{\partial\psi}{\partial s}-c_N\frac{\partial\psi}{\partial t}+\frac{c_N}{c_T}\left(\frac{\partial T}{\partial s}-\left(af-EI\frac{\partial^2\psi}{\partial s^2}\right)\frac{\partial\psi}{\partial s}\right)\frac{\partial\psi}{\partial s}=0 \tag{4.25}$$

Thus, we have an equation that relates the tension in the beam $T(s,t)$ and the tangent angle $\psi(s,t)$, to the internal shear force $f(s,t)$, and the constants a, EI, c_N, c_T .

Similarly, starting with Equation (4.10), combined with Equation (4.15) and taking a spatial derivative:

$$-N\frac{\partial^2\psi}{\partial s^2}-\frac{\partial N}{\partial s}\frac{\partial\psi}{\partial s}+\frac{\partial^2 T}{\partial s^2}+-c_T\frac{\partial v_T}{\partial s}=0 \tag{4.26}$$

Substituting Equation (4.13):

$$-N\frac{\partial^2\psi}{\partial s^2}-\frac{\partial N}{\partial s}\frac{\partial\psi}{\partial s}+\frac{\partial^2 T}{\partial s^2}+-c_T v_N\frac{\partial\psi}{\partial s}=0 \tag{4.27}$$

Combining Equations (4.11) and (4.16):

$$c_N v_N=\frac{\partial N}{\partial s}+T\frac{\partial\psi}{\partial s} \tag{4.28}$$

Combining Equations (4.27) and (4.28):

$$-N\frac{\partial^2\psi}{\partial s^2}-\frac{\partial N}{\partial s}\frac{\partial\psi}{\partial s}+\frac{\partial^2 T}{\partial s^2}-\frac{c_T}{c_N}\frac{\partial\psi}{\partial s}(\frac{\partial N}{\partial s}+T\frac{\partial\psi}{\partial s})=0 \tag{4.29}$$

Substituting for N (from Equation (4.24)) and its first spatial derivative:

$$-(af-EI\frac{\partial^2\psi}{\partial s^2})\frac{\partial^2\psi}{\partial s^2}-(a\frac{\partial f}{\partial s}-EI\frac{\partial^3\psi}{\partial s^3})\frac{\partial\psi}{\partial s}+\frac{\partial^2 T}{\partial s^2}+\frac{C_T}{C_N}\frac{\partial\psi}{\partial s}((a\frac{\partial f}{\partial s}-EI\frac{\partial^3\psi}{\partial s^3})+T\frac{\partial\psi}{\partial s})=0 \tag{4.30}$$

Thus, the complete description of beam behavior is given by Equations (4.30) and (4.25), rearranged here, where $(.)_{,z} = \frac{\partial(.)}{\partial z}$:

$$\psi_{,t} = \frac{1}{C_N}\left(-EI\psi_{,ssss} + af_{,ss} + T_{,s}\psi_{,s} + T\psi_{,ss}\right) + \frac{1}{C_T}\left(EI\left(\psi_{,s}\right)^2\psi_{,ss} - af\left(\psi_{,s}\right)^2 + T_{,s}\psi_{,s}\right) \tag{4.31}$$

$$T_{,ss} - (af - EI\psi_{,ss})\psi_{,ss} - \left(af_{,s} - EI\psi_{,sss}\right)\psi_{,s} - \frac{C_T}{C_N}\left(af_{,s} - EI\psi_{,sss} + T\psi_{,s}\right)\psi_{,s} = 0 \tag{4.32}$$

Equations (4.31) and (4.32) match both the original derivations by Hines and Blum [78] and a more recent examination by Hilfinger [77] and condense the general system of Equations (4.23), (4.29), and (4.24).

4.3 Discussion

In summary, a model of the flagellum as a nonlinear slender beam in viscous media can be derived from first principles. Equations (4.23), (4.24), and (4.29) present a system of equations with 3 dependent variables: the tension in the beam $T(s,t)$, the shear angle $\psi(s,t)$, and the total internal shear force term $f(s,t)$. In order to solve these equations, a relationship between total internal shear force (including both passive and active elements) and beam motion is needed. This relationship defines the regulation of dynein that produces inter-doublet sliding and consequent bending of the flagellum.

A brief examination of Equations (4.31) and (4.32) reveals significant nonlinearity in beam motion, even for a simplified 2D model of the axoneme. Beating flagella reflect this aspect of the model when amplitudes are finite; a consequence is that, in general, solutions are not straightforward. We examine closed-form solutions through eigenanalysis of linearized equations of motion to determine modes of oscillation, particularly unstable modes which correspond to spontaneous oscillation. In addition, we consider the full nonlinear system and simulate solutions using a time-marching approach. These methods and their results are described in the following two chapters.

Chapter 5

Unstable Modes in a Model of Sliding-Controlled Dynein Activity[1]

Dynein acts to slide adjacent microtubule doublets relative to one another. This motion, coupled with elastic constraints within the axoneme, drives the generation of bends and subsequent movement of the flagellum. One of the first mathematical models of flagellar activity proposed this sliding activity itself as the feedback mechanism for dynein regulation. A more recent formulation of this concept [75] shows an ability to match observed experimental data, but does not consider all possible solutions. This prior study identified a propulsive, periodic solution of the linearized version of the sliding-controlled model, which closely resembles observed behavior. However, unstable, non-propulsive solutions exist at the same parameter values. The stability of identified modes is important for understanding their physical relevance.

5.1 Introduction and Motivation

The sliding of filaments (microtubule doublets) within the axoneme was discovered in 1965 through analysis of micrographs produced by Satir [103]. Considering these micrographs, Charles Brokaw proposed a theory of bend propagation controlled by sliding between filaments [2], later expanded to include curvature-controlled feedback. Another model of dynein regulation was recently proposed by Riedel-Kruse et al in which dynein activity depends only on sliding

---

[1] Analysis of unstable modes of the SC model presented in this chapter was published as part of an article in the *Journal of the Royal Society Interface* [123]. KW contributed to equation derivations including closed-form eigenvalue analysis and Matlab modeling, along with discussion of stability of both cases.

between doublets on opposite sides of the flagellum [75]. The derived 'sliding-controlled' (SC) model results in periodic oscillations under certain conditions, however the analysis is incomplete without examination of the possibility of co-existing unstable modes. This chapter recapitulates the analysis of the sliding-controlled model of Riedel-Kruse in a more general form to allow identification of both stable and unstable modes. It is found that unstable modes exist at the same parameter values that correspond to periodic solutions found by the authors of the previous study; thus the periodic modes are not of physical importance.

5.2 Linearized Equation of Motion and Shear Force

In order to understand flagellar oscillations, Riedel-Kruse et-al linearized the set of equations of motion derived in Chapter 4 [75]. After eliminating all higher-order terms from Equations (4.31) and (4.32) (those that include more than one dependent variable T, f, or ψ), a single linear equation remains (where $(.)_{,z} = \frac{\partial(.)}{\partial z}$):

$$EI\psi_{,ssss} - af_{,ss} + C_N\psi_{,t} = 0 \tag{5.1}$$

Examining this equation shows the tangent angle of the flagellum, ψ, is dependent on a viscous term $C_N \frac{\partial\psi}{\partial t}$, the flexural rigidity of the microtubule doublet structure $EI\psi_{,ssss}$, and the total internal shear $af_{,ss}$.

Riedel-Kruse et al propose an internal shear force term $f(s,t)$ that depends on the relative doublet displacement $\Delta(s,t)$ and on relative sliding velocity of doublets on opposite sides of the beam, $\frac{\partial\Delta(s,t)}{\partial t}$ (a schematic of the relative doublet displacement Δ is shown in Figure 5.1) [75].

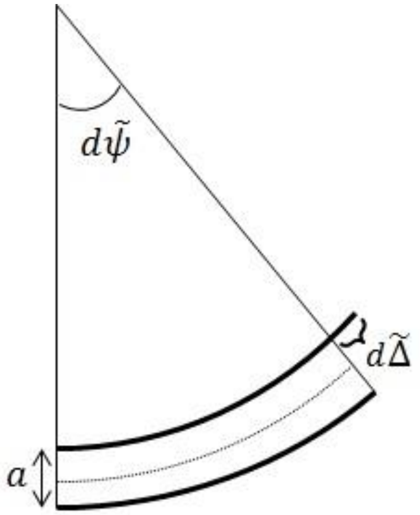

Figure 5.1 – Schematic of sliding displacement
Diagram showing relationship between tangent angle ψ and relative displacement of doublets Δ for a beam with diameter a (a more detailed beam representation can be found in Figure 4.1).

The sliding-controlled equation for active internal shear force f is defined in (5.2). Shear increases with $\delta p(s,t)$, the incremental change in probability of dynein attachment, and decreases with sliding velocity (note active force is assumed negative here):

$$f(s,t) = -2\rho\bar{f}\delta p + 2\rho\bar{p}f'\frac{\partial \Delta}{\partial t} \tag{5.2}$$

Where ρ is the linear density of dynein arms; $\bar{f}$ is the maximum force per dynein arm, $\bar{p}$ is the mean baseline probability of dynein head attachment, and f' is the magnitude of the slope of the dynein force-velocity curve. Because the force per dynein head decreases with velocity ($f'$is negative), dynein cross-linking probability changes in response to sliding speed, as described by the equation:

$$\frac{\partial(\delta p)}{\partial t} = \frac{1}{\tau}\left(\frac{\bar{p}(1-\bar{p})f'}{f_c}\frac{\partial \Delta}{\partial t} - \delta p\right) \tag{5.3}$$

Where τ is the characteristic time for this effect, and f_c is a characteristic force for crosslink detachment. This relationship can lead to an increase in net shear force in response to increasing sliding velocity and displacement, which is mathematically equivalent to negative friction or negative stiffness. While counterintuitive, this response is biologically reasonable considering the active force contributions of dynein along the length of the flagellum.

5.3 Eigenvalue Problem

Riedel-Kruse et al propose a form of solution to Equation (5.1) by hypothesizing ψ is separable: $\psi(s,t) = A(s)B(t)$ [75]. This allows examination of mode shapes $A(s)$ for a prescribed time response $B(t)$. Riedel-Kruse proposed a purely periodic time function $B(t) = e^{ni\omega t}$ which permits identification of only periodic modes at frequencies $n\omega$. However, more generally $B(t)$ can take many different forms, including solutions that increase with time. To allow identification of both stable and unstable modes, we generalize the assumed time function as $B(t) = e^{\sigma_n t}$ where $\sigma_n = \alpha_n + i\omega_n$(both α_n and ω_n are real). The assumed form of the resulting waveform becomes:

$$\psi(s,t) = \sum_{n=-\infty}^{\infty} A_n \tilde{\psi}^{(n)}(s) e^{\sigma_n t} \tag{5.4}$$

Since we propose solutions to the linearized equation, each mode $\tilde{\psi}^{(n)}$ is a solution along with any linear combination of modes. While the complete description of the beam shape ψ may require many modes n, we consider just one Fourier mode ($n = 1$) following the method of Riedel-Kruse [75], and drop the subscript:

$$\psi(s,t) = \tilde{\psi}(s) \exp(\sigma t) \tag{5.5}$$

Similarly, the other dependent variables f, Δ, and δp become:

$$f(s,t) = \tilde{f}(s) \exp(\sigma t) \tag{5.6}$$

$$\Delta(s,t) = \widetilde{\Delta}(s)\exp(\sigma t) \tag{5.7}$$

$$\delta p(s,t) = \delta\tilde{p}(s)\exp(\sigma t) \tag{5.8}$$

By assigning a form to the time-dependent characteristics of the beam angle, the time-dependent viscous term in Equation (5.1) can be calculated and the overall governing equation becomes:

$$EI\frac{d^4\tilde{\psi}}{ds^4} - a\frac{d^2\tilde{f}}{ds^2} + \sigma C_N\tilde{\psi} = 0 \tag{5.9}$$

The shear force shape function $\tilde{f}(s)$ can be expressed in terms of a complex mechanical impedance term $\chi(\sigma)$:

$$\tilde{f}(s) = \chi(\sigma)\tilde{\Delta}(s) \tag{5.10}$$

The inter-doublet separation shape function $\widetilde{\Delta}(s)$ is defined as shown in Figure 5.1, formalized in equation form below, where $\widetilde{\Delta}_0 = \widetilde{\Delta}(0)$:

$$\tilde{\Delta}(s) = \tilde{\Delta}_0 + a\big(\tilde{\psi}(s) - \tilde{\psi}(0)\big) \tag{5.11}$$

The complex impedance $\chi(\sigma)$ is defined in terms of dynein kinetics by comparison to Equation (5.2). Substituting the assumed solutions of displacement $\tilde{\Delta}(s)$ and probability of dynein attachment $\delta\tilde{p}(s)$ (Equations (5.7) and (5.8)) into the equation governing cross-linking probability (5.3):

$$\delta\tilde{p}(s) = \frac{\bar{p}(1-\bar{p})f'}{f_c}\frac{\sigma}{1+\sigma\tau}\tilde{\Delta}(s) \tag{5.12}$$

The expressions for $\delta\tilde{p}$ and $\tilde{\Delta}(s)$ are then substituted into the equation for shear force (5.2):

$$\tilde{f}(s) = -2\rho\bar{f}\left[\frac{\bar{p}(1-\bar{p})f'}{f_c}\frac{\sigma}{1+\sigma\tau}\tilde{\Delta}(s)\right] + 2\rho\bar{p}f'\sigma\tilde{\Delta}(s) \tag{5.13}$$

The complex impedance, $\chi(\sigma)$ can now written compactly in terms of the characteristic exponent, σ:

$$\chi(\sigma) = \frac{-A\sigma}{1+\sigma\tau} + B\sigma \tag{5.14}$$

$$A = \frac{2\rho\bar{p}(1-\bar{p})\bar{f}f'}{f_c} \tag{5.15}$$

$$B = 2\rho\bar{p}f' \tag{5.16}$$

Where the derived parameters A and B are real. For the special case of the neutrally-stable, periodic response the characteristic exponent $\sigma = i\omega$, and $\chi(i\omega) = k + i\omega\lambda$ [75], [77]. The effects of the feedback-controlled dynein motors can be combined into dynamic stiffness (k) and friction (λ) coefficients:

$$k = -A\omega^2\tau/(1+\omega^2\tau^2) \tag{5.17}$$

$$\lambda = (B-A)/(1+\omega^2\tau^2) \tag{5.18}$$

Passive stiffness and friction may also be included, but here these contributions are considered negligible [75]. The values of k and λ are expected to both be negative, corresponding to an increase in net shear force in response to increasing doublet sliding rate.

Substitution of identities (5.5) - (5.8), (5.10), and (5.11) into the linearized equation of motion (5.1) leads to an equation of motion dependent only on constants EI, a, c_N ,and complex impedance $\chi(\sigma)$:

$$EI\frac{d^4\tilde{\psi}}{ds^4} - a^2\chi\frac{d^2\tilde{\psi}}{ds^2} + \sigma c_N\tilde{\psi} = 0 \tag{5.19}$$

This equation can be translated to non-dimensional form using the parameters:

$$\bar{s} = s/L \tag{5.20}$$

$$\bar{\sigma} = \sigma c_N L^4/EI \tag{5.21}$$

$$\bar{\chi} = \chi a^2 L^2 / EI \tag{5.22}$$

So that Equation (5.19) becomes:

$$\tilde{\psi}'''' - \bar{\chi}\tilde{\psi}'' + \bar{\sigma}\tilde{\psi} = 0 \tag{5.23}$$

Where $(\cdot)' = \frac{d(\cdot)}{d\bar{s}}$.

Boundary conditions of the beam are necessary to identify solutions of $\tilde{\psi}(s)$ which satisfy Equation (5.23). Because the base of the flagellum is fixed at the cell body, we assume cantilever beam conditions with a fixed base and free end. At the base, the beam can support forces and moments but has a zero tangent angle and zero angular time derivative. At the distal end of the beam there can be no residual forces or moments supported. These constraints can be stated mathematically (following substitution into Equation (5.1)):

(i) Zero angle at base: $\psi(0,t) = 0$

(ii) Zero normal velocity at base: $EI\psi_{,sss}(0,t) - af_{,s}(0,t) = 0$

(iii) Zero moment at distal end: $EI\psi_{,s}(L,t) = 0$

(iv) Zero transverse force at distal end: $EI\psi_{,ss}(L,t) - af(L,t) = 0$

(5.24)

Using the identities of Equations (5.20) to (5.23), the nondimensional fixed-free nondimensional boundary conditions are:

(i) Zero angle at base: $\tilde{\psi}(0) = 0$

(ii) Zero normal velocity at base: $\tilde{\psi}'''(0) - \bar{\chi}\tilde{\psi}'(0) = 0$

(iii) Zero moment at distal end: $\tilde{\psi}'(1) = 0$

(iv) Zero transverse force at distal end: $\tilde{\psi}''(1) - \bar{\chi}\left(\bar{\Delta}_0 + \tilde{\psi}(1) - \tilde{\psi}(0)\right) = 0$

(5.25)

Where $\bar{\Delta}_0 = \tilde{\Delta}_0/a$ describes the nondimensional inter-doublet sliding at the base [75]. We examined both the situations where basal sliding is real and dependent on separate stiffness parameters (Case 1) as well as the case where no basal sliding is permitted (Case 2) [75], [77]:

Case 1: Sliding at the proximal end is resisted by base stiffness, k_s , and friction, γ_s:

$$\Gamma = \frac{\bar{\chi}}{\bar{\chi} + \bar{k}_s + \bar{\sigma}\bar{\gamma}_s} \tag{5.26}$$

$$\bar{k}_s = \frac{k_s a^2 L}{EI} \tag{5.27}$$

$$\bar{\gamma}_s = \gamma_s a^2/(L^3 c_N) \tag{5.28}$$

leading to the expression:

$$\bar{\Delta}_0 = \Gamma \left(\tilde{\psi}(0) - \int_0^1 \tilde{\psi}(\bar{s}) d\bar{s} \right) \tag{5.29}$$

Case 2: Sliding at the proximal end of the flagellum is prohibited: $\bar{\Delta}_0 = 0$.

It is important to note that even in Case 1 where relative sliding of the doublets at the base is permitted, the boundary conditions of (5.25) still apply (zero angle and zero normal velocity at the base $\bar{s} = 0$).

5.4 Solution to the Eigenvalue Problem

Solutions to the differential equation for the mode shape, Equation (5.23), are assumed to be of the form:

$$\tilde{\psi}(\bar{s}) = A\, e^{\beta \bar{s}} \tag{5.30}$$

Substitution of Equation (5.30) into Equation (5.23) gives the characteristic polynomial:

$$\beta^4 - \bar{\chi}\beta^2 + \bar{\sigma} = 0 \tag{5.31}$$

The roots of Equation (5.31) are values of the characteristic (space) exponent, $\beta_1,\ \beta_2,\ \beta_3,\ \beta_4$. For a given value of $\bar{\chi}$, the general solution to Equation (5.23) can be constructed using β_{1-4} from Equation (5.31):

$$\tilde{\psi}(\bar{s}) = A_1 e^{\beta_1 \bar{s}} + A_2 e^{\beta_2 \bar{s}} + A_3 e^{\beta_3 \bar{s}} + A_4 e^{\beta_4 \bar{s}} \tag{5.32}$$

Substituting this general solution (5.32) into boundary condition Equations (5.25) leads to a matrix equation of the form given in Equation (5.33), below, with 4 unknowns (A_n) for each value of the characteristic exponent β_n (roots of equation (5.31)). Equations (5.26) to (5.29) can be used to eliminate $\overline{\Delta}_0$ from boundary condition Equation (5.25)(iv):

$$\begin{bmatrix} \cdots & 1 & \cdots \\ \cdots & \beta_n^3 - \bar{\chi}\beta_n & \cdots \\ \cdots & \beta_n e^{\beta_n} & \cdots \\ \cdots & \beta_n^2 e^{\beta_n} + \bar{\chi}\left(1 - \Gamma - e^{\beta_n} + \dfrac{\Gamma}{\beta_n}\left(e^{\beta_n} - 1\right)\right) & \cdots \end{bmatrix} \begin{Bmatrix} A_1 \\ A_2 \\ A_3 \\ A_4 \end{Bmatrix} = \begin{Bmatrix} 0 \\ 0 \\ 0 \\ 0 \end{Bmatrix}, \quad \text{n=1, 2, 3, 4} \tag{5.33}$$

If sliding at the base is not permitted (Case 2), the base compliance parameter $\Gamma = 0$ and the matrix becomes:

$$\begin{bmatrix} \cdots & 1 & \cdots \\ \cdots & \beta_n^3 - \bar{\chi}\beta_n & \cdots \\ \cdots & \beta_n e^{\beta_n} & \cdots \\ \cdots & \beta_n^2 e^{\beta_n} + \bar{\chi}\left(1 - e^{\beta_n}\right) & \cdots \end{bmatrix} \begin{Bmatrix} A_1 \\ A_2 \\ A_3 \\ A_4 \end{Bmatrix} = \begin{Bmatrix} 0 \\ 0 \\ 0 \\ 0 \end{Bmatrix}, \quad \text{n=1, 2, 3, 4} \tag{5.34}$$

Note that the values of β_n in the matrices above depend not only on the physical parameters of the model, but also on the characteristic exponent, or eigenvalue, $\bar{\sigma}$ via $\bar{\chi}(\bar{\sigma})$. For a specific parameter set, the eigenvalue problem can thus be written compactly as:

$$\mathbf{M}(\bar{\sigma}) \cdot \boldsymbol{a} = \mathbf{0} \qquad\qquad \boldsymbol{a} = [A_1, A_2, A_3, A_4]^T \tag{5.35}$$

Non-trivial solutions are found by seeking values of $\bar{\sigma}$ that lead to:

$$D(\bar{\sigma}) = \det \mathbf{M}(\bar{\sigma}) = 0 \tag{5.36}$$

Eigenvalues $\bar{\sigma}_m$ are found at the zeros of $D(\bar{\sigma})$ (or minima of $|D(\bar{\sigma})|$). Mode shapes are found by seeking vectors $\boldsymbol{a}^{(m)}$ that span the corresponding null-space of the matrix, $\mathbf{M}(\bar{\sigma}_m)$; this is accomplished by singular value decomposition. The mode shape $\tilde{\psi}^{(m)}(\bar{s})$ is then reconstructed by substituting values for $A_n^{(m)}$ and $\beta_n^{(m)}$ (coefficients and roots corresponding to the eigenvalue $\bar{\sigma}_m$) into Equation (5.32).

5.5 Results and Stability

5.5.1 Case 1: Finite Sliding Compliance at the Base

Modes from eigenvalue analysis

A sliding-controlled model with fixed-free boundary conditions and sliding permitted at the base was analyzed by the direct solution approach described above[75], [77]. Sliding at the base was opposed by finite positive stiffness ($k_s = 94.8 \times 10^{-3}$ N/m) and friction ($\gamma_s = 0.273 \times 10^{-3}$ N-s/m) as in [75]. Other parameters were chosen to match the mechanical impedance used by [75]; all parameters are listed in Table 5.1. These parameters lead to negative effective shear stiffness ($k = -1620$ N/m^2) and friction ($\lambda = -7.60$ N-s/m^2) in the flagellum for the 20.6 Hz mode discussed by Riedel-Kruse [75].

Table 5.1 – Parameter values for sliding-controlled model with base sliding (Case 1) [75]

Parameter	**Value**	**Units**	**Description**
c_N	0.0034	pN-s/μm^2	Normal resistive force coefficient
c_T	0.0017	pN-s/μm^2	Tangent resistive force coefficient $(c_T \approx c_N/2)$
a	0.185	μm	Effective diameter of flagellum
L	58.3	μm	Length of flagellum
EI	1700	pN-μm^2	Flexural rigidity of flagellum
τ	0.004	s	Dynein time constant
$\bar{p}$	0.03	1	Mean probability of crosslinking
$\bar{f}$	3.8	pN	Dynein stall force
f_C	2.0	pN	Characteristic force
f'	1.8	pN-s/μm	Slope of dynein force-velocity curve
k_s	94.8×10^{-3}	pN/μm	Sliding stiffness at base
γ_s	0.273×10^{-3}	pN-s/μm	Sliding friction at base
ρ	150	1/μm	Density of dynein motors
k_3	800	pN/μm^4	Nonlinear shear stiffness

Characteristic exponents in the complex plane are found at local minima of the determinant magnitude, $|D(\sigma)|$, shown in Figure 5.2 (a) - (b) (results are shown in terms of physical, rather than dimensionless, variables). Two important observations can be made. (i) A periodic solution (complex conjugate eigenfunctions with purely imaginary characteristic exponents: $\sigma = i\omega$) exists. The frequency of this periodic mode corresponds precisely to the frequency ($\omega/2\pi$=20.6 Hz) of the periodic mode reported by Reidel-Kruse et al in 2007 for these parameters [75]. (ii) Multiple unstable modes co-exist with this periodic mode over the range of σ examined here. Three of these unstable modes have characteristic exponents with positive real parts ($\mathrm{Re}(\sigma) = \alpha > 0$).

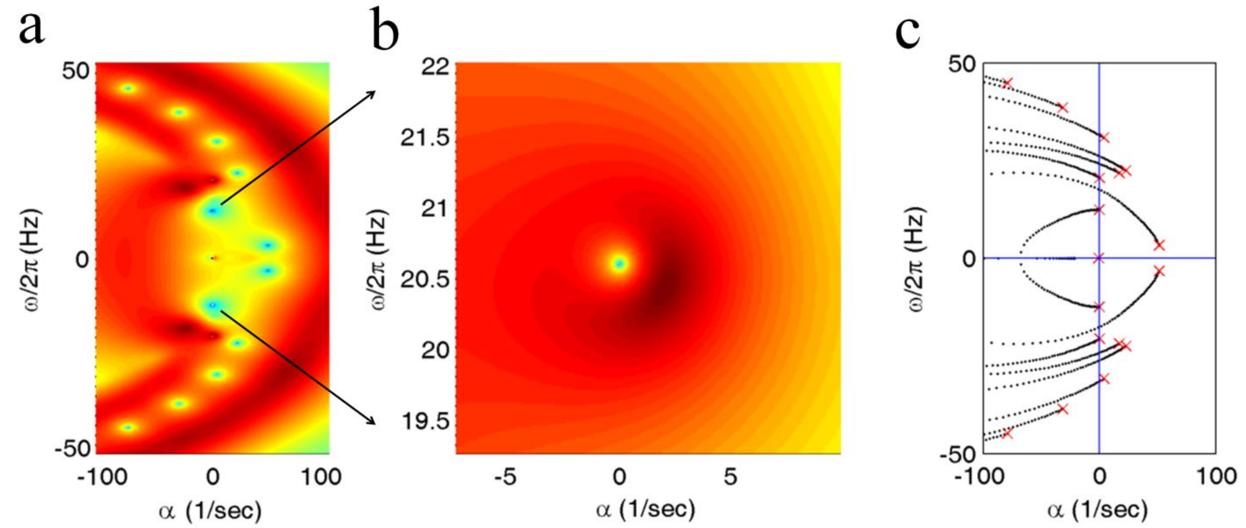

Figure 5.2 – Eigenvalues from direct solution of the sliding-controlled flagella model (a) Images of the log magnitude of the determinant, ln $|D(\sigma)|$ (arbitrary units), are shown as a function of $\sigma = \alpha + i\omega$ (Case 1; parameters in Table 5.1). Eigenvalues (characteristic exponents) are found at local minima (blue) of $|D(\sigma)|$. Unstable modes have $\alpha = Re(\sigma) > 0$. (b) Expanded view of panel (a) showing the eigenvalue at $\sigma = i2\pi \cdot 20.6$ corresponding to a 20.6 Hz periodic mode. (c) Eigenvalues were also calculated from the weighted-residuals method [105]: Paths of eigenvalues $\sigma = \alpha + i\omega$ are shown in the complex plane as $\bar{p}$ is varied ($0 < \bar{p} < 0.04$). Other parameters are as in Table 5.1. The red 'x' symbols denote the eigenvalues at the final value $\bar{p} = 0.04$. The eigenvalues in panel (c) closely match the minima of $|D(\sigma)|$ in panel (a).

Mode shapes corresponding to the eigenvalues of Figure 5.2 are shown in Figure 5.3. The shape of the periodic mode at 20.6 Hz obtained here matches closely the shape of the periodic mode at the same frequency in [75]. The unstable modes of this model under the same conditions have not been described in prior studies.

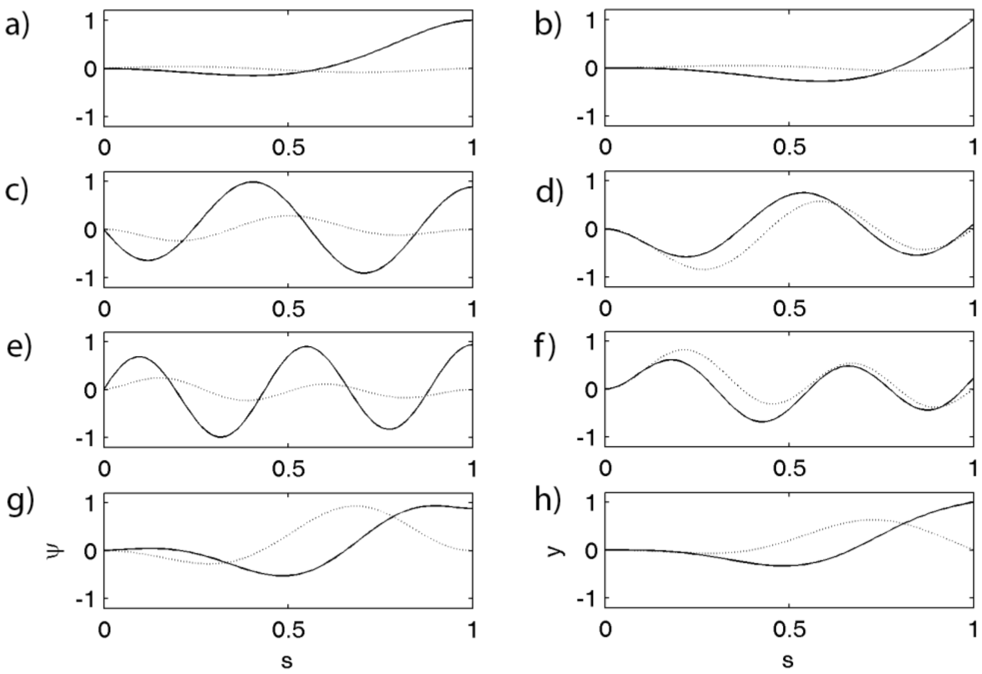

Figure 5.3 – Unstable and neutrally-stable modes of the sliding-controlled model with sliding at the base (Case 1).

(Left) The mode shape expressed in terms of tangent angle, $\tilde{\psi}(\bar{s})$. (Right) The mode shape expressed in terms of displacement $\tilde{y}(\bar{s})$. The real (solid) and imaginary (dashed) part of each mode is shown. Each mode corresponds to eigenvalue $\sigma = \alpha + i\omega$: (a-b) $\alpha = 51.3$/s, $\omega/2\pi$ =3.3 Hz (unstable); (c-d) $\alpha = 22.8$/s, $\omega/2\pi$ =22.5 Hz (unstable); (e-f) $\alpha = 4.0$/s, $\omega/2\pi$ =30.8 Hz (unstable); (g-h) $\alpha = 0.0$/s, $\omega/2\pi$ =20.6Hz (periodic).

Unstable modes were investigated to determine frequency of oscillation and bend propagation direction. Figure 5.4(a) shows the frequency of the least stable unstable mode, as a function of the mean crosslinking probability, $\bar{p}$, and flagellum length, L. The white region of the plot indicates parameter combinations for which unstable modes are absent, so the edge of the colored region indicates the stability boundary. Figure 5.4(b) displays the gradient of phase for the least stable mode, $\frac{\partial \angle \tilde{\psi}}{\partial s}$, at each parameter combination. If the mode exhibits proximal-to-distal (anterograde) propagation, the phase gradient will be negative. For example, the phase gradient of the 20.6 Hz mode is negative. However, the phase gradient of the least stable mode is positive for all parameter combinations in this model, indicating that retrograde (distal-to-proximal) propagation is present in this model with these parameters.

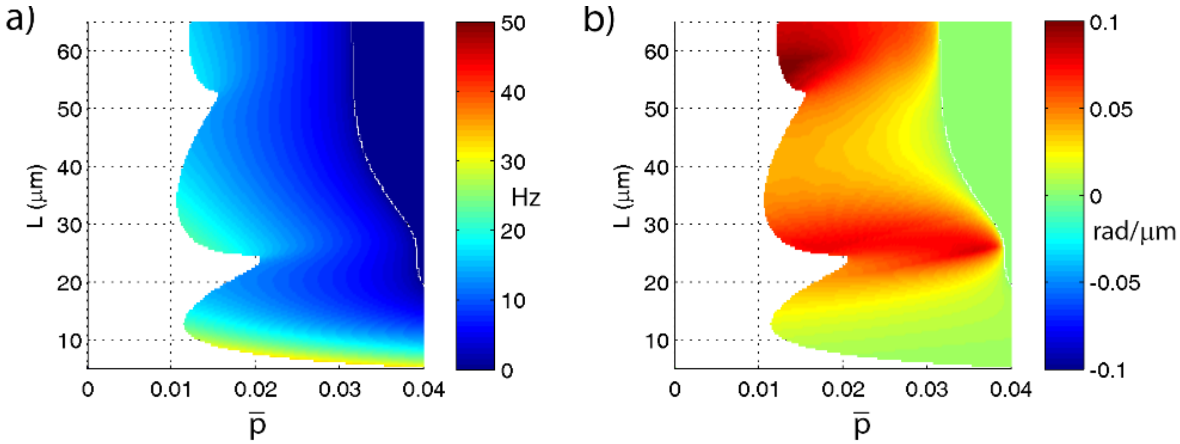

Figure 5.4 – Frequency of least stable mode and bend propagation direction, sliding-controlled model (Case 1)
(a) Frequency $\omega/2\pi$ (Hz) of the least stable mode of the sliding-controlled flagella model (Case 1) as a function of flagella length, L, and mean probability of crosslinking, $\bar{p}$. Other parameters are as in Table 5.1. At each parameter combination $(\bar{p}, L)$ frequency is obtained from the imaginary part of the eigenvalue $\sigma = \alpha + i\omega$ with largest real part (α). (b) Median phase gradient, $\frac{\partial \angle \tilde{\psi}}{\partial s}$, of the least stable mode. Anterograde (proximal-distal) propagation corresponds to a phase gradient < 0, for $\omega > 0$. For all parameter combinations shown here, the least stable mode exhibits phase gradient > 0 and thus retrograde propagation.

Predicted behavior from simulation

Numerical time-marching simulation allows exploration of nonlinear, transient and non-periodic behavior. Simulations of the full nonlinear system of flagellum equations were performed in the time domain with fixed-free boundary conditions to investigate the behavior of the sliding-controlled dynein regulation model at finite amplitudes. Equations (4.23), (4.24), and (4.29) were modeled in a commercial finite element (FE) software package (COMSOL v4.3a, COMSOL, Inc., Burlington, MA) with values given in Table 5.1.

Linearized models of the flagellum either omit elastic shear forces [75]or permit elastic force to remain proportional to displacement. In the real system, it is likely that forces from passive components of the axoneme will increase nonlinearly with displacement [77]. Such nonlinearity does not affect the linear models above, but prevents unstable modes from growing without limit. Accordingly, in nonlinear simulations an additional restoring shear force proportional to the cube of the shear displacement was added. The simulated shear force becomes:

$$f_{sim}(s,t) = f(s,t) + k_3\Delta^3 \tag{5.37}$$

The nonlinear restoring force of Equation (5.37) approximates the assumed stiffening behavior of elastic elements [77], [106]. When the linearized model is unstable, the value of k_3 may determine the amplitude of simulated oscillations. In simulations, the value of the nonlinear coefficient k_3 was adjusted to produce oscillations of comparable amplitude in each model. Simulations of the sliding-controlled model with sliding at the base (Case 1) lead to oscillatory waves with retrograde propagation (Figure 5.5). The positive mean value of tension at the base (T_0) and counter-clockwise loop of Figure 5.5(b-c) signify backward propulsive force (anterograde bend propagation).

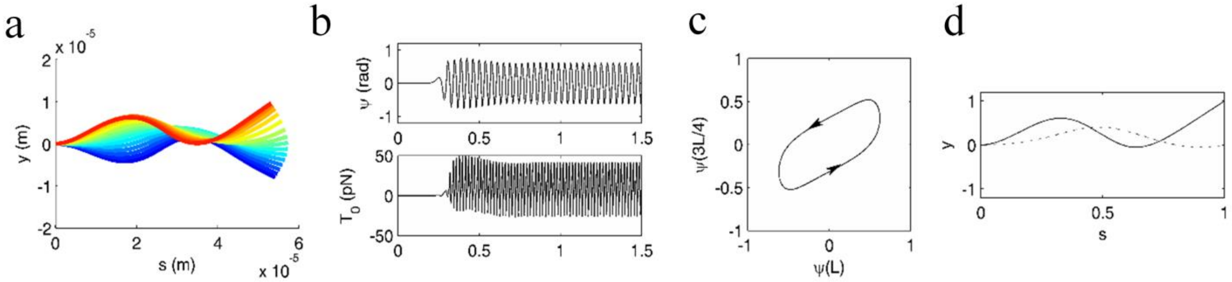

Figure 5.5 – Nonlinear simulation of sliding-controlled model with sliding at base (Case 1) (a) Successive snapshots of the flagellar waveform from time-marching simulations; color shows time increasing from blue (early) to red (later); (b) Time series of angle at tip $\psi(s = L)$ (top) and tension at base $T_0(s = 0)$ (bottom; $T_0 < 0$ is propulsive); (c) Plot of $\psi(3L/4)$ vs $\psi(L)$ (clockwise loop = anterograde propagation; counter-clockwise=retrograde); (d) Fundamental mode shape $y(s)$ from Fourier analysis of simulation.

5.5.2 Case 2: No sliding at the base

Modes from eigenvalue analysis

This case provides an opportunity for more extensive comparison to results from prior work [77], shown in Figure 5.6. Periodic modes were found by the direct solution method at frequencies from 1-100 Hz, using the same parameter values as in [77], given in Table 5.2.

Table 5.2 – Parameter values for sliding-controlled model with no base sliding (Case 2) [75], [77] (, EI, a, c_N are as in Table 5.1).

Parameter	**Value**	**Units**	**Description**
$\bar{p}$	0.01	1	Mean probability of crosslinking
$\bar{f}$	5.2	pN	Dynein stall force
f_C	1.0	pN	Characteristic force
f'	0.5	pN-s/μm	Slope of dynein force-velocity curve
k_3	40	pN/μm^4	Nonlinear shear stiffness

Figure 5.6 shows the frequencies of all unstable modes found by the method of weighted residuals, at all values of the complex impedance, χ. The frequency predictions from the weighted residual method at the boundaries of different solution regimes agree closely with the frequencies of periodic modes obtained by direct solution. These predictions also match corresponding results in [77]. The values of the complex impedance χ corresponding to periodic solutions are shown in Figure 5.6 (red markers); the frequency of each mode is plotted on the vertical axis of Figure 5.6(b). Figure 5.6(a) is directly comparable to Fig. 3 in [77]. For many of the parameter combinations at which periodic solutions exist, co-existing unstable modes are also found.

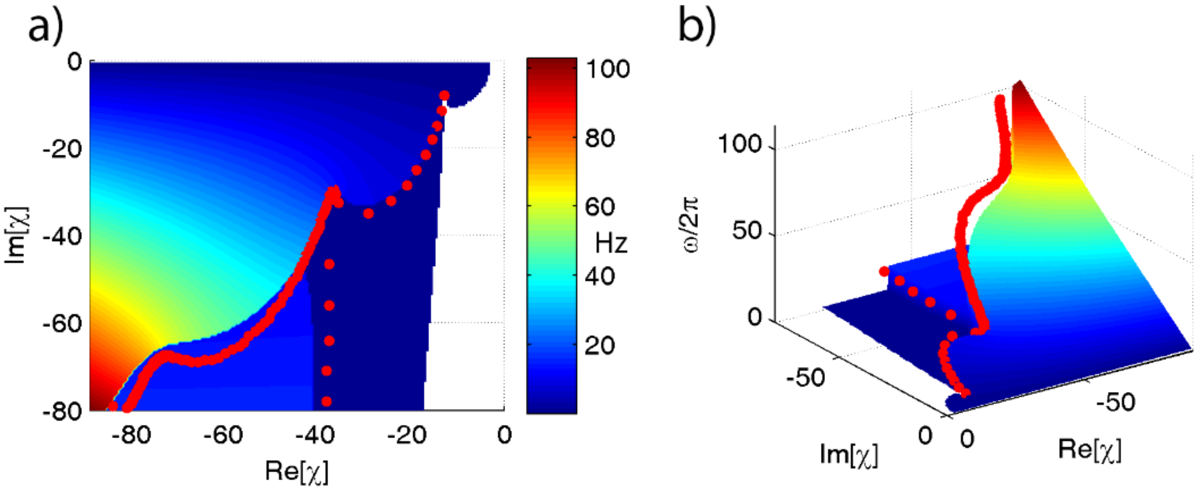

Figure 5.6 – Comparison of frequency of periodic solutions from direct analysis and weighted residual predictions, no base sliding (Case 2).
(a) Frequency, $\omega/2\pi$ (Hz), shown as a function of the mechanical impedance, χ. The color scale in panels (a) and (b), and the vertical axis in panel (b) display the frequency of the least stable mode. Modes with zero frequency (white) are non-oscillatory. The plots show good agreement and periodic (neutrally-stable) solutions arise at transitions between solution regimes (described in [77]).

Similar to Case 1, eigenvalues were computed using the method of weighted residuals for the sliding-controlled model (Equation (5.23)) with no sliding at the base (Case 2, other parameters are as in Table 5.2). Figure 5.7(a) shows the locations of eigenvalues for a range of parameters $\sigma = \alpha + i\omega$. The frequency and propagation direction of the least stable mode are shown in Figure 5.7(b)-(c) as functions of the length of the flagellum L and mean probability of attachment $\bar{p}$. The neutrally stable mode at 28Hz, identified by eigenvalues on the imaginary axis in Figure 5.7(a) and by the mode shape in Figure 5.8, matches the corresponding example result from [77].

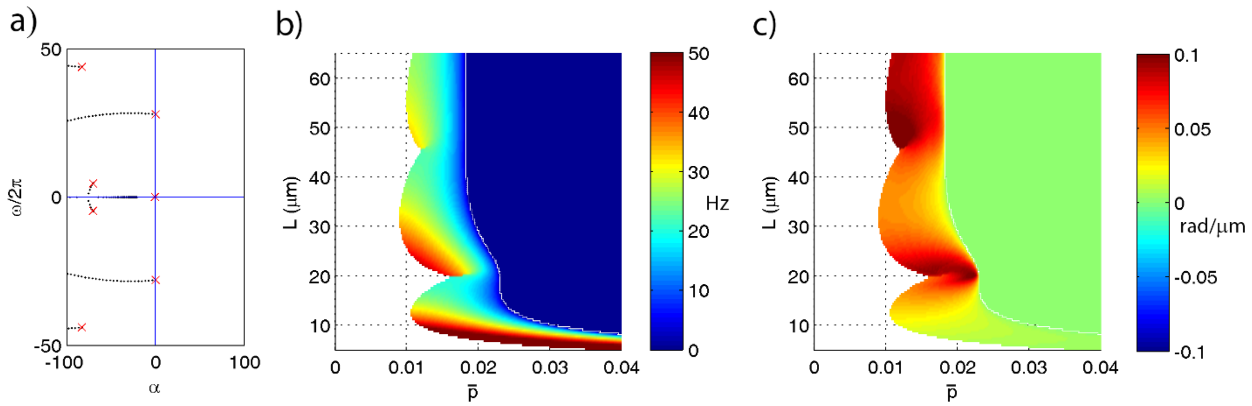

Figure 5.7 – Eigenvalues of the sliding-controlled model with no base sliding (Case 2) from the weighted residuals method
(a) Paths of eigenvalues $\sigma = \alpha + i\omega$ in the complex plane as baseline probability of dynein attachment, $\bar{p}$, is varied ($0 < \bar{p} < 0.01$) in the sliding-controlled flagella model with no sliding at the base (Case 2). Other parameters are as in Table 5.2. The red 'x' symbols denote the eigenvalues at the final value: $\bar{p} = 0.01$. (b) Frequency $\omega/2\pi$ (Hz) of the least stable mode of this model as a function of flagella length and $\bar{p}$. Other parameters are as in Table 5.2. At each parameter combination $(\bar{p}, L)$ frequency is obtained from the imaginary part $(i\omega)$ of the eigenvalue $\sigma = \alpha + i\omega$ with largest real part (α). (c) Median phase gradient, $\frac{\partial \angle \tilde{\psi}}{\partial s}$, of the least stable mode. Anterograde (proximal-distal) propagation corresponds to a phase gradient < 0, for $\omega > 0$. For all parameter combinations shown here, the least stable mode exhibits phase gradient > 0 and thus retrograde propagation.

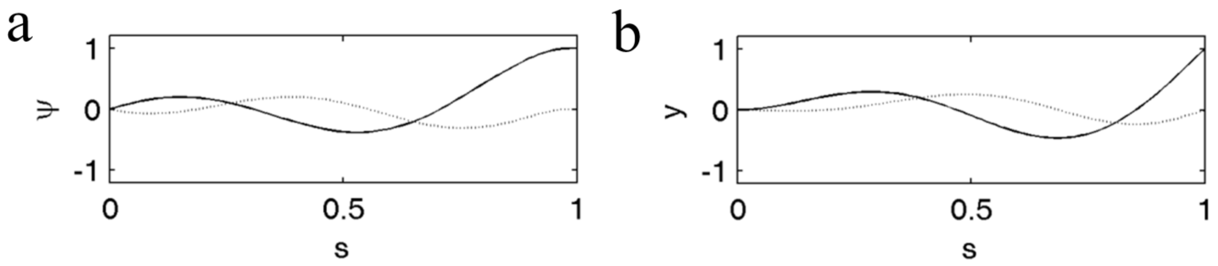

Figure 5.8 – Mode shapes of the sliding-controlled model with no sliding at base (Case 2). The neutrally-stable, retrograde propagating mode corresponding to eigenvalue $\sigma = \alpha + i\omega$: $\alpha = 0.0$/s, $\omega/2\pi$ =28 Hz, as described in [77]. (a) The mode shape expressed in terms of tangent angle, $\tilde{\psi}(\bar{s})$. (b) The mode shape expressed in terms of displacement $\tilde{y}(\bar{s})$. The real (solid) and imaginary (dashed) part of each mode is shown

Predicted behavior from simulation

Modes of oscillation for Case 2 were also obtained from COMSOL simulations using parameters given by Table 5.2, including a nonlinear shear restoring force. The sliding-controlled model without sliding at the base (Case 2) exhibits non-propulsive, retrograde waves similar to the least stable mode of the linearized version (Figure 5.9).

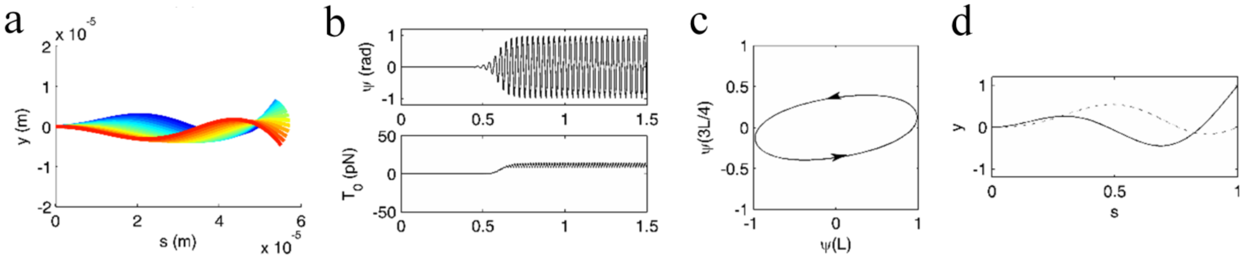

Figure 5.9 – Nonlinear simulation of sliding-controlled model with no sliding at base (Case 2) (a) Successive snapshots of the flagellar waveform from time-marching simulations; color shows time increasing from blue (early) to red (later); (b) Time series of angle at tip $\psi(s = L)$ (top) and tension at base $T_0(s = 0)$ (bottom; $T_0 < 0$ is propulsive); (c) Plot of $\psi(3L/4)$ vs $\psi(L)$ (clockwise loop = anterograde propagation; counter-clockwise=retrograde); (d) Fundamental mode shape y from Fourier analysis of simulation.

Fourier analysis of the steady-state spatiotemporal pattern of $\psi(s,t)$ from simulation was performed along the time dimension (*fft* ; Matlab$^{\text{TM}}$, The Mathworks, Natick, MA) to obtain the frequency and shape of the fundamental mode of oscillation (Figure 5.5, Figure 5.9, Table 5.3). The relative contribution of the fundamental mode to the simulated response was measured by the ratio of its magnitude to the summed magnitudes of all the Fourier coefficients (Table 5.3). The similarity of the fundamental mode from simulation to the unstable modes of the linearized model (obtained by weighted residuals eigenanalysis) was measured by the amplitude of the correlation coefficient between the two shapes (*corrcoef* ; Matlab$^{\text{TM}}$, The Mathworks, Natick, MA; Table 5.3).

Table 5.3 – Comparison of SC fundamental modes from simulation and direct eigenanalysis Underlined values correspond to the least stable mode.

Model	**Simulation: Fundamental Frequency (Hz)**	**Simulation: Relative Amplitude of Fundamental Mode**	**Eigenanalysis: Frequencies of Unstable Modes (Hz)**	**Correlation Coefficients: Simulation to Eigenanalysis**
Sliding controlled Case 1	27.3	0.881	3.3 22.5 30.8 20.6	0.739 0.667 0.272 0.354
Sliding controlled Case 2	31.3	0.972	28.0	0.974

5.6 Discussion

Unstable and neutrally-stable (periodic) modes were identified for the sliding-controlled model of flagella motion[75]–[77]. The sliding-controlled model is characterized by sliding impedances with negative effective stiffness and friction coefficients. We confirmed the existence of a periodic solution with the mode shape and frequency presented in [75] for the case of the fixed-free flagellum at specific parameter values (Table 5.1). This periodic mode closely resembles observed flagella behavior. However, at the same parameter values that give rise to this neutrally stable periodic mode, multiple unstable modes exist, some of which exhibit retrograde (distal-to-proximal) wave propagation. Such unstable modes would dominate the response of a physical system. The methods of Riedel-Kruse [75] are sufficient to identify periodic modes, but eliminate by definition the possibility of non-periodic (expanding) modes. The existence of unstable modes at the same parameter values suggests that the sliding-controlled hypothesis as formulated here is not sufficient to describe flagellar motion.

The nonlinear versions of these models, which more closely approximate the physical situation, were explored by time-domain simulation. Even in the nonlinear regime, unstable modes of the linearized models have pronounced effects on observed behavior. The results of this study complement the recent observation that distinct nonlinear modes of deformation in flagella models may arise at large amplitudes [107] leading to asymmetric waveforms.

In conclusion, the existence of unstable retrograde (tip-to-base) modes in current sliding-controlled models, with both fixed and sliding boundary conditions at the base, weakens the argument for this mechanism as the sole regulator of dynein coordination. The further development of mathematical models of flagella motion is a topic of active research; the stability properties and propagation directions of all modes should be considered in evaluating proposed mathematical models.

Chapter 6

Mathematical Formulation of the Geometric Clutch Hypothesis[2]

Dynein attachment and force generation, like many biological processes, is stochastic[55]. The principles governing dynein regulation are not necessarily prescribed steps, but the result of increased probability of attachment and subsequent force generation. In this chapter, the probability of dynein attachment is modeled as a function of inter-doublet separation. Principles of inter-doublet tension and curvature feedback are extended to a continuum model that displays anterograde (base-to-tip) bend propagation and *Chlamydomonas*-like waveforms.

6.1 Introduction and Motivation

In contrast to the displacement-driven control of the SC model, a dynein control model was proposed by Lindemann in 1994 in which transverse force across the axoneme diameter controls dynein binding. The geometric distance between adjacent microtubules governs the probability of dynein attachment, thus it has been referred to as a ‘geometric clutch’ (GC) [79], [80]. Discrete computer models were examined by Lindemann and give promising results to matching physical observations of flagella, however a continuum model of these processes, expressed as in terms of partial differential equations, has so far been lacking[80], [82]. In this chapter we explore and derive a complete continuum model of the axoneme. Here, local positive feedback in

---

[2] Formulation of the geometric clutch as a continuum model, presented in this chapter, is published in part in the *Biophysical Journal* [84]. KW contributed to equation derivations, figures, and discussions on stability.

dynein recruitment is balanced by global negative feedback associated with inter-doublet separation, which is driven in turn by curvature and the difference in doublet tension.

6.2 Model: Two Doublet Pairs

Generalizing to a continuum model, we split the axoneme into 2 sides: a principal bend side (labeled P in Figure 6.1, where active dynein forces generate a negative moment) and a reverse bend side (labeled R in Figure 6.1, where active dynein forces generate a positive moment). Note that the dynein activity is constant per side, but may oppose or contribute to passive shear forces/moments based on the local curvature of the flagellum (positive curvature is show in the upper part of Figure 6.1, negative curvature is shown in the bottom part of Figure 6.1).

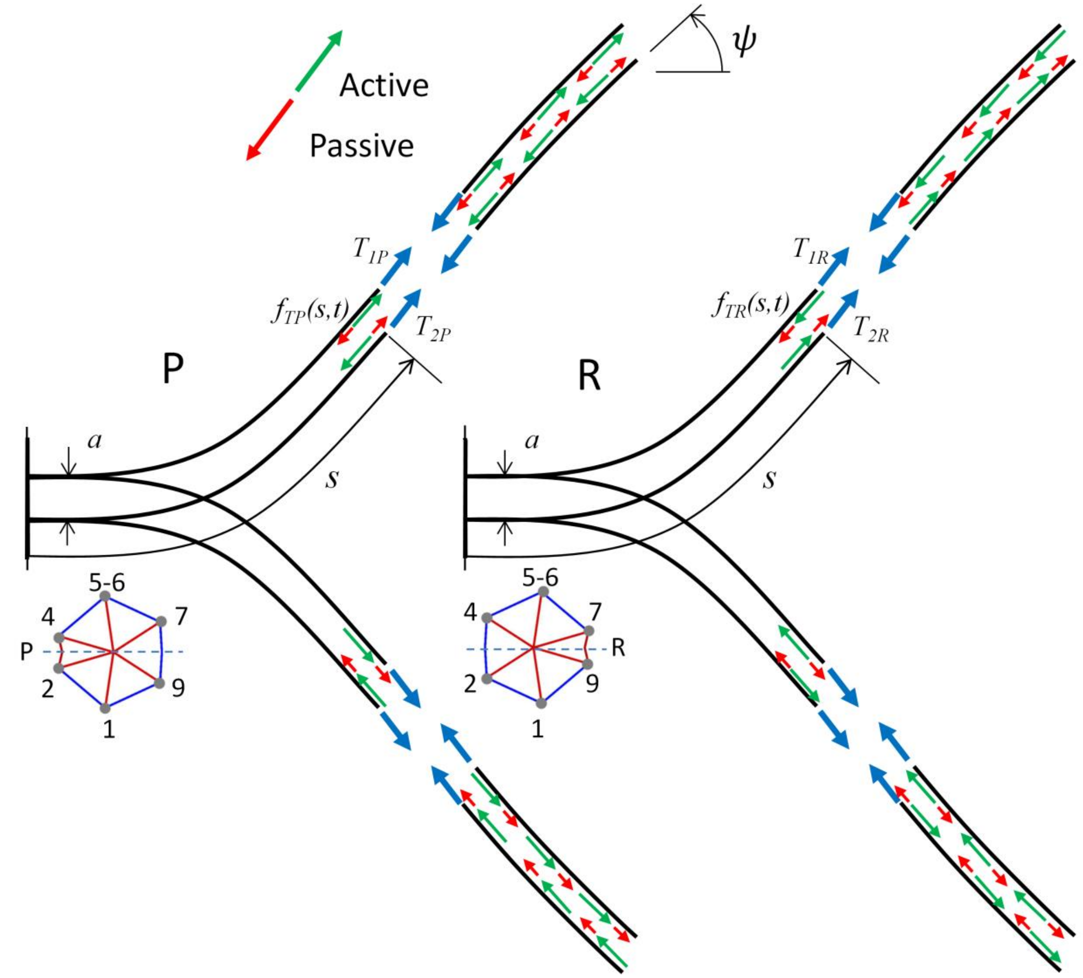

Figure 6.1 – Schematic of two doublet-pair model

The simplified GC model is based on two pairs of doublets driving flagellar bending. Side views of P and R doublet pairs show effective diameter a, active (green) and passive (red) shear forces (total shear given by $f_{TP}(s,t)$ and $f_{TR}(s,t)$) and internal doublet tension (T_{1P}, T_{2P}, T_{1R}, T_{2R}). Schematic cross-sectional views illustrate activity of P and R doublet pairs on a simplified hexagonal axoneme structure (distortion is exaggerated). P activity drives doublet 4 tip-ward relative to doublet 2; R activity drives doublet 9 tip-ward relative to doublet 7. The dashed line segment, formed by connecting doublets 3 and 8, is normal to the beat plane.

6.3 Doublet Pair Interactions

6.3.1 Equilibrium Equations

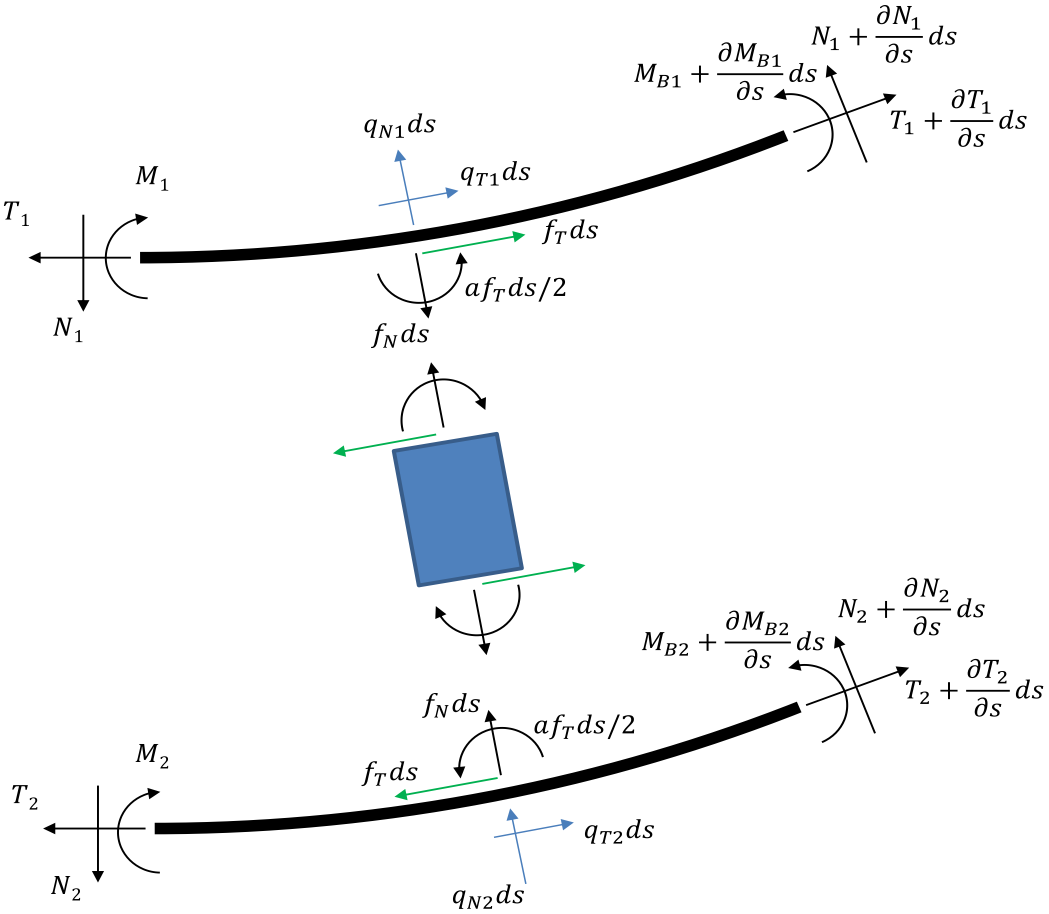

Figure 6.2 – Free body diagram of a single doublet pair
Each doublet, or filament, may support a tension T, normal force N, and moment M (subscripts indicate doublet within the doublet pair; upper doublet is labeled 1, lower doublet is labeled 2). In addition, the doublet pair is subject to external viscous loads q_T and q_N and inter-doublet shear and normal forces: f_T and f_N.

We consider each bending side as a separate active system of two filaments (essentially a 'flattened' equivalent construction of the axoneme) labeled 1 and 2. Within each doublet pair, we consider forces acting along and within each filament (doublet), T and N, in addition to force and moment couples between the doublets: f_T and f_N (representing all shear components, both active and passive), and the external resistance to bending due to viscous fluid, q_T and q_N (Figure 6.2).

In the most general case, shear force is generated within the axoneme and is also resisted by passive elements. The resultant total shear force is given by the term f_T and explored later in the context of specific dynein regulation mechanisms. Similar to derivations in Chapter 4, the equilibrium equations may be written for a differential element of each doublet as:

$$\begin{array}{llll}
 & \text{Doublet 1} & \text{Doublet 2} & \\
\boldsymbol{e}_T & \dfrac{\partial T_1}{\partial s} - N_1 \dfrac{\partial \psi_1}{\partial s} + f_T + q_{T1} = 0 & \dfrac{\partial T_2}{\partial s} - N_2 \dfrac{\partial \psi_2}{\partial s} - f_T + q_{T2} = 0 & (6.1) \\
\boldsymbol{e}_N & \dfrac{\partial N_1}{\partial s} + T_1 \dfrac{\partial \psi_1}{\partial s} - f_N + q_{N1} = 0 & \dfrac{\partial N_2}{\partial s} + T_2 \dfrac{\partial \psi_2}{\partial s} + f_N + q_{N2} = 0 & (6.2)
\end{array}$$

The moment balance within a differential element along each doublet may be written:

$$\frac{\partial M_{B1}}{\partial s} + \frac{a}{2} f_T + N_1 = 0 \qquad \frac{\partial M_{B2}}{\partial s} + \frac{a}{2} f_T + N_2 = 0 \tag{6.3}$$

We define the net tangential force in the element $T = T_1 + T_2$, the net normal force $N = N_1 + N_2$, and the total moment due to elastic bending $M_B = M_{B1} + M_{B2}$. The mean angle $\psi = (\psi_1 + \psi_2)/2$ defines the shape of the flagellum. Equations (6.1) - (6.3) can be combined with the constitutive equations for velocity and viscous force from resistive force theory (Chapter 4, (4.13) - (4.16)) to produce overall equations of motion of the two filament system. Neglecting the small differences in curvature between the doublets ($\frac{\partial(\psi_1 - \psi_2)}{\partial s} \ll \frac{\partial \psi}{\partial s}$), the equilibrium equations reduce to those defined in Chapter 4 for a 2-D beam in viscous fluid (Equations (4.31) and (4.32)) [77], [78]. We again consider the entire flagellum as a cantilever beam with fixed-free boundaries.

6.3.2 Inter-Doublet Separation and Transverse Force

The inter-doublet shear force $f_T(s, t)$ includes dynein activity as well as passive shear resistance, and may be related to mechanical variables such as curvature, inter-doublet sliding velocity, or microtubule displacement. In the GC hypothesis dynein is regulated by the transverse distance between doublets [80], [82], [83]. Here, we derive continuum mechanical equations that govern inter-doublet separation, allowing each individual filament to bend, resulting in a slight difference between ψ_1, ψ_2, and ψ. Subtracting Equation $(6.1)_2$ from $(6.1)_1$, and likewise for Equations (6.2) and (6.3) we obtain

$$\frac{\partial(T_1-T_2)}{\partial s}-\left(N_1\frac{\partial\psi_1}{\partial s}-N_2\frac{\partial\psi_2}{\partial s}\right)+2f_T+(q_{T1}-q_{T2})=0 \tag{6.4}$$

$$\frac{\partial(N_1-N_2)}{\partial s}+\left(T_1\frac{\partial\psi_1}{\partial s}-T_2\frac{\partial\psi_2}{\partial s}\right)-2f_N+(q_{N1}-q_{N2})=0 \tag{6.5}$$

$$\frac{\partial(M_{B1}-M_{B2})}{\partial s}+(N_1-N_2)=0 \tag{6.6}$$

Denoting the change in separation between the doublets as h, applied evenly between the two doublets, the inter-doublet distance is $a-h$ (Figure 6.3). The tangent angle of individual filaments is related to the overall tangent angle by:

$$\psi_1=\psi-\frac{1}{2}\frac{\partial h}{\partial s} \qquad \psi_2=\psi+\frac{1}{2}\frac{\partial h}{\partial s} \qquad \psi_1-\psi_2=\frac{-\partial h}{\partial s} \tag{6.7}$$

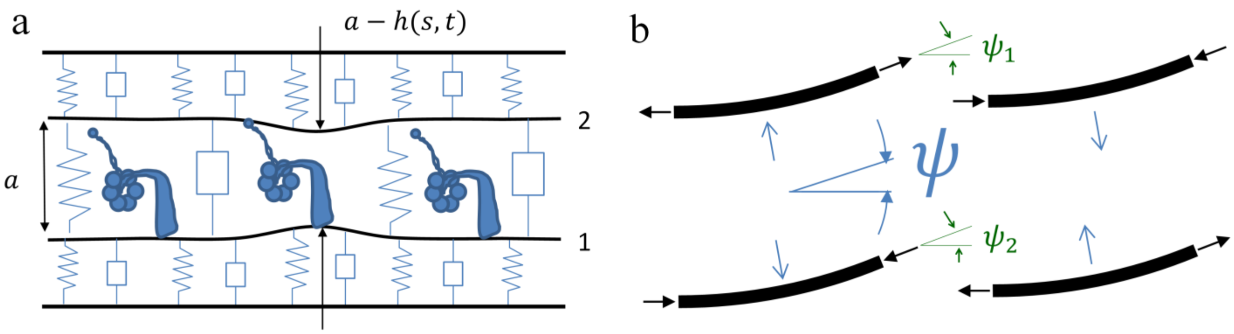

Figure 6.3 – Schematic diagrams of inter-doublet separation.
(a) Doublet spacing with zero mean curvature. Inter-doublet spacing is a smooth function of axial position, s, modulated by doublet flexural modulus and active and passive axoneme components. Shapes and sizes are exaggerated for illustration. (b) Effect of curvature and doublet tension (small arrows at ends of doublets) on inter-doublet force; blue arrows illustrate resultants. Individual doublet angle $\psi_i$may vary slightly from overall angle ψ.

We note that $h \ll a \ll L$ and $\frac{\partial h}{\partial s} \ll \psi$. We assume the distributed viscous forces act approximately equally on both doublets $(q_{T1} - q_{T2}) \approx (q_{N1} - q_{N2}) \approx 0$, and that the constitutive relationship for each doublet is

$$M_{B1} = EI_d \frac{\partial \psi_1}{\partial s} \qquad\qquad M_{B2} = EI_d \frac{\partial \psi_2}{\partial s} \tag{6.8}$$

where EI_d is the flexural modulus of an individual doublet. Eliminating terms and substituting the identities of (6.7), Equations (6.4) and (6.5) become:

$$\frac{\partial (T_1 - T_2)}{\partial s} + \frac{\partial \psi}{\partial s}(N_2 - N_1) + \frac{1}{2}\frac{\partial^2 h}{\partial s^2}(N_2 + N_1) + 2f_T = 0 \tag{6.9}$$

$$\frac{\partial (N_1 - N_2)}{\partial s} + \frac{\partial \psi}{\partial s}(T_1 - T_2) - \frac{1}{2}\frac{\partial^2 h}{\partial s^2}(T_1 - T_2) - 2f_N = 0 \tag{6.10}$$

Substituting the spatial derivative of (6.6), definitions for N and T, and defining $S = T_1 - T_2$:

$$\frac{\partial S}{\partial s} - \frac{\partial \psi}{\partial s}\left(EI_d \frac{\partial^3 h}{\partial s^3}\right) + \frac{1}{2}\frac{\partial^2 h}{\partial s^2}(N) + 2f_T = 0 \tag{6.11}$$

$$EI_d \frac{\partial^4 h}{\partial s^4} + \frac{\partial \psi}{\partial s}(S) - \frac{1}{2}\frac{\partial^2 h}{\partial s^2}(S) - 2f_N = 0 \tag{6.12}$$

Ignoring small nonlinear terms (their inclusion in the full model is straightforward and does not perceptibly affect results), Equations (6.11) and (6.12) reduce to:

$$S = 2\int_s^L f_T \, d\zeta \tag{6.13}$$

$$EI_d \frac{\partial^4 h}{\partial s^4} = 2f_N - S\frac{\partial \psi}{\partial s} \tag{6.14}$$

Equations (6.13) and (6.14) are key equations define the inter-doublet separation h in terms of the transverse internal force (f_N) and the curvature of the flagellum ($\frac{\partial \psi}{\partial s}$), which is modulated by the difference in inter-doublet tensions (S). To solve Equation (6.14) we again consider a fixed-free system, but in terms of inter-doublet separation h:

(i) Zero deflection at base: $h(0,t) = 0$

(ii) Zero angle of deflection at base: $\frac{\partial h}{\partial s}(0,t) = 0$

(iii) Zero bending moment at distal end: $\frac{\partial^2 h}{\partial s^2}(L,t) = 0$ (6.15)

(iv) Zero transverse force at distal end: $\frac{\partial^3 h}{\partial s^3}(L,t) = 0$

6.3.3 Cross-Bridge Attachment and Dynein Activity

Inter-doublet forces f_T and f_N are summary terms that include all active and passive contributions to shear. We separate the active and passive forces based on estimates of dynein activity and slender beam mechanics. The active force is modeled by a constant maximum active force ($\bar{f}_T$ or $\bar{f}_N$) multiplied by the aggregate probability of dynein cross-bridge attachment, p. Passive shear and transverse forces oppose the active forces, and are assumed to be proportional to the corresponding components of displacement (Δ) and sliding velocity ($\frac{\partial \Delta}{\partial t}$) (with proportionality constants k_T, b_T in the tangential direction and k_N, b_N in the normal direction). The inter-doublet sliding displacement $\Delta(s,t) = a\psi(s,t)$ when the base is fixed ($\psi(0,t) = 0$ and $\Delta(0,t) = 0$) [75], [78]. The tangential and normal inter-doublet forces can be defined:

$$f_T = \bar{f}_T p - k_T a\psi - b_T a\frac{\partial \psi}{\partial t} \tag{6.16}$$

$$f_N = \bar{f}_N p - k_N h - b_N \frac{\partial h}{\partial t} \tag{6.17}$$

The probability of dynein attachment p determines the overall active force generated within the beam, governed in the GC model by inter-doublet separation h [79], [80], [82]. We assume the variable p increases with a specified rate constant toward a maximum probability value p_1 when

h exceeds a threshold, h_{on}, and decreases to a baseline probability value (p_0) when h is less than a different threshold, h_{off}. This behavior is captured by the following equations and illustrated in Figure 6.4. The variable A represents "activation" of dynein and modulates the probability of attachment. Recall h is defined as positive when doublets are close together. Deflections are defined relative to $h_{max} = p_1\bar{f}_N/k_N$:

$$p = p_0 + A(p_1 - p_0) \tag{6.18}$$

$$\frac{\partial A}{\partial t} = K_{on}(1-A) - K_{off}A \tag{6.19}$$

$$K_{off}(h) = \frac{K_0}{1+\exp\left(20(h-h_{off})\,/h_{max}\right)} \tag{6.20}$$

$$K_{on}(h) = \frac{K_0}{1+\exp(20(h_{on}-h)\,/h_{max})} \tag{6.21}$$

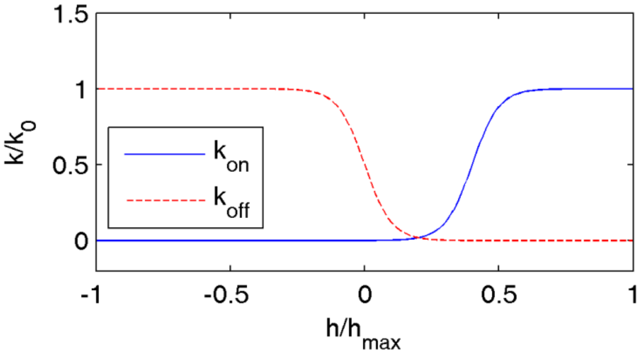

Figure 6.4 – Effect of inter-doublet separation on the rate of cross-bridge attachment or detachment
When the doublets become sufficiently close ($h > h_{on}$) attachment probability increases at a characteristic rate, k_0. When h drops below a different threshold ($h < h_{off}$) the probability of attachment decreases at rate that approaches k_0. Governed by Equations (6.20) - (6.21).

Incorporation of the effects of inter-doublet separation on dynein activity completes the basic model of flagella motion. Summarizing the continuum version of GC model, the coupled equations for ψ, N, T, h, A, and S are written together in Table 6.4.

Table 6.4 – Summary of equations of flagella motion and inter-doublet separation

Nonlinear Equations of Motion	
Tangential force balance (4.29)	$T_{,ss} - N\psi_{,ss} - \left(1+\frac{c_T}{c_N}\right)N_{,s}\psi_{,s} - \frac{c_T}{c_N}T\psi_{,s}^2 = 0$
Normal force balance (4.23)	$N_{,ss} + \left(1+\frac{c_N}{c_T}\right)T_{,s}\psi_{,s} + T\psi_{,ss} - \frac{c_N}{c_T}N\psi_{,s}^2 = c_N\psi_{,t}$
Moment balance (4.24), sign of shear force f_T switched to match GC equations and references)	$EI\psi_{,ss} + af_T + N = 0$
Inter-Doublet Forces	
Inter-doublet separation (6.14)	$EI_d\frac{\partial^4 h}{\partial s^4} = 2f_N - S\frac{\partial\psi}{\partial s}$
Tension difference in doublets (6.13)	$S = 2\int_s^L f_T d\zeta$
Tangential inter-doublet force density (6.16)	$f_T = \bar{f}_T p - k_T a\psi - b_T a\frac{\partial\psi}{\partial t}$
Normal inter-doublet force density (6.17)	$f_N = \bar{f}_N p - k_N h - b_N\frac{\partial h}{\partial t}$
Dynein Activity	
Cross-bridge attachment probability (6.18)	$p = p_0 + A(p_1 - p_0)$
Cross-bridge attachment dynamics (6.19)	$\frac{\partial A}{\partial t} = K_{on}(1-A) - K_{off}A$
Detachment rate (6.20)	$K_{off}(h) = \frac{K_0}{1+\exp\left(20(h-h_{off})/h_{max}\right)}$
Attachment rate (6.21)	$K_{on}(h) = \frac{K_0}{1+\exp(20(h_{on}-h)/h_{max})}$

6.4 Opposing Doublet Pairs

The equations summarized in Table 6.4 describe the mechanics by which dynein activity might lead to global flagella bending and inter-doublet separation in a flagellum with a single pair of doublets. However, as written above these equations will only produce active bending in one direction, and will not lead to oscillations. To explain this switching behavior, we invoke the widely accepted notion that two subsystems exist (Figure 6.1), each consisting of a set of doublets and associated dynein motors [80], [82] and governed by a set of equations like those in Table 6.4. The principal (P) bend subsystem comprises doublets 2-4 and the reverse (R) subsystem comprises doublets 7-9 (Figure 6.1). The resulting equations for the two sides are tabulated in Table 6.5.

The equations for the R side are identical to those of the P side, after replacing P with R, except that the active force ($-\bar{f}_T p_R$) is negative as it bends the flagella in the opposite direction. The equations of global flagella motion (Equations (4.23), (4.24), (4.29), and Table 6.4) remain the same except that activity on both the P and R sides contributes to the total active bending moment: $af_T = a(f_{TP} + f_{TR})$. To model asymmetric beating, values of parameters (such as h_{on} or h_{off}) may differ between sides P and R.

Table 6.5 – Equations for principal (P) and reverse (R) doublet pairs

	Principal (P)	**Reverse (R)**
Inter-doublet separation	$EI_d \frac{\partial^4 h_P}{\partial s^4} = 2f_{NP} - S_P \frac{\partial \psi}{\partial s}$	$EI_d \frac{\partial^4 h_R}{\partial s^4} = 2f_{NR} - S_R \frac{\partial \psi}{\partial s}$
Tension difference	$S_P = 2\int_s^L f_{TP} d\zeta$	$S_R = 2\int_s^L f_{TR} d\zeta$
Tangential force density	$f_{TP} = \bar{f}_T p_P - k_T a\psi - b_T a \frac{\partial \psi}{\partial t}$	$f_{TR} = -\bar{f}_T p_R - k_T a\psi - b_T a \frac{\partial \psi}{\partial t}$
Normal force density	$f_{NP} = \bar{f}_N p_P - k_N h_P - b_N \frac{\partial h_P}{\partial t}$	$f_{NR} = \bar{f}_N p_R - k_N h_R - b_N \frac{\partial h_R}{\partial t}$
Attachment probability	$p_P = p_0 + A_P(p_1 - p_0)$	$p_R = p_0 + A_R(p_1 - p_0)$
Attachment dynamics	$\frac{\partial A_P}{\partial t} = K_{on}(1 - A_P) - K_{off} A_P$	$\frac{\partial A_R}{\partial t} = K_{on}(1 - A_R) - K_{off} A_R$
Attachment rate	$K_{off}(h_P) = \frac{K_0}{1 + \exp\left(20\left(h_P - h_{off}\right)/h_{max}\right)}$	$K_{off}(h_R) = \frac{K_0}{1 + \exp\left(20\left(h_R - h_{off}\right)/h_{max}\right)}$
Detachment rate	$K_{on}(h_P) = \frac{K_0}{1 + \exp(20(h_{on} - h_P)/h_{max})}$	$K_{on}(h_R) = \frac{K_0}{1 + \exp(20(h_{on} - h_R)/h_{max})}$

6.4.1 Inter-Doublet Equations: Two Doublet Model

In the GC model, the net shear force is $f_T = f_{TP} + f_{TR}$, where f_{TP} and f_{TR} are the net shear forces in the principal and reverse directions, exerted between pairs of doublets on opposite sides of the axoneme. Including shear forces due to passive stiffness and friction, net shear force may be expressed as [84]:

$$f_T = f_{TP} + f_{TR} = \bar{f}_T p_P - k_T a\psi - b_T a \frac{\partial \psi}{\partial t} - \bar{f}_T p_R - k_T a\psi - b_T a \frac{\partial \psi}{\partial t} \tag{6.22}$$

$$f_T = \bar{f}_T (A_P - A_R)(p_1 - p_0) - 2k_T a\psi - 2b_T a \frac{\partial \psi}{\partial t} \tag{6.23}$$

Changing the sign of the active shear force f_T to match that of [75] and [77] (which is opposite that of [84]) and defining the net dynein activity in the principal bend direction $A = A_P - A_R$ the inter-doublet shear force may be written:

$$f_T = \bar{f}_T(p_1 - p_0)A + 2k_T a\psi + 2b_T a\frac{\partial\psi}{\partial t} \tag{6.24}$$

Internal normal forces are not assumed to be additive in the same manner as tangential forces due to the geometry of the flagellum, thus the general expression for f_N (6.17) may be combined with the equation for inter-doublet separation (6.14):

$$EI_d\frac{\partial^4 h}{\partial s^4} + 2k_N h + 2b_N\frac{\partial h}{\partial t} = 2\bar{f}_N[p_0 + (p_1 - p_0)A] - S\frac{\partial\psi}{\partial s} \tag{6.25}$$

6.4.2 Load Dynamics of Inter-Doublet Separation

The activation variable A is governed by Equation (6.19). The local dynamics of Equations (6.25) and (6.19) may be examined by ignoring spatial variations in h and A and uncoupling the resulting equations from the global flagellar motion (letting $S\frac{\partial\psi}{\partial s} = 0$). This leads to a pair of ordinary differential equations (ODEs):

$$\frac{dh}{dt} = \frac{\bar{f}_N(p_1 - p_0)}{b_N}A - \frac{k_N}{b_N}h + \frac{\bar{f}_N}{b_N}p_0 \tag{6.26}$$

$$\frac{dA}{dt} = K_{on}(1 - A) - K_{off}A \tag{6.27}$$

The nullclines of this system (where $\frac{dh}{dt} = 0$ or $\frac{dA}{dt} = 0$) are shown in Figure 6.5(a). For illustrative purposes we consider the case $p_0 = 0$; other parameters are as in Table 6.6. The intersections of the nullclines define the equilibria (fixed points) of the local system.

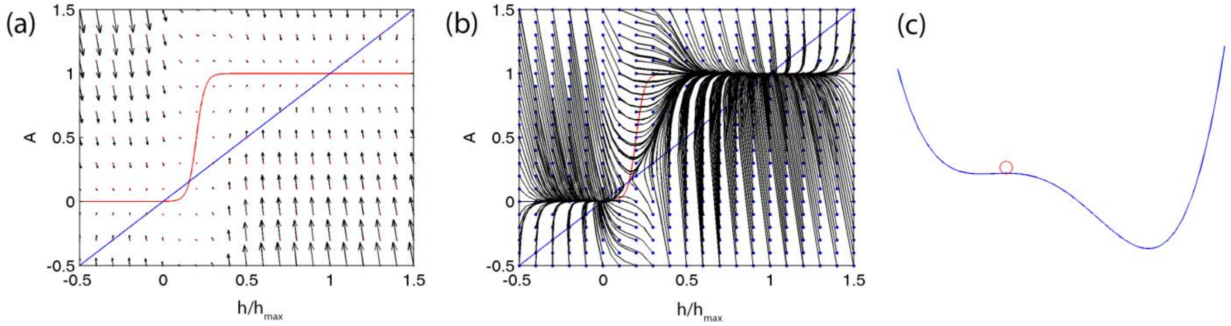

Figure 6.5 – Dynamics of inter-doublet separation variables A and h.
(a) Nullclines and vector field corresponding to the local dynamics of inter-doublet separation: Equations (6.26) and (6.27). (b) Trajectories in the $A - h$ plane rapidly approach a curve representing the quasi-equilibrium value of A for a given value of h: $A_{eq}(h)$. (c) The system approaches the behavior of a particle on a curved surface with two stable equilibria separated by an unstable equilibrium.

Table 6.6 – Parameter values of the continuum GC model [84] (L, EI, a, c_N are as in Table 5.1)

Parameter	**Value**	**Units**	**Description**
τ	0.05	s	Dynein time constant
p_0	0.05	1	Baseline probability of crosslinking
p_1	0.15	1	Maximum probability of crosslinking
f_T	2000	pN/μm	Maximum dynein force per unit length
k_T	12.5	pN/μm^2	Passive shear stiffness
b_T	0.25	pN-s/μm^2	Passive shear friction
k_N	500	pN/μm^2	Passive normal stiffness
b_N	10	pN-s/μm^2	Passive normal friction
C_S	0.50	μm/ pN-s	Interdoublet force and dynein coupling factor
k_3	30	pN/μm^4	Nonlinear shear stiffness

At the parameter values listed in Table 6.6, the behavior of the local 2D system is closely approximated by a 1D sub-system, as the cross-bridge variable (A) approaches a quasi-equilibrium for each value of inter-doublet spacing (h). Trajectories from many initial conditions are shown in Figure 6.5(b); trajectories rapidly approach a curve that comprises the unstable manifold of the unstable fixed point and the stable manifolds of the two locally stable fixed points. Trajectories then more slowly approach one of the stable fixed points. The asymptotic behavior resembles that of a damped particle on the energy surface of Figure 6.5(c).

After the initial transient, the inter-doublet separation is well described by the simplified model:

$$\frac{dh}{dt} \approx \frac{\bar{f}_N(p_1 - p_0)}{b_N} A_{eq}(h) - \frac{k_N}{b_N} h \tag{6.28}$$

Examining the plots of dh/dt vs h and dA/dt vs A (Figure 6.6) in this local system, it is apparent that the right hand side of Equation (6.28) may be approximated by a cubic polynomial function, as in many excitable systems (Fitzhugh-Nagumo, e.g.). Thus, local dynamics of h follow:

$$\frac{dh}{dt} \approx C_h h(h - h_{th})(h_{max} - h) \tag{6.29}$$

where $h_{max} = \bar{f}_N(p_1 - p_0)/k_N$. The other parameters of the cubic analogy, C_h and h_{th}, depend on k_N, b_N, h_{on} , and h_{off}. Similarly, the local dynamics of the attachment variable A may be approximated by (Figure 6.6(c)):

$$\frac{dA}{dt} \approx E(A) = C_A A(A - A_{th})(1 - A) \tag{6.30}$$

If we make the corresponding approximation in the equation of inter-doublet separation (6.25) we obtain:

$$\frac{\partial h}{\partial t} = -\frac{EI_d}{2b_N}\frac{\partial^4 h}{\partial s^4} + C_h h(h - h_{th})(h_{max} - h) - \frac{S}{2b_N}\frac{\partial \psi}{\partial s} \tag{6.31}$$

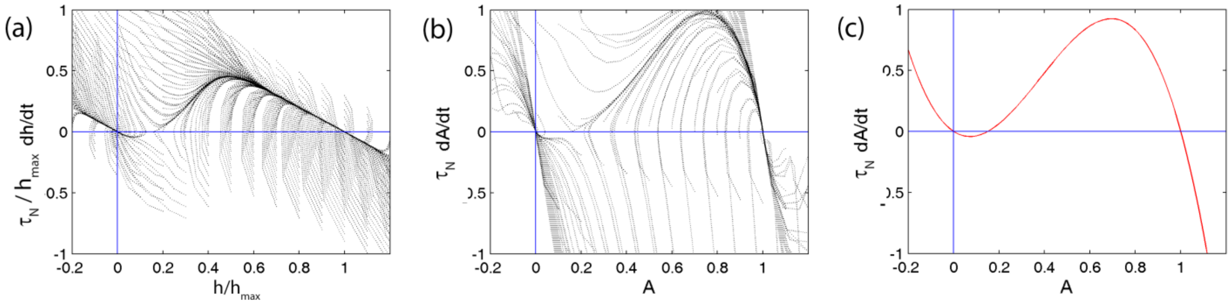

Figure 6.6 – Analogous equations for A and h
Trajectories in (a) the $dh/dt - h$ plane and (b) the $dA/dt - A$ plane rapidly approach 1-D curves as in Figure 6.5. These curves resemble cubic polynomial functions with three zeros representing two stable equilibria and one unstable (threshold) equilibrium. (c) The cubic polynomial analogy to local attachment dynamics: $\frac{\partial A}{\partial t} \approx E(A) = C_A A(A - A_{th})(1 - A)$. Derivatives are normalized by $\tau_N = b_N/k_N$.

Excluding the last term, Equation (6.31) is a form of the parabolic nonlinear 4th order PDE with bi-stable nonlinearity known as the extended Fisher-Kolmorogov (EFK) equation [108]. The term $S\frac{\partial \psi}{\partial s}$ couples this system to global flagella motion. This equation (with $S\frac{\partial \psi}{\partial s} = 0$) is analogous to the classic reaction-diffusion system, and is known to exhibit traveling wave front solutions [106]. Figure 6.7 shows examples of propagation of an initial disturbance in h at the left end of the domain, using (a) the original model with cross-bridge kinetics (Equations (6.25) and (6.19)) and (b) the cubic approximation, Equation (6.31), showing the cubic approximation exhibits very similar propagation to the original PDE [84].

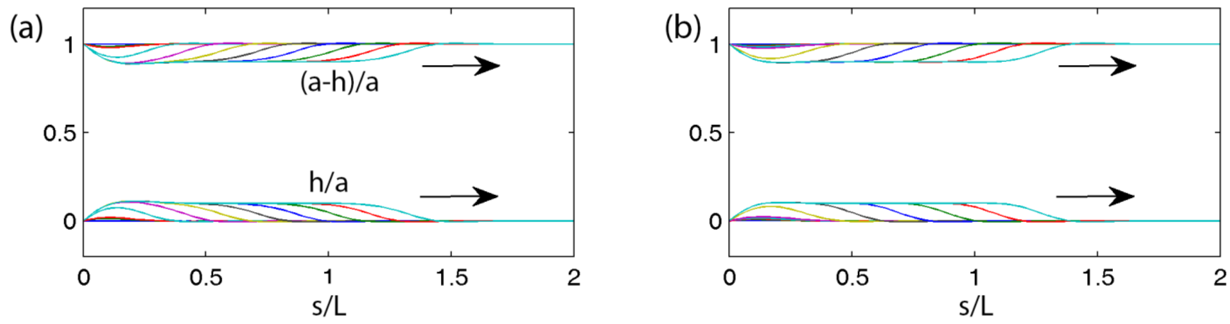

Figure 6.7 – Propagation of inter-doublet separation
(a) The decrease in separation $h(s,t)$ is computed from the original PDE of inter-doublet separation (Equations (6.25) and (6.19)), and plotted vs s/L at discrete times $t = 0.025\,n$, n=1, 2, ..20. (b) Solutions of the simplified excitable system (Equation (6.31)) plotted vs. s/L at the same discrete times. Note the domain is extended to $s = 2L$ to better visualize propagation.

Thus the equations of inter-doublet separation and dynein activity, uncoupled from the global motion of the flagellum, clearly support propagation of disturbances. Results from theoretical studies of the EFK equation [39], [105], [106], [108]–[110] can illuminate the relationship between flagella properties and behavior.

6.5 Stability Analysis

To produce flagellar motion, dynein activity not only propagates, but also changes flagellar curvature and periodically and autonomously switches the direction of bending. This behavior is exhibited by the discrete GC model [79], [80], [82] and is replicated by the current set of PDEs. We will first consider small-amplitude (linear) motion. *Chlamydomonas* flagella exhibit small-amplitude, symmetric oscillations which propel the cells backward under conditions of increased cytosolic calcium concentration [36], [111], [112].

6.5.1 Linearized Equations of Motion

As described in Chapter 5, for small-amplitude motion about a straight equilibrium conformation Equations (4.31) - (4.32) can be reduced by eliminating nonlinear terms, leading to a single equation [75], [77], [113]:

$$EI\psi_{,ssss} + af_{T_{,ss}} + c_N\psi_{,t} = 0 \tag{6.32}$$

In the GC model, dynein activity on both the principal and recovery bends is encompassed in the shear force term f_T. All equations necessary to describe f_T are given in Table 6.6 and examined in Equation (6.23). Considering previous analysis of local dynamics (Figure 6.5, Figure 6.6) dynein activity on each side of the beam is governed by an equation like:

$$\frac{\partial A_P}{\partial t} \approx \frac{\partial h_P}{\partial t} \cdot \frac{dA_{eq}}{dh} \tag{6.33}$$

Dynein activity is thus governed by the propagation dynamics of Equation (6.31) coupled to global flagella motion by tension and curvature ($S_P \frac{\partial \psi}{\partial s}$ or $S_R \frac{\partial \psi}{\partial s}$). After adding the two sides together and linearizing, only the baseline difference in tension, S_0, appears in the equation governing net dynein activity, A. The following expressions are obtained [84]:

$$\frac{\partial A}{\partial t} = -\left(\frac{1}{\tau_N}\right) A - C_S S_0 \frac{\partial \psi}{\partial s} + \frac{EI_d}{2b_N} \frac{\partial^4 A}{\partial s^4} \tag{6.34}$$

$$S_0 = 2 \int_s^L \bar{f}\, p_0 \, d\zeta = -2\bar{f} p_0 (L - s) \tag{6.35}$$

The time constant $\tau_N = b_N / k_N$ describes the local (linearized) behavior of A; the new variable S_0 is the baseline difference in tension in the doublets. This resting difference in tension provides a baseline level of coupling between curvature and dynein activity even when the flagellum is almost straight. The parameter $C_S = (\frac{dA_{eq}}{dh})/2b_N$ controls the magnitude of the coupling [84]. The stability of a straight flagellum is significantly affected when $S_0 \neq 0$.

6.5.2 Eigenvalue Problem for the GC Model

Similar to Chapter 5, we assume the flagellar waveform is separable and seek generalized solutions of the form [75]–[77]:

$$\psi(s,t) = \tilde{\psi}(s)\exp(\sigma t) \qquad f_T(s,t) = \tilde{f}_T(s)\exp(\sigma t) \qquad A(s,t) = \tilde{A}(s)\exp(\sigma t) \tag{6.36}$$

We again use the exponential term $\sigma = \alpha + i\omega$ where α and ω are real to allow all possible (stable and unstable) solutions. Each such solution $\tilde{\psi}$ that satisfies the equation of motion and all boundary conditions is a solution mode. If $\alpha > 0$, the mode grows exponentially. If m such modes are found with exponents σ_m and shape $\tilde{\psi}^{(m)}(s)$, then a solution can also be formed from any linear combination of these modes: $\psi(s,t) = \sum_{m=1}^{M} a_m e^{\sigma_m t}\,\tilde{\psi}^{(m)}(s)$. In general, for arbitrary initial conditions, the least stable mode will dominate the response.

To illuminate the mechanisms of mechanical feedback from flagellar shape and facilitate comparison to other models, we neglect for the moment the relatively small 4th order spatial derivative term in Equation (6.34). The resulting expressions can be combined and simplified to obtain an ordinary differential equation (ODE) in $\tilde{\psi}$:

$$EI\frac{d^4\tilde{\psi}}{ds^4} - c_1(\sigma)\frac{d^2}{ds^2}\left[(1 - s/L)\frac{d\tilde{\psi}}{ds}\right] - c_2(\sigma)\frac{d^2\tilde{\psi}}{ds^2} + \sigma c_N\tilde{\psi} = 0 \tag{6.37}$$

with coefficients:

$$c_1(\sigma) = 2p_0(p_1 - p_0)a\bar{f}_T^2 C_S\tau_N L/(\tau_N\sigma + 1) \tag{6.38}$$

$$c_2(\sigma) = 2a^2(k_T + \sigma b_T) \tag{6.39}$$

In non-dimensional form the equation becomes

$$\tilde{\psi}'''' - [\bar{c}_1(\bar{\sigma})(1 - \bar{s})\tilde{\psi}']'' - \bar{c}_2(\bar{\sigma})\tilde{\psi}'' + \bar{\sigma}\tilde{\psi} = 0 \tag{6.40}$$

or its equivalent,

$$\tilde{\psi}'''' - \bar{c}_1(\bar{\sigma})(1 - \bar{s})\tilde{\psi}''' - [\bar{c}_2(\bar{\sigma}) - 2\bar{c}_1(\bar{\sigma})]\tilde{\psi}'' + \bar{\sigma}\tilde{\psi} = 0 \tag{6.41}$$

where the new non-dimensional parameters are $\bar{c}_1 = c_1L^2/EI$ and $\bar{c}_2 = c_2L^2/EI$.

It is apparent that the GC model includes feedback from both curvature (the term containing $\tilde{\psi}'''$) and shear deformation (the term containing $\tilde{\psi}''$). Notably, both terms become more destabilizing when $c_1(\sigma)$ increases [84]. An important feature of the curvature-feedback term in the GC model is the proportionality to $1-\bar{s}$. The feedback is thus strongest at the proximal end, which encourages switching at the base and proximal-to-distal bend propagation. The factor of $1-\bar{s}$ also complicates the solution of the eigenvalue problem, so that numerical methods (finite element calculations or weighted residuals, e.g.) are required to find the natural modes and frequencies of oscillation.

6.5.3 Numerical Eigenanalysis and Simulation

The method of weighted residuals is well-suited to this problem, as the flagella eigenfunctions can be constructed from the vibration modes of an Euler-Bernoulli beam with corresponding boundary conditions. Stability analysis of the linearized equations of motion (Equation (6.41) and fixed-free boundary conditions) was performed by using the method of weighted residuals [105] with up to $N = 12$ test functions to obtain a matrix form of the eigenvalue problem. The resulting matrix eigenvalue problem was solved using MATLAB software (The Mathworks, Natick, MA). The free vibration modes of a uniform, fixed-free beam were used as trial and test functions.

To check the stability of the solution and characterize subsequent behavior, solutions to the equations of motion were also found using COMSOL. The 1-D domain was discretized into 50 elements with quartic interpolation. Eigenvalue/eigenfunction calculations (300 maximum iterations, relative tolerance 1x10^{-6}) and time-marching simulations (backward differentiation formula, variable time step, relative tolerance 1x10^{-4}) were performed. Representative results were confirmed at finer spatial resolution and smaller tolerance values.

6.5.4 Unstable Modes of the GC Model

By analogy to other models, parameter changes that increase the magnitude of the delayed curvature feedback and decrease the value of the shear feedback were expected to lead to instability. Increasing the baseline probability of cross-bridge attachment, p_0, does both. A dynamic instability occurs when complex eigenvalues cross into the right half plane (Figure 6.8) with non-zero imaginary part: $Re(\sigma) > 0; Im(\sigma) \neq 0$. Increasing the baseline probability of cross-bridge attachment, p_0, encourages instability.

Physically, the oscillations shown in Figure 6.9 can be interpreted as the result of a switching mechanism [79], [114]. Active shear in one doublet pair (for example the P side) induces a tension difference in the doublets on that side which, combined with curvature, produces a transverse force ($S_P \frac{\partial\psi}{\partial s}$) which pushes the doublets apart and eventually terminates the active shear. This transverse force corresponds to the “global transverse force” described by Lindemann [79], [80], [82]. At the same time, the corresponding passive shear force on the opposite doublet pair produces a transverse force ($S_R \frac{\partial\psi}{\partial s}$) which pulls the doublets on the passive side together and initiates active shear on that side. The modes corresponding to the 3 least stable eigenvalues are shown in Figure 6.9.

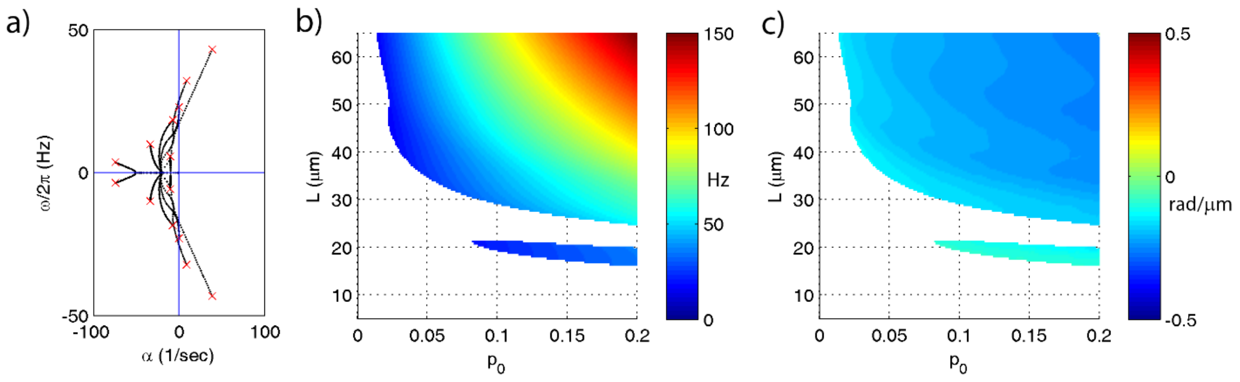

Figure 6.8 – Eigenvalues of the GC model from the weighted residual method
(a) Paths of eigenvalues $\sigma = \alpha + i\omega$ in the complex plane as p_0 is varied ($0 < p_0 < 0.2$) in the GC flagella model (6.31). Other parameters are as in Table 6.6. The red 'x' symbols denote the eigenvalues at the final value $p_0 = 0.2$. (b) Frequency $\omega/2\pi$ (Hz) of the least stable mode of the GC model as a function of flagella length and baseline probability of dynein activation, p_0. Other parameters are as in Table 6.6. At each parameter combination (p_0, L) frequency is obtained from the imaginary part $(i\omega)$ of the eigenvalue $\sigma = \alpha + i\omega$ with largest real part (α). (c) Median phase gradient, $\frac{\partial\angle\tilde{\psi}}{\partial s}$, of the least stable mode. Anterograde (proximal-distal) propagation corresponds to a phase gradient < 0, for $\omega > 0$. For all parameter combinations shown, the least stable mode exhibits anterograde propagation.

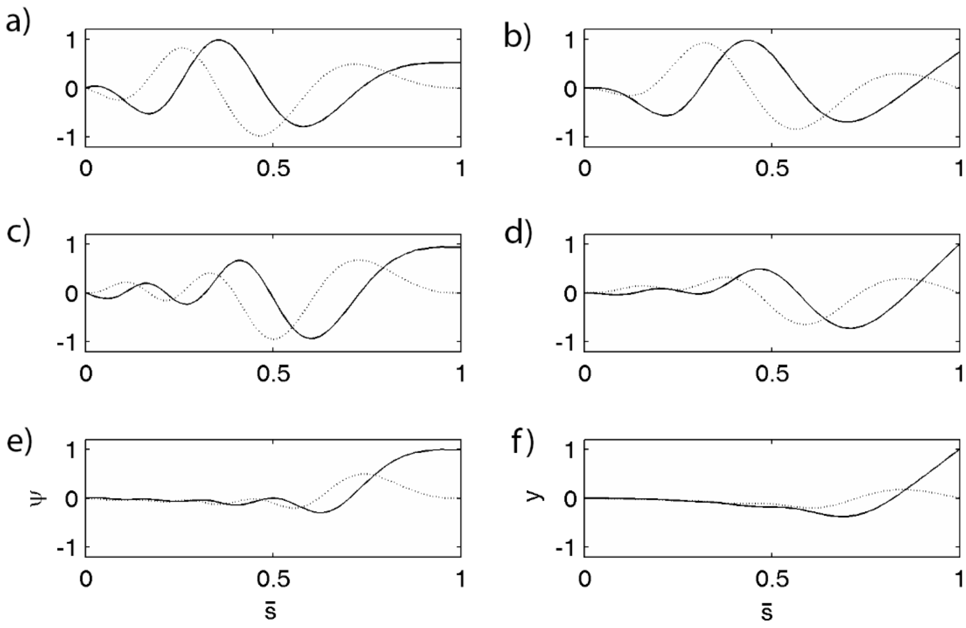

Figure 6.9 – Unstable modes of the GC model
Solutions to Equation (6.31) with parameter values in Table 6.6. (Left) The mode shape expressed in terms of tangent angle, $\tilde{\psi}(\bar{s})$. (Right) The mode shape expressed in terms of displacement, $\tilde{y}(\bar{s})$. The real (solid line) and imaginary (dashed line) part of each mode is shown. Unstable modes correspond to eigenvalues $\sigma = \alpha + i\omega$: (a-b) $\alpha = 38.5$/s, $\omega/2\pi$ =43.2 Hz. (c-d) $\alpha = 7.75$/s, $\omega/2\pi$ =32.6 Hz. (e-f) $\alpha = 1.20$/s, $\omega/2\pi$ =20.3 Hz.

6.6 Large Amplitude, Nonlinear Flagella Oscillations

To explore large-amplitude nonlinear behavior of the model, direct numerical simulations (time-marching) of the complete system of flagellum equations were performed in COMSOL as described above. Equations (4.23), (4.24), and (4.29) with fixed-free boundary conditions, together with the inter-doublet separation Equations (6.13) and (6.14) and dynein activity Equations (6.16) - (6.21), were incorporated in the model. Simulations were started from an initial straight configuration. Bending is initiated by asymmetry in the baseline probabilities of attachment [84].

For a wide range of parameter values the system exhibited large-amplitude oscillations (Figure 6.10). Solutions are characterized by proximal-distal propagation of dynein activity, sustained by the local positive feedback between dynein activity and inter-doublet separation. As predicted by Lindemann [79], [80], [82], [114], when the curvature and doublet tension become large enough, the global transverse force $(S\frac{\partial\psi}{\partial s})$ promotes doublet separation at the proximal end of the active side. This leads to switching of dynein activity and reversal of the direction of bending. For reasonable parameter values (Table 6.6; Figure 6.10) the frequency, amplitude, and waveform resemble those of *Chlamydomonas* in forward swimming (Figure 6.10).

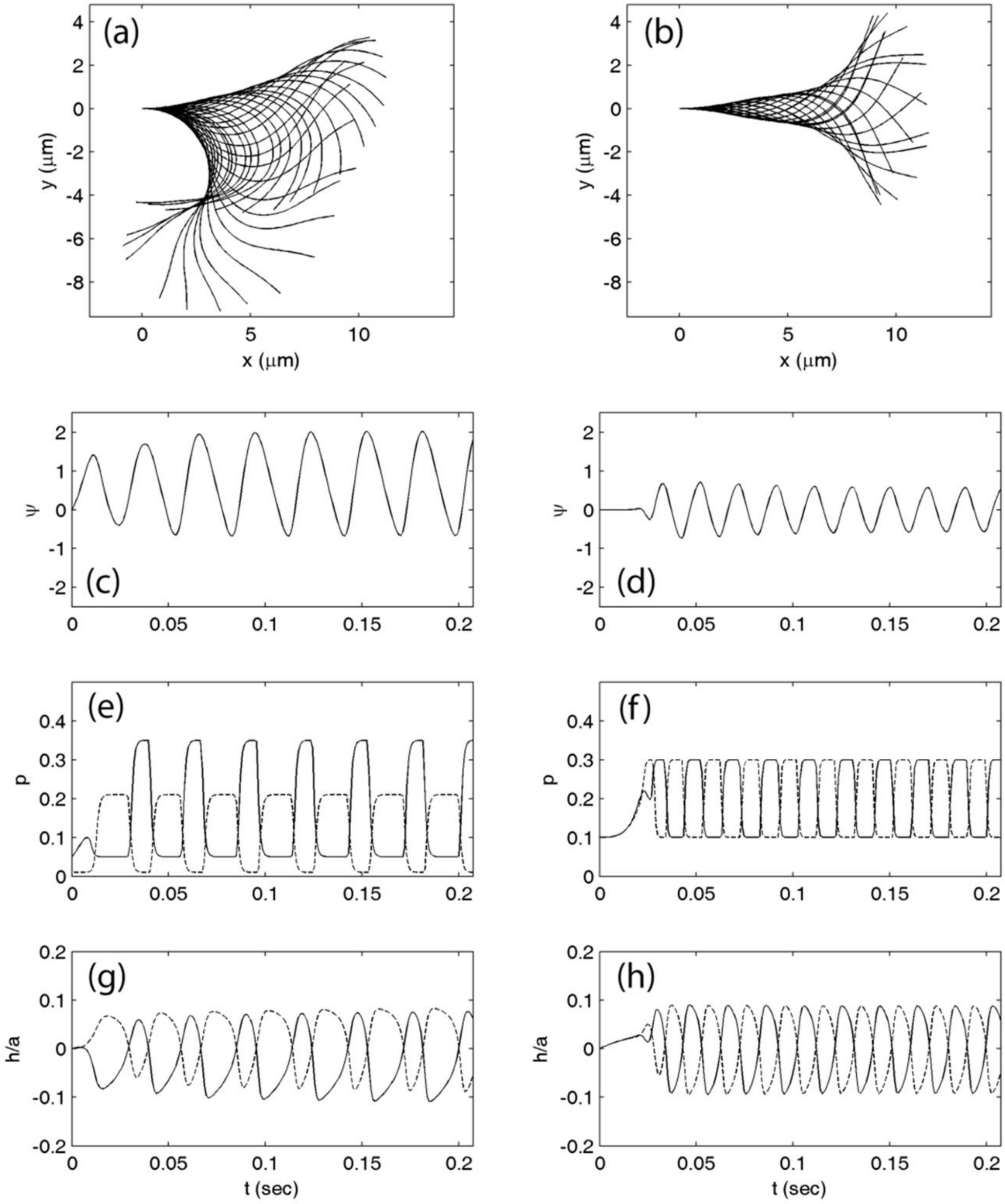

Figure 6.10 – GC waveforms of *Chlamydomonas* flagella from time-marching simulation (a) Asymmetric waveform with baseline probabilities of dynein attachment $p_{0P} = 0.05$ and $p_{0R} = 0.01$. (b) Symmetric waveform with baseline probabilities of dynein attachment $p_{0P} = p_{0R} = 0.10$. Panels (c - h) show corresponding time series of tangent angle, attachment probability and deflection at $s = L/2$. Panels (c, e, g) correspond to the waveform in panel (a). Panels (d, f, h) correspond to the waveform in panel (b). Parameters values are in Table 6.6 except as noted: L=12 μm; EI = 500 pN- μm^2; a= 0.200 μm; C_N=0.0025 pN-s/ μm^2.

Nonlinear simulations of the GC model with parameters as in the SC model (Case 1, Figure 5.5, Case 2, Figure 5.9) were also performed (Figure 6.11). Again, Fourier analysis shows the relative contribution of the fundamental mode to simulations (Table 6.7).

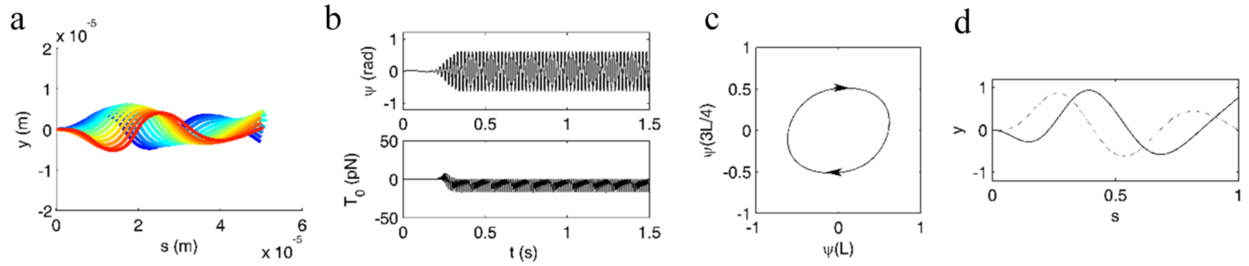

Figure 6.11 – Nonlinear simulation of geometric clutch model
Nonlinear GC model simulation [84], with parameters in Table 6.6 for comparison to sliding-controlled model; (a) Successive snapshots of the flagellar waveform from time-marching simulations; color shows time increasing from blue (early) to red (later); (b) Time series of angle at tip $\psi(s = L)$ (top) and tension at base $T_0(s = 0)$ (bottom; $T_0 < 0$ is propulsive); (c) Plot of $\psi(3L/4)$ vs $\psi(L)$ (clockwise loop = anterograde propagation; counter-clockwise=retrograde); (d) Fundamental mode shape y from Fourier analysis of simulation.

Table 6.7 – Comparison of GC fundamental modes from simulation to the linearized system
Parameters in Table 6.6

Model	**Simulation: Fundamental Frequency (Hz)**	**Simulation: Relative Amplitude of Fundamental Mode**	**Eigenanalysis: Frequencies of Unstable Modes (Hz)**	**Correlation Coefficients: Simulation to Eigenanalysis**
Geometric clutch	46.2	0.948	43.2 32.6 20.3	0.971 0.804 0.430

6.7 Discussion

Partial differential equations (PDEs) corresponding to a continuum version of the GC hypothesis of flagella motion were derived and analyzed. The GC hypothesis has been supported previously by a discrete computer model [79], [80], [82].The solutions to the equations derived here exhibit characteristic features of *Chlamydomonas* flagella: (1) propagation of dynein activity after a supra-threshold stimulus; (2) instability and emergence of small-amplitude, symmetric oscillations under some conditions; (3) the occurrence of large-amplitude, asymmetric oscillations under other conditions.

The PDEs of the GC model were derived from a simplified but rigorous mechanical analysis of doublet pairs on opposite sides of the flagellum. The effects of dynein activity on inter-doublet separation, both directly and indirectly through the effects of accumulated tension and curvature, are included. In turn, dynein activity is modulated by the distance between doublets.

This model includes both local positive feedback, as dynein activity pulls doublets together and increases the likelihood of attachment, and global negative feedback, in which accumulated tension difference and increasing curvature tend to pull the doublets apart. This negative feedback is greater proximally than distally, favoring proximal to distal propagation. Notably, when the baseline probability of attachment is symmetric and relatively large, small-amplitude oscillations arise via a classical dynamic instability. Higher levels of baseline dynein activity increase the steady-state difference in tension in the doublets, which amplifies the de-stabilizing effects of curvature feedback.

Our analysis provides theoretical justification for the GC hypothesis. The equations of inter-doublet separation reduce to a form of the extended Fisher-Kolmorogov (EFK) equations [110], [115], [116], an excitable system known to exhibit propagating wavefronts. This system is closely related to classical reaction-diffusion models [115]. Direct simulation of the original equations of inter-doublet separation (Equations (6.19) and (6.25)) or a simplified excitable model (Equation (6.31)) led to patterns of dynein activity that propagated from the location of a supra-threshold stimulus. Propagation speed depends on elastic and viscous properties of the flagellum, parameters that describe the effects of inter-doublet spacing on cross-bridge formation, and external viscosity.

The emergence of oscillations via dynamic instability is confirmed in a linearized version of the system of equations. The modes and frequencies predicted by this linearized analysis correspond to the small-amplitude solutions of the full nonlinear model under certain conditions. These modes resemble the symmetric motion of *Chlamydomonas* flagella during backward swimming [117]. Time-marching simulations of the full GC model with unequal parameter values governing dynein activity on the P and R sides lead to large-amplitude, asymmetric oscillations similar to those exhibited by *Chlamydomonas* in forward swimming [85], [86], [117] (Figure 6.10). In the absence of active dynein forces, these equations predict the behavior of an elastic beam in viscous fluid and the flagellum returns asymptotically to its straight position. The GC model combines a physically-intuitive mechanism with predicted behavior that resembles observed waveforms. Based on the results of both eigenanalysis and simulation, the data presented in this chapter demonstrate the GC model can produce waveforms with anterograde bend propagation, bend switching at the base, and asymmetry similar to those observed in beating *Chlamydomonas* flagella. These results suggest axonemal dyneins are regulated mostly by inter-doublet separation, not local doublet sliding.

Chapter 7

Discussion and Future Work

This thesis describes experimental measurements of the *Chlamydomonas reinhardtii* flagellar waveform, as well as mathematical modeling and analysis of the flagellum. Flagellar beating has been partially characterized in previous papers[72], [92], [100] but comprehensive, quantitative experimental data has remained elusive. The experimental approach used here is based on a fast, partially automated method for quantifying *Chlamydomonas* waveforms. Solutions to mathematical models of the flagellum were found by both eigenvalue analysis and by time-marching simulation. This chapter summarizes the key findings, examines their significance and discusses possible future work.

7.1 Summary

The *Chlamydomonas* flagellum is an excellent tool for understanding the mechanics and response of axonemes. We find that flagella respond to mechanical loading by primarily varying either beat frequency or waveform. We confirm previous studies [13], [89], [93], [118] showing outer dynein arms are important for maintaining beat frequency. This becomes even more apparent at high viscosities. We observe a reduction in beat width in axonemes lacking inner dynein arm I1/f, suggesting this protein is important for maintenance of a complete power stroke and overall spread of the flagellar beat. The analysis methods presented here suggest beat frequency, beats per revolution, stroke width, curvatures, bend propagation speeds, and stroke completion are useful parameters for characterizing function of a flagellum.

Modeling the flagellum as a nonlinear slender beam in viscous fluid allows derivation of continuum equations of beam mechanics. The solution method proposed by Riedel-Kruse [75] formalizes a mechanism of sliding filament control of dynein regulation, but ignores possible unstable modes that turn out to be important. Formulation of the geometric clutch as a continuum model provides a mathematical basis for an intuitive switching mechanism at the base of the flagellum and displays anterograde bend propagations similar to those observed in *Chlamydomonas* flagella. Analysis of these models suggests curvature and tension feedback are important regulators of dynein activity in the axoneme.

7.1.1 Key Findings and Results

- **Experiment:** Waveform analysis of uniflagellate *Chlamydomonas* cells in regular and high viscosity media shows that the axoneme responds differently to mechanical loading, depending on which motor proteins are present.
    - Outer dynein arms are important for maintaining beat frequency at all viscosities.
    - Flagella generate maximum power at low viscosities, suggesting they are tuned to beat optimally in regular media. Cells lacking inner dynein arm I1/f and outer dynein arms show very little power generation compared to wild-type flagella.
    - The fast flagellar beating rate of *ida1* mutants, particularly at high viscosities, suggests I1/f may actually inhibit bending at high viscosities.
    - Reduction in *ida1* power stroke completion and increase in *oda2* recovery stroke completion suggests that timing of bend initiation and completion is more

important in determining the waveform than minimum or maximum curvature values (bend magnitudes).
    - Significant increase in curvature values only in wild-type axonemes at high viscosities suggests all dynein motors must be present in order to overcome additional resistance to bending.
- **Theory:** Analysis and simulation of sliding controlled (SC) and geometric clutch (GC) models has provided useful insight into their ability to explain flagella motion
    - The analysis of the sliding-controlled mechanism of dynein regulation, as formulated by Riedel-Kruse, et al., does not capture all possible modes of the linearized equations of the beam in viscous media. The existence of retrograde, unstable modes found in this study weakens the argument for this model.
    - Complete nonlinear simulation of a beam with sliding-controlled dynein regulation confirms instability and retrograde (tip-to-base) propagation of bends.
    - A continuum model of the geometric clutch dynein control mechanism shows anterograde bend propagation and robust switching between bends at the base of the flagellum, similar to observed *Chlamydomonas* waveforms.
    - Inter-doublet tension and curvature may be key determinants of flagellar switching.

7.1.2 Significance

Quantitative waveform analysis methods can be used to analyze the flagellar beat and compare changes in flagellum structure and response to conditions. Here we show flagellar response to mechanical loading, including beat frequency reduction and mutation-specific parameter changes. Increasing waveform contrast through tracing allows more accurate and efficient fitting algorithms, at the expense of input time. The automated, quantitative, analysis of previously qualitative information provides valuable additional insight.

Formulation of continuum models of the flagellum as a beam allows comprehensive analysis of the system not possible with other discrete methods. Analysis of the sliding-controlled mechanism of dynein regulation shows this model is unable to describe the autonomous anterograde propagation of bends found in axonemes. The geometric clutch, however, is able to recapitulate these behaviors in a system that presents a simple mechanism for curvature and inter-doublet tension feedback. The analysis presented here suggests the geometric clutch is a more plausible model of dynein regulation, although some elements of sliding control may still be useful in a comprehensive model of flagellar motion.

7.2 Limitations

7.2.1 Cell Experiments

All cells were assumed to be periodically beating, however periodicity was difficult to determine at very low beat frequencies and rotation rates. Occasionally non-asymmetric beat patterns were observed (transient beating and 'unsticking' quick motions). While these were avoided in all analyzed recordings, there is a possibility that recorded cells were actually performing non-periodic oscillations. A photosynthetic organism, the *Chlamydomonas* flagellum has at least two modes of beating: (1) asymmetric, propulsive beats (examined and considered here), and (2) symmetric, 'backwards' beats to reorient or reverse the direction of cell body motion ([37], [119]). Recordings analyzed here were presumed to avoid any transient or symmetric behavior, despite observations of symmetric beating and waveform alterations in sample volumes, particularly at high viscosities.

Cells were recorded an average of 48 hours after dilution, however exact timing was varied based on observations of moving cells. Cultures with minimal rotating cells were either re-diluted or left to grow for an additional amount of time, which may have slightly altered results.

Finally, every effort was made to reduce bias in tracing and analysis, however the manual tracing of each flagellum frame presents an opportunity for error. This work has been a valuable teaching experience in optimizing tasks for humans and computers. Computers are great at sorting and storing large volumes of data, but are poor at recognizing patterns (such as flagellar location in subsequent frames). Humans can readily detect patterns and identify flagellum location in noisy images, but struggle to identify changes in curvature values and periodicity.

7.2.2 Modeling Assumptions

Many theories of dynein regulation have been proposed, however here we only investigate two basic systems: force regulation by sliding displacement of doublets and force regulation by transverse force between doublets. Both models were based on simplified systems of two doublet pairs. In reality, the axoneme has pseudo-symmetry of the nine doublets, along with a central pair that remains perpendicular to the bend plane [120], [121].

The models of dynein regulation analyzed here only consider a general shear force and assumed shear stiffness, unspecified by individual axonemal components. This approach certainly lends insight to force production, but doesn't specify actions of individual motor proteins or even general classes, such as inner vs outer dynein arms.

Finally, the axoneme is a complex structure not only circumferentially but also longitudinally (structural variations also exist within specific species examined). While we have considered the flagellum as a continuous, homogeneous beam, the composition of the axoneme actually varies over its length [122]. The current models do not incorporate any variation in stiffness or composition along the length of the flagellum.

7.3 Future Work

7.3.1 Non-Periodic Oscillations

Quantification of non-periodic processes remains a promising area of study. With much higher time-resolution imaging systems a dense sampling of behavior will allow investigation of symmetric beating and perhaps the transitions from symmetric to asymmetric beating modes.

7.3.2 Model Validation

Mathematical models of flagellar bending have yet to be examined with respect to higher loading conditions. The experimental and computational work associated with this thesis provides a database for comparison between simulated and observed flagellar beats. Consideration of specific dynein components and identified force-velocity curves may be incorporated into a more complex model in an attempt to understand the relative contributions of individual dynein motors.

7.3.3 Clinical Diagnostics

On a broader scale, this research is focused on trying to understand flagellar beating but may also aid the development of fast, automated, clinical diagnostic tools.

The extension of quantitative waveform analysis to human cilia has been a subject of continued research. Key limitations are the 3-dimensional nature of the ciliary beat and difficulty in maintaining culture conditions conducive to physiologic beating. Of the tracheal epithelia analyzed so far, cilia display much more heterogeneous beat patterns.

7.3.4 Microfluidics

Understanding Stokes flow mechanics may provide useful feedback for design of microfluidics systems. It is feasible that the active biological control of dynein motors could have applications beyond *Chlamydomonas*. It is likely that the observed automatic switching and bend propagation is tuned to the length scale of these organelles.

7.3.4 Outlook

The investigation of flagellar beating in response to high mechanical loading and structural variation provides a database of information to validate and critique models of beam oscillation. Understanding how these systems of motors work and how they fail provides insight to the underlying mechanisms of motor protein activity.

References

[1] G. Lefevre and U. B. Jonsson, “Sperm transfer, storage, displacement, and utilization in Drosophila melanogaster.,” *Genetics*, vol. 47, no. December, pp. 1719–1736, 1962.

[2] C. J. Brokaw, “Bend propagation by a sliding filament model for flagella.,” *J. Exp. Biol.*, vol. 55, no. 2, pp. 289–304, Oct. 1971.

[3] P. Satir, “Studies on cilia III: Further studies on the cilium tip and a ‘sliding filament’ model of ciliary motility.,” *J. Cell Biol.*, vol. 39, pp. 77–94, 1968.

[4] K. W. Foster, *Analysis of the ciliary/flagellar beating of Chlamydomonas.*, vol. 91, no. 08. Elsevier Masson SAS, 2009, pp. 173–239.

[5] M. K. Yadav, S. W. Chae, and J. J. Song, “In VitroStreptococcus pneumoniae Biofilm Formation and In Vivo Middle Ear Mucosal Biofilm in a Rat Model of Acute Otitis Induced by S. pneumoniae,” *Clin. Exp. Otorhinolaryngol.*, vol. 5, no. 3, pp. 139–144, 2012.

[6] J. R. Davenport and B. K. Yoder, “An incredible decade for the primary cilium: a look at a once-forgotten organelle.,” *Am. J. Physiol. Renal Physiol.*, vol. 289, pp. F1159–F1169, 2005.

[7] S. Nonaka, Y. Tanaka, Y. Okada, S. Takeda, A. Harada, Y. Kanai, M. Kido, and N. Hirokawa, “Randomization of left-right asymmetry due to loss of nodal cilia generating leftward flow of extraembryonic fluid in mice lacking KIF3B motor protein.,” *Cell*, vol. 95, pp. 829–37, Dec. 1998.

[8] F. Lin, T. Hiesberger, K. Cordes, A. M. Sinclair, L. S. B. Goldstein, S. Somlo, and P. Igarashi, “Kidney-specific inactivation of the KIF3A subunit of kinesin-II inhibits renal ciliogenesis and produces polycystic kidney disease.,” *Proc. Natl. Acad. Sci. U. S. A.*, vol. 100, no. 9, pp. 5286–5291, 2003.

[9] R. a. Lyons, E. Saridogan, and O. Djahanbakhch, “The reproductive significance of human Fallopian tube cilia,” *Hum. Reprod. Update*, vol. 12, no. 4, pp. 363–372, 2006.

[10] D. J. Smith, E. a. Gaffney, H. Gadelha, N. Kapur, and J. C. Kirkman-Brown, “Bend propagation in the flagella of migrating human sperm, and Its modulation by viscosity,” *Cell Motil. Cytoskeleton*, vol. 66, no. December 2008, pp. 220–236, 2009.

[11] T. Ferkol, “Airway Epithelium SEM.” Washington University in St. Louis.

[12] M. Fliegauf, T. Benzing, and H. Omran, “When cilia go bad: cilia defects and ciliopathies.,” *Nat. Rev. Mol. Cell Biol.*, vol. 8, no. 11, pp. 880–93, Nov. 2007.

[13] G. J. Pazour, N. Agrin, B. L. Walker, and G. B. Witman, “Identification of predicted human outer dynein arm genes: candidates for primary ciliary dyskinesia genes.,” *J. Med. Genet.*, vol. 43, pp. 62–73, Jan. 2006.

[14] S. T. Christensen, L. B. Pedersen, L. Schneider, and P. Satir, “Sensory cilia and integration of signal transduction in human health and disease.,” *Traffic*, vol. 8, no. 2, pp. 97–109, Feb. 2007.

[15] M. Adams, U. M. Smith, C. V Logan, and C. a Johnson, “Recent advances in the molecular pathology, cell biology and genetics of ciliopathies.,” *J. Med. Genet.*, vol. 45, no. 5, pp. 257–67, May 2008.

[16] W. F. Marshall, “The cell biological basis of ciliary disease.,” *J. Cell Biol.*, vol. 180, no. 1, pp. 17–21, Jan. 2008.

[17] L. Zhu, J. W. Belmont, and S. M. Ware, “Genetics of human heterotaxias.,” *Eur. J. Hum. Genet.*, vol. 14, no. August 2005, pp. 17–25, 2006.

[18] N. Hornef, H. Olbrich, J. Horvath, M. a Zariwala, M. Fliegauf, N. T. Loges, J. Wildhaber, P. G. Noone, M. Kennedy, S. E. Antonarakis, J.-L. Blouin, L. Bartoloni, T. Nüsslein, P. Ahrens, M. Griese, H. Kuhl, R. Sudbrak, M. R. Knowles, R. Reinhardt, and H. Omran, “DNAH5 mutations are a common cause of primary ciliary dyskinesia with outer dynein arm defects.,” *Am. J. Respir. Crit. Care Med.*, vol. 174, no. 2, pp. 120–6, Jul. 2006.

[19] L. Vincensini, T. Blisnick, and P. Bastin, “1001 model organisms to study cilia and flagella biology,” *Biol. Aujourdhui.*, vol. 205, pp. 5–28, 2011.

[20] B. Afzelius, “Genetical and ultrastructural aspects of the immotile-cilia syndrome.,” *Am. J. Hum. Genet.*, vol. 33, pp. 852–864, 1981.

[21] J. L. Blouin, M. Meeks, U. Radhakrishna, a Sainsbury, C. Gehring, G. D. Saïl, L. Bartoloni, V. Dombi, a O’Rawe, a Walne, E. Chung, B. a Afzelius, M. Armengot, M. Jorissen, D. V Schidlow, L. van Maldergem, H. Walt, R. M. Gardiner, D. Probst, P. a Guerne, C. D. Delozier-Blanchet, and S. E. Antonarakis, “Primary ciliary dyskinesia: a genome-wide linkage analysis reveals extensive locus heterogeneity.,” *Eur. J. Hum. Genet.*, vol. 8, no. June 1999, pp. 109–118, 2000.

[22] D. Antony, A. Becker-Heck, M. a Zariwala, M. Schmidts, A. Onoufriadis, M. Forouhan, R. Wilson, T. Taylor-Cox, A. Dewar, C. Jackson, P. Goggin, N. T. Loges, H. Olbrich, M. Jaspers, M. Jorissen, M. W. Leigh, W. E. Wolf, M. L. A. Daniels, P. G. Noone, T. W. Ferkol, S. D. Sagel, M. Rosenfeld, A. Rutman, A. Dixit, C. O’Callaghan, J. S. Lucas, C. Hogg, P. J. Scambler, R. D. Emes, E. M. K. Chung, A. Shoemark, M. R. Knowles, H. Omran, and H. M. Mitchison, “Mutations in CCDC39 and CCDC40 are the major cause

of primary ciliary dyskinesia with axonemal disorganization and absent inner dynein arms.," *Hum. Mutat.*, vol. 34, no. 3, pp. 462–72, Mar. 2013.

[23] M. P. Kennedy, H. Omran, M. W. Leigh, S. Dell, L. Morgan, P. L. Molina, B. V Robinson, S. L. Minnix, H. Olbrich, T. Severin, P. Ahrens, L. Lange, H. N. Morillas, P. G. Noone, M. a Zariwala, and M. R. Knowles, "Congenital heart disease and other heterotaxic defects in a large cohort of patients with primary ciliary dyskinesia.," *Circulation*, vol. 115, pp. 2814–21, Jun. 2007.

[24] K. Storm van's Gravesande and H. Omran, "Primary ciliary dyskinesia: clinical presentation, diagnosis and genetics.," *Ann. Med.*, vol. 37, pp. 439–49, Jan. 2005.

[25] G. Pennarun, E. Escudier, C. Chapelin, a M. Bridoux, V. Cacheux, G. Roger, a Clément, M. Goossens, S. Amselem, and B. Duriez, "Loss-of-function mutations in a human gene related to Chlamydomonas reinhardtii dynein IC78 result in primary ciliary dyskinesia.," *Am. J. Hum. Genet.*, vol. 65, pp. 1508–1519, 1999.

[26] L. Lee, "Mechanisms of mammalian ciliary motility: Insights from primary ciliary dyskinesia genetics.," *Gene*, vol. 473, no. 2, pp. 57–66, Mar. 2011.

[27] C. D. Silflow and P. A. Lefebvre, "Assembly and Motility of Eukaryotic Cilia and Flagella . Lessons from Chlamydomonas reinhardtii," *Plant Physiol.*, vol. 127, no. December, pp. 1500–1507, 2001.

[28] E. Kott, P. Duquesnoy, B. Copin, M. Legendre, F. Dastot-Le Moal, G. Montantin, L. Jeanson, A. Tamalet, J. F. Papon, J. P. Siffroi, N. Rives, V. Mitchell, J. De Blic, A. Coste, A. Clement, D. Escalier, A. Touré, E. Escudier, and S. Amselem, "Loss-of-function mutations in LRRC6, a gene essential for proper axonemal assembly of inner and outer dynein arms, cause primary ciliary dyskinesia," *Am. J. Hum. Genet.*, vol. 91, pp. 958–964, 2012.

[29] M. Wei, P. Sivadas, H. A. Owen, D. R. Mitchell, and P. Yang, "Chlamydomonas mutants display reversible deficiencies in flagellar beating and axonemal assembly," *Cytoskeleton*, vol. 67, no. 2, pp. 71–80, 2010.

[30] L. El Zein, H. Omran, and P. Bouvagnet, "Lateralization defects and ciliary dyskinesia: Lessons from algae," *Trends Genet.*, vol. 19, no. 3, pp. 162–167, 2003.

[31] L. C. Keller, E. P. Romijn, I. Zamora, J. R. Yates, and W. F. Marshall, "Proteomic analysis of isolated chlamydomonas centrioles reveals orthologs of ciliary-disease genes.," *Curr. Biol.*, vol. 15, no. 12, pp. 1090–8, Jun. 2005.

[32] C. Cibert, "A cascade of biochemical events creates emergence," *Biol. Cell*, vol. 96, pp. 677–679, 2004.

[33] H. Sakakibara and K. Oiwa, “Molecular organization and force-generating mechanism of dynein,” *FEBS J.*, vol. 278, pp. 2964–2979, 2011.

[34] G. J. Pazour, “Comparative genomics: Prediction of the ciliary and basal body proteome,” *Curr. Biol.*, vol. 14, pp. 575–577, 2004.

[35] G. J. Pazour and J. L. Rosenbaum, “Intraflagellar transport and cilia-dependent diseases,” *Trends Cell Biol.*, vol. 12, no. 12, pp. 551–555, 2002.

[36] K. I. Wakabayashi, T. Yagi, and R. Kamiya, “Ca2+-dependent waveform conversion in the flagellar axoneme of chlamydomonas mutants lacking the central-pair/radial spoke system,” *Cell Motil. Cytoskeleton*, vol. 38, no. November 1996, pp. 22–28, 1997.

[37] R. a. Segal, B. Huang, Z. Ramanis, and D. J. Luck, “Mutant strains of Chlamydomonas reinhardtii that move backwards only.,” *J. Cell Biol.*, vol. 98, no. June, pp. 2026–2034, 1984.

[38] M. Polin, I. Tuval, K. Drescher, J. P. Gollub, and R. E. Goldstein, “Chlamydomonas swims with two ‘gears’ in a eukaryotic version of run-and-tumble locomotion.,” *Science*, vol. 325, no. 5939, pp. 487–90, Jul. 2009.

[39] D. Bray, *Cell Movements: From Molecules to Motility*. 2001.

[40] D. L. Ringo, “Flagellar Motion and Fine Structure of the Flagellar Apparatus in Chlamydomonas,” *J. Cell Biol.*, vol. 33, pp. 543–571, 1967.

[41] R. Sager and S. Granick, “Nutritional Studies with Chlamydomonas reinhardi,” *Ann. N. Y. Acad. Sci.*, vol. 56, pp. 831–838, 1953.

[42] L. M. DiBella and S. M. King, “Dynein motors of the Chlamydomonas flagellum.,” *Int. Rev. Cytol.*, vol. 210, pp. 227–68, Jan. 2001.

[43] S. S. Merchant, S. E. Prochnik, O. Vallon, E. H. Harris, S. J. Karpowicz, G. B. Witman, A. Terry, A. Salamov, L. K. Fritz-Laylin, L. Maréchal-Drouard, W. F. Marshall, L.-H. Qu, D. R. Nelson, A. a Sanderfoot, M. H. Spalding, V. V Kapitonov, Q. Ren, P. Ferris, E. Lindquist, H. Shapiro, S. M. Lucas, J. Grimwood, J. Schmutz, P. Cardol, H. Cerutti, G. Chanfreau, C.-L. Chen, V. Cognat, M. T. Croft, R. Dent, S. Dutcher, E. Fernández, H. Fukuzawa, D. González-Ballester, D. González-Halphen, A. Hallmann, M. Hanikenne, M. Hippler, W. Inwood, K. Jabbari, M. Kalanon, R. Kuras, P. a Lefebvre, S. D. Lemaire, A. V Lobanov, M. Lohr, A. Manuell, I. Meier, L. Mets, M. Mittag, T. Mittelmeier, J. V Moroney, J. Moseley, C. Napoli, A. M. Nedelcu, K. Niyogi, S. V Novoselov, I. T. Paulsen, G. Pazour, S. Purton, J.-P. Ral, D. M. Riaño-Pachón, W. Riekhof, L. Rymarquis, M. Schroda, D. Stern, J. Umen, R. Willows, N. Wilson, S. L. Zimmer, J. Allmer, J. Balk, K. Bisova, C.-J. Chen, M. Elias, K. Gendler, C. Hauser, M. R. Lamb, H. Ledford, J. C. Long, J. Minagawa, M. D. Page, J. Pan, W. Pootakham, S. Roje, A. Rose, E. Stahlberg, A. M. Terauchi, P. Yang, S. Ball, C. Bowler, C. L. Dieckmann, V. N. Gladyshev, P. Green,

R. Jorgensen, S. Mayfield, B. Mueller-Roeber, S. Rajamani, R. T. Sayre, P. Brokstein, I. Dubchak, D. Goodstein, L. Hornick, Y. W. Huang, J. Jhaveri, Y. Luo, D. Martínez, W. C. A. Ngau, B. Otillar, A. Poliakov, A. Porter, L. Szajkowski, G. Werner, K. Zhou, I. V Grigoriev, D. S. Rokhsar, and A. R. Grossman, "The Chlamydomonas genome reveals the evolution of key animal and plant functions.," *Science*, vol. 318, no. 5848, pp. 245–50, Oct. 2007.

[44] S. K. Dutcher, "Flagellar Assembly in Two Hundred and Fifty Easy-to-Follow Steps," *Trends Genet.*, vol. 11, no. 10, pp. 398–404, 1995.

[45] G. J. Pazour, N. Agrin, J. Leszyk, and G. B. Witman, "Proteomic analysis of a eukaryotic cilium," *J. Cell Biol.*, vol. 170, no. 1, pp. 103–113, 2005.

[46] M. C. Diniz, A. Carolina L. Pacheco, K. M. Farias, and D. M. de Oliveira, "The Eukaryotic Flagellum Makes the Day: Novel and Unforeseen Roles Uncovered After Post-Genomics and Proteomics Data," *Curr. Protein Pept. Sci.*, vol. 13, pp. 524–546, 2012.

[47] I. Gibbons and A. Rowe, "Dynein: A protein with adenosine triphosphatase activity from cilia," *Science (80-.).*, vol. 183, no. May, pp. 139–141, 1965.

[48] A. G. Diamant and A. P. Carter, "Dynein Family Classification," in *Biophysics Encyclopedia*, 2013, pp. 552–572.

[49] M. R. Villarreal, "Eukaryotic Cilium Diagram." p. Public Domain Image.

[50] S. K. Dutcher, "The tubulin fraternity: Alpha to eta," *Curr. Opin. Cell Biol.*, vol. 13, pp. 49–54, 2001.

[51] P. G. Czarnecki and J. V. Shah, "The ciliary transition zone: from morphology and molecules to medicine," *Trends Cell Biol.*, vol. 22, no. 4, pp. 201–210, 2012.

[52] D. Nicastro, C. Schwartz, J. Pierson, R. Gaudette, M. E. Porter, and J. R. McIntosh, "The molecular architecture of axonemes revealed by cryoelectron tomography.," *Science*, vol. 313, pp. 944–948, 2006.

[53] K. E. Summers and I. R. Gibbons, "Adenosine Triphosphate-Induced Sliding of Tubules in Trypsin-Treated Flagella of Sea-Urchin Sperm," *Proc. Natl. Acad. Sci.*, vol. 68, no. 12, pp. 3092–3096, Dec. 1971.

[54] G. B. Witman, J. Plummer, and G. Sander, "Chlamydomonas flagellar mutants lacking radial spokes and central tubules. Structure, composition, and function of specific axonemal components.," *J. Cell Biol.*, vol. 76, no. 3, pp. 729–47, Mar. 1978.

[55] C. B. Lindemann, “Structural-functional relationships of the dynein, spokes, and central-pair projections predicted from an analysis of the forces acting within a flagellum.,” *Biophys. J.*, vol. 84, no. 6, pp. 4115–26, Jun. 2003.

[56] P. Yang, D. R. Diener, J. L. Rosenbaum, and W. S. Sale, “Localization of calmodulin and dynein light chain LC8 in flagellar radial spokes.,” *J. Cell Biol.*, vol. 153, no. 6, pp. 1315–26, Jun. 2001.

[57] M. J. Wargo and E. F. Smith, “Asymmetry of the central apparatus defines the location of active microtubule sliding in Chlamydomonas flagella.,” *Proc. Natl. Acad. Sci. U. S. A.*, vol. 100, no. 1, pp. 137–42, Jan. 2003.

[58] T. Oda, H. Yanagisawa, T. Yagi, and M. Kikkawa, “Mechanosignaling between central apparatus and radial spokes controls axonemal dynein activity,” *J. Cell Biol.*, vol. 204, no. 5, pp. 807–819, 2014.

[59] C. Cibert, “Entropy and information in flagellar axoneme cybernetics: A radial spokes integrative function,” *Cell Motil. Cytoskeleton*, vol. 54, no. October 2002, pp. 296–316, 2003.

[60] T. Heuser, M. Raytchev, J. Krell, M. E. Porter, and D. Nicastro, “The dynein regulatory complex is the nexin link and a major regulatory node in cilia and flagella.,” *J. Cell Biol.*, vol. 187, no. 6, pp. 921–33, Dec. 2009.

[61] T. Yagi, K. Uematsu, Z. Liu, and R. Kamiya, “Identification of dyneins that localize exclusively to the proximal portion of Chlamydomonas flagella.,” *J. Cell Sci.*, vol. 122, pp. 1306–1314, 2009.

[62] G. Piperno and Z. Ramanis, “The Proximal Portion of Chlamydomonas Flaglla Contains a Distinct Set of Inner Dynein Arms,” vol. 112, no. 4, pp. 701–709, 1991.

[63] S. a Burgess, M. L. Walker, H. Sakakibara, P. J. Knight, and K. Oiwa, “Dynein structure and power stroke.,” *Nature*, vol. 421, no. 6924, pp. 715–8, Feb. 2003.

[64] R. Kamiya and G. B. Witman, “Submicromolar levels of calcium control the balance of beating between the two flagella in demembranated models of Chlamydomonas,” *J. Cell Biol.*, vol. 98, pp. 97–107, 1984.

[65] S. Camalet, F. Jülicher, and J. Prost, “Self-Organized Beating and Swimming of Internally Driven Filaments,” *Phys. Rev. Lett.*, vol. 82, no. 7, pp. 1590–1593, Feb. 1999.

[66] T. Kubo, H. A. Yanagisawa, T. Yagi, M. Hirono, and R. Kamiya, “Tubulin Polyglutamylation Regulates Axonemal Motility by Modulating Activities of Inner-Arm Dyneins,” *Curr. Biol.*, vol. 20, no. 5, pp. 441–445, 2010.

[67] S. Suryavanshi, B. Eddé, L. a. Fox, S. Guerrero, R. Hard, T. Hennessey, A. Kabi, D. Malison, D. Pennock, W. S. Sale, D. Wloga, and J. Gaertig, “Tubulin Glutamylation Regulates Ciliary Motility by Altering Inner Dynein Arm Activity,” *Curr. Biol.*, vol. 20, no. 5, pp. 435–440, 2010.

[68] C. J. Brokaw, “Control of flagellar bending: a new agenda based on dynein diversity.,” *Cell Motil. Cytoskeleton*, vol. 28, pp. 199–204, 1994.

[69] C. J. Brokaw, “Computer Simulation of Flagellar Movement : VII . Conventional But Functionally Different Cross-Bridge Models for Inner and Outer Arm Dyneins Can Explain the Effects of Outer Arm Dynein Removal,” vol. 148, no. November 1998, pp. 134–148, 1999.

[70] S. Toba, L. a Fox, H. Sakakibara, M. E. Porter, K. Oiwa, and W. S. Sale, “Distinct roles of 1alpha and 1beta heavy chains of the inner arm dynein I1 of Chlamydomonas flagella.,” *Mol. Biol. Cell*, vol. 22, pp. 342–353, 2011.

[71] K. Machin, “Wave propagation along flagella,” *J. Exp. Biol.*, vol. 35, pp. 796–806, 1958.

[72] C. J. Brokaw and R. Kamiya, “Bending patterns of Chlamydomonas flagella: IV. Mutants with defects in inner and outer dynein arms indicate differences in dynein arm function.,” *Cell Motil. Cytoskeleton*, vol. 8, no. 1, pp. 68–75, Jan. 1987.

[73] M. E. Holwill and P. Satir, “A physical model of microtubule sliding in ciliary axonemes.,” *Biophys. J.*, vol. 58, no. 4, pp. 905–17, Oct. 1990.

[74] R. Rikmenspoel and W. G. Rudd, “The contractile mechanism in cilia.,” *Biophys. J.*, vol. 13, no. 9, pp. 955–93, Sep. 1973.

[75] I. H. Riedel-Kruse, A. Hilfinger, J. Howard, and F. Jülicher, “How molecular motors shape the flagellar beat.,” *HFSP J.*, vol. 1, no. 3, pp. 192–208, Sep. 2007.

[76] S. Camalet and F. Julicher, “Generic aspects of axonemal beating,” *New J. Phys.*, vol. 2, pp. 24.1–24.33, 2000.

[77] A. Hilfinger, A. Chattopadhyay, and F. Jülicher, “Nonlinear dynamics of cilia and flagella,” *Phys. Rev. E*, vol. 79, no. 5, pp. 051918:1–8, May 2009.

[78] M. Hines and J. J. Blum, “Bend Propagation in Flagella. I. Derivation of Equations of Motion and Their Simulation,” *Biophys. J.*, vol. 3, pp. 41–57, 1978.

[79] C. B. Lindemann, “A ‘Geometric Clutch’ Hypothesis to Explain Oscillations of the Axoneme of Cilia and Flagella,” *J. Theor. Biol.*, vol. 168, pp. 175–189, 1994.

[80] C. B. Lindemann, “A model of flagellar and ciliary functioning which uses the forces transverse to the axoneme as the regulator of dynein activation.,” *Cell Motil. Cytoskeleton*, vol. 29, no. 2, pp. 141–54, Jan. 1994.

[81] C. B. Lindemann and K. S. Kanous, “Views and Reviews ‘ Geometric Clutch ’ Hypothesis of Axonemal Function : Key Issues and Testable Predictions,” *Cell Motil. Cytoskeleton*, vol. 31, pp. 1–8, 1995.

[82] C. B. Lindemann, “Geometric Clutch model version 3: the role of the inner and outer arm dyneins in the ciliary beat.,” *Cell Motil. Cytoskeleton*, vol. 52, no. 4, pp. 242–54, Aug. 2002.

[83] C. B. Lindemann, “The geometric clutch as a working hypothesis for future research on cilia and flagella.,” *Ann. N. Y. Acad. Sci.*, vol. 1101, pp. 477–93, Apr. 2007.

[84] P. V Bayly and K. S. Wilson, “Equations of Interdoublet Separation during Flagella Motion Reveal Mechanisms of Wave Propagation and Instability.,” *Biophys. J.*, vol. 107, no. 7, pp. 1756–72, Oct. 2014.

[85] P. V Bayly, B. L. Lewis, P. S. Kemp, R. B. Pless, and S. K. Dutcher, “Efficient spatiotemporal analysis of the flagellar waveform of Chlamydomonas reinhardtii.,” *Cytoskeleton*, vol. 67, no. 1, pp. 56–69, Jan. 2010.

[86] P. V Bayly, B. L. Lewis, E. C. Ranz, R. J. Okamoto, R. B. Pless, and S. K. Dutcher, “Propulsive forces on the flagellum during locomotion of Chlamydomonas reinhardtii.,” *Biophys. J.*, vol. 100, no. 11, pp. 2716–25, Jun. 2011.

[87] B. Huang, Z. Ramanis, S. K. Dutcher, and D. J. L. Luck, “Uniflagellar mutants of Chlamydomonas: evidence for the role of basal bodies in transmission of positional information,” *Cell*, vol. 29, pp. 745–53, Jul. 1982.

[88] S. K. Dutcher, “Mating and tetrad analysis in Chlamydomonas reinhardtii,” *Methods Cell Biol.*, vol. 47, pp. 531–540, 1995.

[89] R. Kamiya, E. Kurimoto, and E. Muto, “Two Types of Chlamydomonas Flagellar Mutants Missing Different Components of Inner-Arm Dynein,” *J. Cell Biol.*, vol. 112, no. 3, pp. 441–447, 1991.

[90] O. Kagami and R. Kamiya, “Translocation and rotation of microtubules caused by multiple species of Chlamydomonas inner-arm dynein,” *Proteins*, vol. 664, pp. 653–664, 1992.

[91] S. J. King and S. K. Dutcher, “Phosphoregulation of an Inner Dynein Arm Complex in Chlamydomonas renhardtii is Altered in Phototactic Mutant Strains,” *J. Cell Biol.*, vol. 136, no. 1, pp. 177–191, 1997.

[92] T. Yagi, I. Minoura, A. Fujiwara, R. Saito, T. Yasunaga, M. Hirono, and R. Kamiya, “An axonemal dynein particularly important for flagellar movement at high viscosity; Implications from a new Chlamydomonas mutant deficient in the dynein heavy chain gene DHC9.,” *J. Biol. Chem.*, vol. 280, no. 50, pp. 41412–20, Dec. 2005.

[93] R. Kamiya, “Mutations at Twelve Independent Loci Result in Absence of Outer Dynein Arms in Chflamydomonas reinhardtii,” *J. Cell Biol.*, vol. 107, no. 6, pp. 2253–2258, 1988.

[94] F. G. I. Lux and S. K. Dutcher, “Genetic Interactions at the FLA10 Locus: Suppressors and Synthetic Phenotypes That Affect the Cell Cycle and Flagellar Function in Chlamydomonas reinhardtii,” *Genetics*, vol. 128, pp. 549–561, 1991.

[95] J. A. Holmes and S. K. Dutcher, “Cellular asymmetry in Chlamydomonas reinhardtii,” *J. Cell Sci.*, vol. 94, pp. 273–85, Oct. 1989.

[96] B. Huang, M. R. Rifkin, D. J. L. Luck, and V. Kozler, “Temperature-Sensitive Mtations Affecting Flagellar Assembly and Function in Chlamydomonas reinhardtii,” *Cell*, vol. 72, pp. 67–85, 1977.

[97] B. M. Friedrich, I. H. Riedel-Kruse, J. Howard, and F. Jülicher, “High-precision tracking of sperm swimming fine structure provides strong test of resistive force theory.,” *J. Exp. Biol.*, vol. 213, pp. 1226–34, Apr. 2010.

[98] W. S. Rasband, “ImageJ.” U. S. National Institutes of Health, Bethesda, Maryland, USA.

[99] J. B. Tenenbaum, V. de Silva, and J. C. Langford, “A global geometric framework for nonlinear dimensionality reduction.,” *Science*, vol. 290, no. December, pp. 2319–2323, 2000.

[100] I. Minoura and R. Kamiya, “Strikingly Different Propulsive Forces Generated by Diffrent Dynein-Deficient Mutants in Viscous Media,” *Cell Motil. Cytoskeleton*, vol. 31, pp. 130–139, 1995.

[101] S. M. King, “Sensing the mechanical state of the axoneme and integration of Ca 2+ signaling by outer arm dynein,” *Cytoskeleton*, vol. 67, no. April, pp. 207–213, 2010.

[102] M. Wirschell, T. Hendrickson, and W. S. Sale, “Keeping an eye on I1: I1 dynein as a model for flagellar dynein assembly and regulation,” *Cell Motil. Cytoskeleton*, vol. 64, no. 8, pp. 569–79, Aug. 2007.

[103] P. Satir, “Studies on Cilia II. Examination of the Distal Region of the Ciliary Shaft and the Role of the Filaments in Motility,” *J. Cell Biol.*, vol. 26, no. 3, pp. 805–34, 1965.

[104] S. Gueron and N. Liron, “Ciliary motion modeling, and dynamic multicilia interactions.,” *Biophys. J.*, vol. 63, no. 4, pp. 1045–58, Oct. 1992.

[105] L. Meirovitch, *Principles and Techniques of Vibrations*. Prentice Hall, Upper Saddle River, NJ., 1997.

[106] C. J. Brokaw, “Computer simulation of flagellar movement. I. Demonstration of stable bend propagation and bend initiation by the sliding filament model.,” *Biophys. J.*, vol. 12, no. 5, pp. 564–86, May 1972.

[107] H. Gadêlha, E. A. Gaffney, D. J. Smith, and J. C. Kirkman-Brown, “Nonlinear instability in flagellar dynamics : a novel modulation mechanism in sperm migration?,” *J. R. Soc. Interface*, vol. 7, no. 53, pp. 1689–97, 2010.

[108] L. Peletier and W. Troy, “Chaotic Spatial Patterns Described by the Extended Fisher Kolmogorov Equation,” *J. Differ. Equ.*, vol. 129, pp. 458–508, 1996.

[109] C. J. Brokaw, “Thinking about flagellar oscillation.,” *Cell Motil. Cytoskeleton*, vol. 66, no. 8, pp. 425–36, Aug. 2009.

[110] D. Bonheure, “Multitransition kinks and pulses for fourth order equations with a bistable nonlinearity,” *Ann. l’Institut Henri Poincare. Ann. Anal. Non Lineaire*, vol. 21, pp. 319–340, 2003.

[111] J. S. Hyams and G. G. Borisy, “Isolated Flagellar Apparatus of Chlamydomonas: characterization of forward swimming and alteration of waveform and reversal of motion by calcium ions in vitro,” *J. Cell Sci.*, vol. 33, pp. 235–253, 1978.

[112] H. Bannai, M. Yoshimura, K. Takahashi, and C. Shingyoji, “Calcium regulation of microtubule sliding in reactivated sea urchin sperm flagella.,” *J. Cell Sci.*, vol. 113 (Pt 5, pp. 831–9, Mar. 2000.

[113] H. C. Fu, C. W. Wolgemuth, and T. R. Powers, “Beating patterns of filaments in viscoelastic fluids,” *Phys. Rev. E - Stat. Nonlinear, Soft Matter Phys.*, vol. 78, pp. 1–12, 2008.

[114] C. B. Lindemann and K. A. Lesich, “Cytoskeleton Methods and Protocols,” *Business*, vol. 586, pp. 337–353, 2010.

[115] M. E. Akveld and J. Hulshof, “Travelling Wave Solutions of a Fourth-Order Semilinear Diffusion Equation,” *Appl. Math Lett.*, vol. 11, no. 3, pp. 115–120, 1998.

[116] J. B. Van den Berg, J. Hulshof, and R. C. Vandervorst, “Travelling Waves for Fourth Order Parabolic Equations,” *SIAM J. Math. Anal.*, vol. 32, no. 6, pp. 1342–1374, 2001.

[117] C. J. Brokaw and D. J. Luck, “Bending patterns of chlamydomonas flagella I. Wild-type bending patterns.,” *Cell Motil.*, vol. 3, no. 2, pp. 131–50, Jan. 1983.

[118] R. Kamiya and M. Okamoto, “A mutant of Chlamydomonas reinhardtii that lacks the flagellar outer dynein arm but can swim.,” *J. Cell Sci.*, vol. 74, pp. 181–91, Mar. 1985.

[119] K. Yoshimura, Y. Matsuo, and R. Kamiya, “Gravitaxis in Chlamydomonas reinhardtii studied with novel mutants.,” *Plant Cell Physiol.*, vol. 44, no. 10, pp. 1112–8, Oct. 2003.

[120] B. I. Carbajal-González, T. Heuser, X. Fu, J. Lin, B. W. Smith, D. R. Mitchell, and D. Nicastro, “Conserved structural motifs in the central pair complex of eukaryotic flagella.,” *Cytoskeleton (Hoboken).*, vol. 70, no. 2, pp. 101–20, Feb. 2013.

[121] D. R. Mitchell, “Orientation of the central pair complex during flagellar bend formation in Chlamydomonas,” *Cell Motil. Cytoskeleton*, vol. 56, no. May, pp. 120–129, 2003.

[122] H. J. Hoops and G. B. Witman, “Outer doublet heterogeneity reveals structural polarity related to beat direction in Chlamydomonas flagella.,” *J. Cell Biol.*, vol. 97, no. September, pp. 902–908, 1983.

[123] P. V Bayly and K. S. Wilson, “Analysis of unstable modes distinguishes mathematical models of flagellar motion,” *J. R. Soc. Interface*, vol. In Press, no. March, 2015.

Vita

Kate Sarah Wilson

Degrees

PhD, Mechanical Engineering, Washington University in St. Louis, May 2015
MS, Mechanical Engineering, Washington University in St. Louis, May 2013
BS, Biomedical Engineering, Washington University in St. Louis, May 2010

Professional Societies

Biophysical Society
Society of Women Engineers
Biomedical Engineering Society

Journal Publications

Wilson K, Bayly P, Gonzalez O, Dutcher S. Wild-type and mutant flagella of Chlamydomonas reinhardtii respond to high viscosity by decreasing beat frequency or changing waveform . Submitting Apr 2015.

PV Bayly and **KS Wilson**. Identification and Interpretation of Unstable Modes in Mathematical Models of Flagella Motion. Journal of the Royal Society Interface. In Press, March 2015.

PV Bayly and **KS Wilson**. Equations of inter-doublet separation during flagellar motion reveal mechanisms of wave propagation and instability. Biophysical Journal. Oct 2014; 107(7): 1756-72.

Amjad Horani, Steven L Brody, Thomas W Ferkol, David Shoseyov, Mollie G Wasserman, Asaf Ta-shma, **Kate S Wilson**, Philip V Bayly, Israel Amirav, Malena Cohen-Cymberknoh, Susan K Dutcher, Orly Elpeleg, and Eitan Kerem. CCDC65 mutation causes primary ciliary dyskinesia with normal ultrastructure and hyperkinetic cilia. PLoS ONE, July 2013; 8(8):e72299.

Horani A, Druley TE, Zariwala MA, Levinson BT, Van Arendonk LG, Thornton KC, Giacalone JC, Albee AJ, **Wilson KS**, Turner EH, Nickerson DA, Shendure J, Patel AC, Bayly PV, Leigh MW, Knowles, MR, Brody SL, Dutcher SK, Ferkol TW. Whole exome capture and sequencing identifies HEATR2 mutation as a cause of primary ciliary dyskinesia. American Journal of Human Genetics. Oct 2012, 91(4):685-93.

Conference Presentations and Proceedings

Bayly P, **Wilson K**. Equations of Inter-Doublet Separation Explain Wave Propagation and Oscillations in Flagella. Poster presentation, BPS Annual Meeting 2015, Baltimore, MD, February 7-11, 2015.

Wilson K, Dutcher S, Bayly P. Dynein Arm Mutations Modify the Effects of Increased Viscous Forces on the Flagellar Waveform. Poster presentation, BMES 2014 Annual Meeting, San Antonio, TX, October 22-25, 2014.

Bayly PV and **Wilson KS**. Equations of Inter-doublet Separation during Flagella Motion Explain Propagation of Dynein Activity. Platform presentation, BMES 2014 Annual Meeting, San Antonio, TX, October 22-25, 2014.

Wilson K, Dutcher S, Bayly P. Effect of viscosity on flagellar waveform: experiment and theory. Selected for PhD Student Paper Competition (36/700 submissions selected), World Congress of Biomechanics (WCB) 2014, Boston, MA July 6-11, 2014.

Wilson K, Dutcher S, Bayly P. Beat Frequency is Reduced but Waveform Shape is Conserved in *Chlamydomonas* Flagella at High Viscosity. Poster presentation, Biophysical Society Annual Meeting 2014, San Francisco, CA February 15-21, 2014.

Wilson K, Bayly P, Okamoto R, Dutcher S, Ferkol T. Mechanical Characterization of Biological Motors: Cilia and Flagella. Invited oral presentation, Imaging Sciences Pathway Retreat, June 28, 2013.

Gonzalez O, **Wilson K**, Bayly P, Okamoto, R. Particle Image Velocimetry of Cilia Movement. Poster presentation, Imaging Sciences Pathway Retreat, June 28, 2013.

Wilson K, Bayly P, Okamoto R, Dutcher S, Ferkol T. Mechanical Characterization of Biological Motors: Cilia and Flagella. WUSTL Graduate Research Symposium, February 16th, 2013. Awarded 2nd place, Engineering.

Wilson KS, Bayly PV, Okamoto RJ, Dutcher SK, Ferkol TW. Characterizing a Human PCD-Related Mutation by Kinematic Analysis of Chlamydomonas Swimming. BMES 2012 Annual Meeting, Atlanta, Georgia, October 24-27, 2012.

Xu G, **Wilson KS**, Okamoto RJ, Shao JY, Dutcher SK, Bayly PV. Flexural Rigidity and Shear Stiffness of Flagella. Proceedings of the 56th Meeting of the Biophysical Society. San Diego, California, February 25-29, 2012.

Xu G, **Wilson KS**, Okamoto RJ, Shao JY, Dutcher SK, Bayly PV. The Apparent Flexural Rigidity of the Flagellar Axoneme Depends on Resistance to Inter-Doublet Sliding. Proceedings of the ASME 2012 Summer Bioengineering Conference (SBC2012), Fajardo, Puerto Rico, June 20-23, 2012.

Okamoto, R. J., Clayton, E. H., **Wilson, K. S.**, Bayly, P. V. Validation of Magnetic Resonance Elastography by Dynamic Shear Testing in the Shear Wave Regime. Proceedings of the ASME 2010 Summer Bioengineering Conference (SBC2010), Naples, Florida, June 16-19, 2010.

Clayton, E. H., Okamoto, R. J., **Wilson, K. S.**, Namani, R., Bayly, P. V. Comparison of Dynamic Mechanical Testing and MR Elastography of Biomaterials. SEM Annual Conference and Exposition on Experimental and Applied Mechanics, Indianapolis, Indiana, June 7-10, 2010.